Development of Comprehensive Experimental, Analytical and, Numerical Methods for Predicting Rubber Friction and Wear under Thermomechanical Conditions

By

Mehran Shams Kondori

Dissertation submitted to the faculty of the Virginia Polytechnic Institute and State University in partial fulfillment of requirements for the degree of

Doctor of Philosophy

In

Engineering Mechanics

Saied Taherii, Chair

Corina Sandu

Reza Mirzaeifer

Shima Shahab

Omuar Barry

August 27, 2021 Blacksburg, VA

Keywords: Wear, Friction, Tire, Numerical model

Copyright © 2021 Mehran Shams Kondori

Development of Comprehensive Experimental, Analytical and, Numerical Methods for Predicting Rubber Friction and Wear under Thermomechanical Conditions

By

Mehran Shams Kondori

ABSTRACT

Viscoelastic materials have been used widely in different applications, such as constructing tires, artificial joints, shoe heels, and soles. A study on the different characteristics of viscoelastic materials has always been a matter of interest in order to improve their properties for various applications.

In the automotive industry, rubber, as a viscoelastic material, has been used in several subsystems, such as vehicle interior, suspension, steering joints, and tires. The tire and terrain's contact characteristics are among the essential factors for assessing the performance of the tire and the vehicle in general. Friction and tread wear are two of these contact characteristics. Considering the tire's functionality, for most applications, it is desired to have higher friction to have better traction and a lower wear rate to minimize the material loss of the tread.

The friction coefficient and the rubber's wear rate depend on various parameters such as rubber material properties, terrain characteristics, temperature (tread and the environment), and the load. To obtain the wear rate and friction of a viscoelastic material, three approaches have been used for this study: Experimental, Analytical, and Numerical. The results obtained using these approaches have been compared and validated.

Several test setups have been designed and implemented to study the wear and friction of the rubber experimentally. Also, a new linear friction tester has been designed and manufactured by the author to achieve this project's objectives. The new test setup has several advantages over existing test setups in this field, such as covering a higher range of velocities while maintaining high precision. The designed Linear Friction tester and the modified dynamic friction tester at the CenTiRe laboratory at Virginia Tech were used to measure the rubber's friction and wear for different testing conditions such as different normal loads,

different velocities, and various surfaces such asphalt and sandpaper. The data collected by the experiment will later be used for the validation of the developed models.

In order to obtain the wear rate of the rubber using the analytical approach, the real contact area and friction of the rubber were calculated using Persson's model. The simulation has created the surface to obtain the friction coefficient and the real contact area. After obtaining the friction coefficient and the real contact area, the rubber's wear rate was calculated using a novel approach by combining the Persson Powdery Rubber Wear model with the Crack Propagation model. The results from the improved model compare well with the results from the original model.

For the last step of this project, a Finite Element approach was used for modeling a tread block and round rubber sample. A new semi-empirical model for wear was developed by improving the Archard wear model. The novel approach was implemented to Abaqus by using the Umeshmotion subroutine and adaptive mesh motion (ALE) and subroutine UFric and UFric_Coef in two categories: The Node base method and the Ribbon base method. For finite element modeling, the visco-hyper elastic material model has been used to define the rubber's material properties.

Development of Comprehensive Experimental, Analytical and, Numerical Methods for Predicting Rubber Friction and Wear under Thermomechanical Conditions

By

Mehran Shams Kondori

GENERAL AUDIENCE ABSTRACT

Viscoelastic materials have been used widely in different applications, such as constructing tires, artificial joints, shoe heels, and soles. Therefore, studying the different characteristics of viscoelastic materials has always been a matter of interest in improving their properties for various applications.

In the automotive industry, rubber, as a viscoelastic material, has been used in several subsystems, such as vehicle interior, suspension, steering joints, and tires. The tire and terrain's contact characteristics are among the essential factors for assessing the performance of the tire and the vehicle in general. Friction and tread wear are two of these contact characteristics. Considering the tire's functionality, for most applications, it is desired to have higher friction to have better traction and a lower wear rate to minimize the material loss of the tread.

This study used different approaches such as experimental, analytical, and numerical methods to predict the friction and wear of the rubber sample in contact with different surfaces. For the experimental parts, the author designed and manufactured a linear friction test setup. For the numerical parts, a new semi-empirical model was created to predict rubber samples' wear accurately.

Dedication

This dissertation is dedicated to my love, Hoda, and my dearests, my parents, Fakhrodin and Sodabeh.

Acknowledgments

I would like to sincerely thank my advisor, Prof. Saied Taheri, for his help and support via technical advice and direction, as well as his personal support. Furthermore, I am deeply grateful for his trust in me by giving me the opportunity of joining his group to start the new chapter of my life and follow my dream.

I would also like to thank my committee members for their help and support. Also, I would like to thank my colleagues, thank you for your help and for creating this fantastic team. I have been fortunate to work with you over these years. The work presented here would not have been possible without your contributions

Finally, I would like to thank my wife, Hoda; I am truly grateful for your love and support. Without you, I would not have been able to thrive in my doctoral program or balance my research with everything else. Thanks for joining me in this scholarly adventure – I could not accomplish this feat without you by my side.

Table of Contents

List of Figures

List of Tables

List of Abbreviations

Abbreviation	Description
ALE	Adaptive mesh motion
WLF	William_Landel_Ferry
DFT	Dynamic Friction Tester
LFT	Linear Friction Tester
COF	Coefficient of friction

Chapter 1

Introduction

1.1 Background and Motivation

As a viscoelastic material, rubber has been used in different applications and industries, such as the tire industry. The friction and wear rate of the rubber are two essential parameters in studying contact mechanics. The friction and wear rate of the tires tread section has always been a research topic of interest. However, in the existing literature, most of the friction and abrasion prediction methods are based on experimental results under a few specific conditions, and a comprehensive model between different abrasive conditions and abrasion mechanisms is missing. Although there are several numerical and analytical models to predict the friction coefficient and the wear rate of the rubber [1], [2], none of them can present a model that acceptable results. Among the existing models, the Persson model shows more acceptable results in comparison with other models suggested. However, if one compares the Person's model's results with the experimental results, a considerable amount of error can still be found. Some studies tried to improve the original Persson model in different ways [3].

In this study, three approaches have been considered to achieve the project's main objectives: Analytical approach, numerical method, and experimental method.

Besides, even though all three existing approaches have been used in different studies separately, based on the literature search, no unique study covers all three approaches together to present a comprehensive model.

1.2 Research Objectives

To achieve a comprehensive understanding of the rubber's wear and friction mechanism, the following objectives were defined for this project:

- Conducting a comprehensive literature review on the existing studies on the wear rate and friction
- Design and manufacture of a linear sliding friction tester
- Comparing the results obtained by the linear sliding friction tester and the Dynamic friction tester
- Obtain the effect of different operating conditions such as normal load, velocity, rubber compound material, surface type, surface characteristics, and temperature on wear mechanism using the Linear friction tester and the Dynamic friction tester
- Understanding the effects of temperature on the wear rate by modifying and using the test setups
- Estimation of friction coefficient of the tread and tire durability by developing a comprehensive wear model
- Develop a numerical model to estimate the friction and abrasion properties of the tread compound on a rough surface
- Comparing the results obtained by three approaches (experimental method, analytical model, and numerical method)
- Sensitivity analysis of rubber friction and wear rate with respect to different parameters.

1.3 Research outlines

As shown in Figure 1-1, three approaches have been considered to achieve this project's objectives: Analytical, numerical, and experimental.

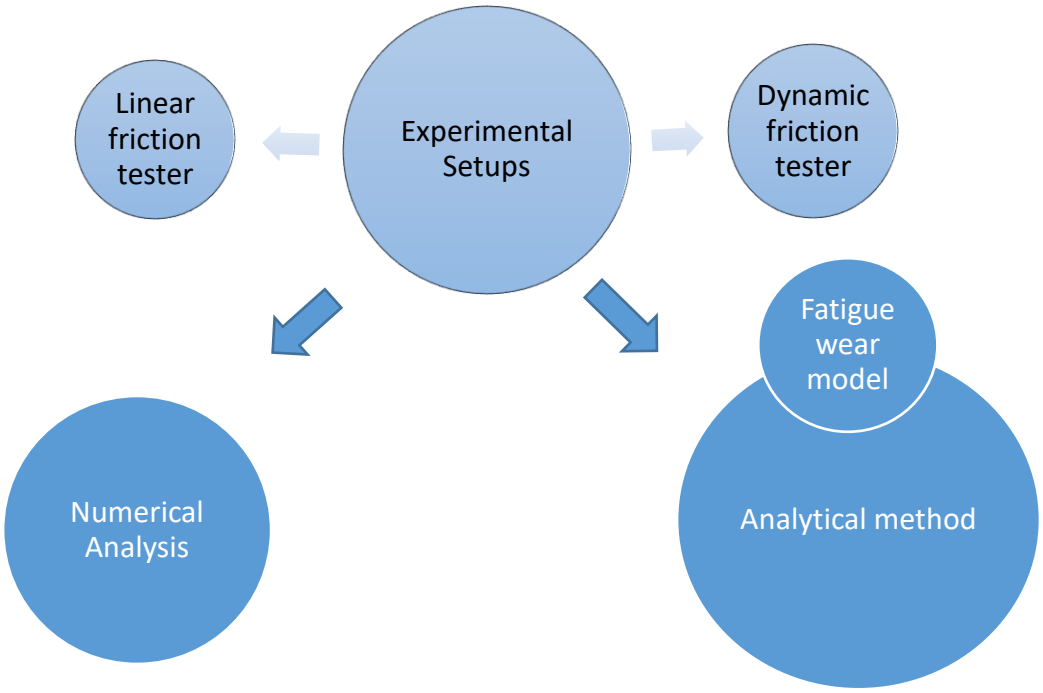

Figure 1-1: Various methods used in this study

This document includes seven sections. In Section 1, an introduction to the motivations and objectives of this project has been presented. Section 2 covers a comprehensive literature review of different approaches, including analytical, numerical, and experimental methods.

In Section 3, the experimental part of this study has been explained. A linear friction tester has been designed and manufactured to study the rubber sample's wear and friction experimentally. The new linear friction tester and the dynamic friction tester can measure the rubber's friction and wear for different testing conditions; such as various temperatures of the rubber and environment, different normal loads, different velocities, and various surfaces

such as icy surface, asphalt, and sandpaper.

Section four covers developing the analytical approach to predict the wear rate and friction for material in contact with a rough surface.

In Section 5, the numerical method used in this study is presented. The finite Element Method has been used to obtain the material's wear rate and friction under different conditions. Finite Element modeling can be used for modeling a tread block sample or a tire. One of the first steps to simulate the rubber's wear rate and friction using finite element analysis is defining the rubber's material properties. Based on the model's application and precision, rubber can be modeled as elastic, viscoelastic, hyperelastic, or a combination of these categories. Then, the new semi-empirical model for predicting the wear rate was developed and implemented in Abaqus. Finally, sections 6 and 7 presents the conclusion and possible future work.

Chapter 2

Literature Review

A study on the contact mechanics between two surfaces has always been a matter of interest to the research community [2], [4]–[10]. Several approaches have been used to investigate the contact characteristics of different materials. These approaches can be divided into several categories: the experimental method, analytical method, numerical, and semi-analytical.

Due to the complexity of friction and wear mechanisms, the experimental method is one of the best solutions. Thus, most studies on friction and wear mechanisms have focused on contact mechanics using the empirical approach. In order to conduct the required tests for these studies, several test setups have been designed by various researchers worldwide. Some of the existing studies on friction and wear at the two solids' contact areas using an experimental approach are presented in the next section.

2.1 Experimental approach

A summary of the studies conducted on the wear and friction mechanism using an experimental approach has been presented in this section.

Schallamach [11] conducted several tests using rubber samples and a needle to study different rubber compounds' wear rates. He scratched a needle on the surfaces of the rubber samples in a controlled condition. Figure 2-1 from his study shows the rubber surface deformation's abrasion pattern due to the needle sliding on the rubber, called the stick-slip mechanism. The author compared the needle and rubber's contact mechanism for soft and stiff rubbers and different normal loads in this study. He showed that the groove's depth

created on the rubber surface depends on applying the normal load and rubber's hardness. In another study by him [12], [13], the pattern of rubber abrasion for different rubber compounds has been studied.

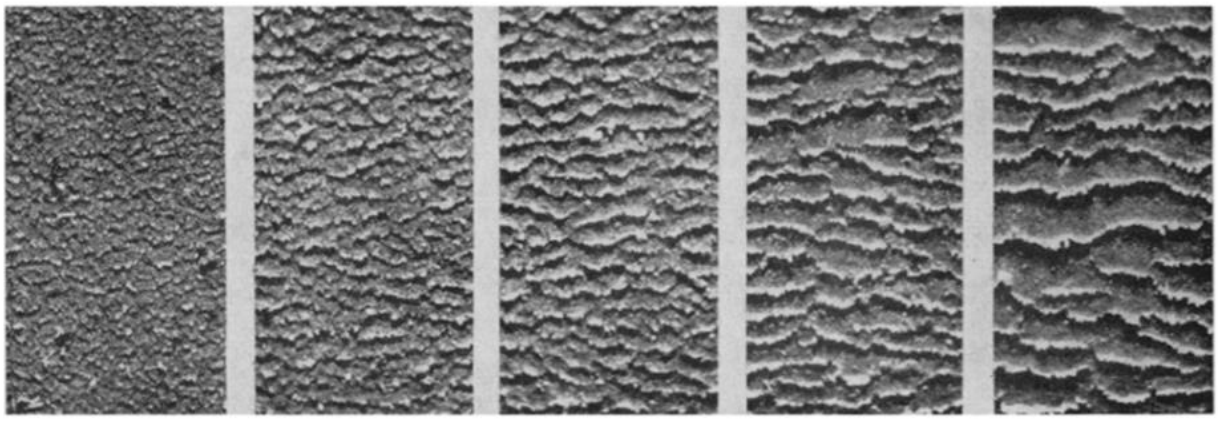

Figure 2-1: Abrasion pattern for the rubber for different distances of travel

The dependency of the friction coefficient and wear rate of epoxy-rubber composites to speed, load, and time has been investigated in various studies [14], [15]. These studies show the low wear rate and friction coefficient values for the sliding rubber in dry conditions.

In a study by Sivaraos et al. [16], several tests were conducted to obtain the friction coefficient and tire rubber wear rate. A pin-on-disc tribometer (CM-9109), shown in Figure 2-2, was used in this study. The tests were conducted for a dry flat surface. Figure 2-3 shows a part of the results obtained by this study. This figure shows that for rubber samples with different filler percentages, the rubber with the highest percentage of filler has the highest friction coefficient among all the samples. In addition, it has been shown that the friction coefficient has an increasing trend at the beginning of the test until it reaches an almost constant value.

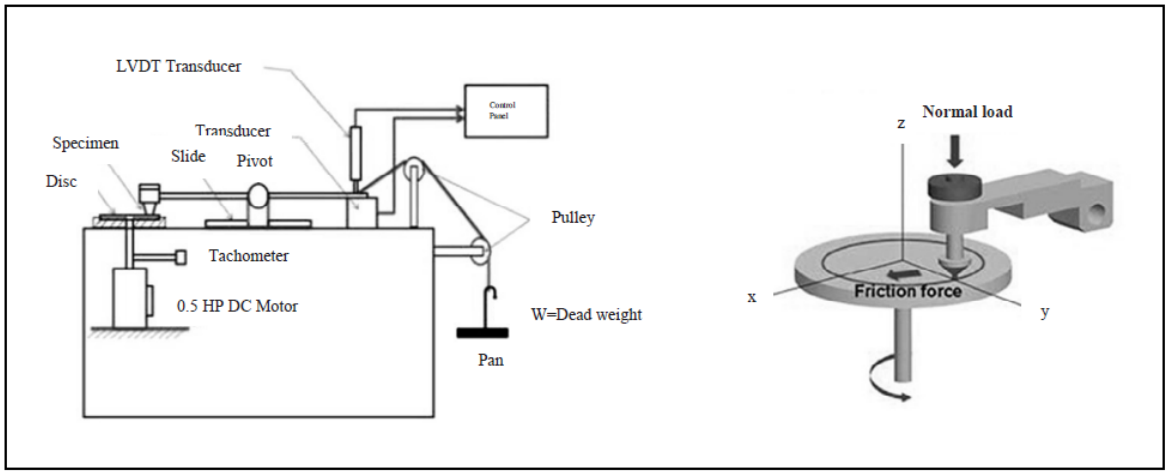

Figure 2-2: pin-on-disc tribometer [16]

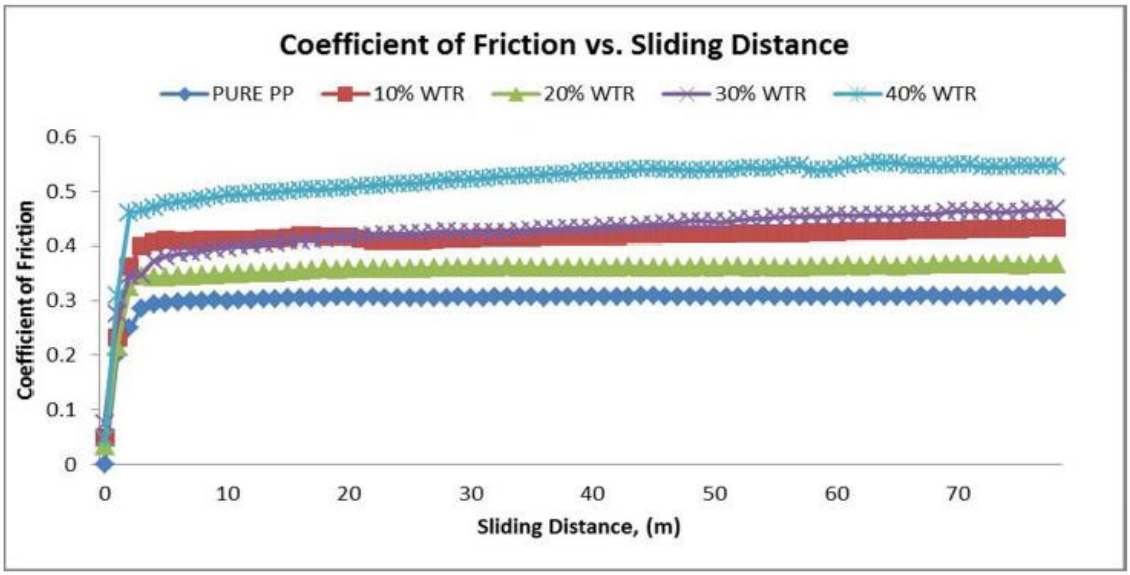

Figure 2-3: Friction test results [16]

A friction setup has also been used in a study by Hemette et al.[17]. This test setup can capture the real-time ice-rubber contact area and measure the contact patch forces in a temperature-controlled environment. The effect of different parameters on tire-ice contact characteristics such as ice surface melting, viscoelastic deformation, ice creep, and adhesion was investigated in this study. The test setup was designed at Ecole centrale de Lyon and can control velocity and temperature during the test. Figure 2-4 shows the schematic of the test

fixture.

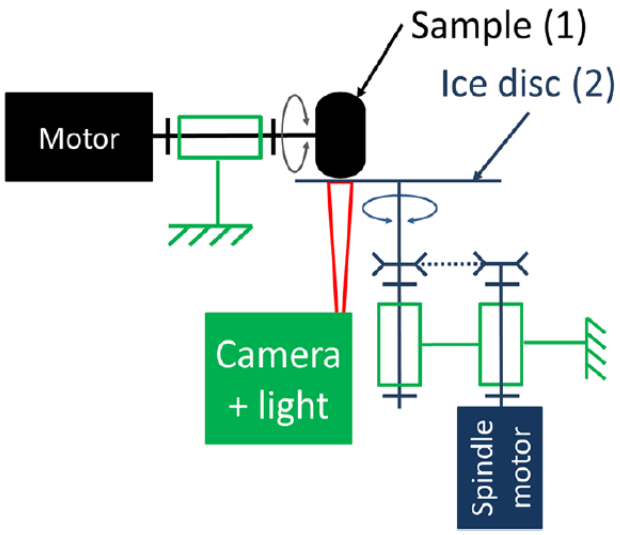

Figure 2-4: Schematic of the design used in [17]

Figure 2-5 shows the trends obtained for the friction coefficient and real contact area vs. velocity. As shown in this figure, there is a peak value for the friction coefficient around 0.1 m/s.

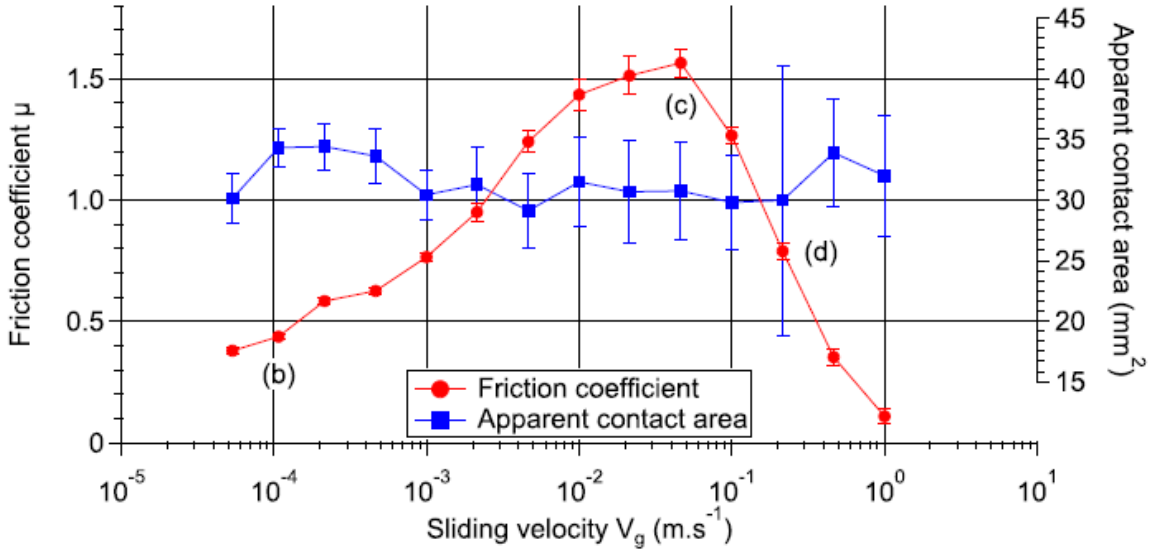

Figure 2-5: Friction coefficient and real contact area vs. velocity [17]

In another study by Lahayne et al. [18], a linear friction tester was introduced and used to conduct several tests to obtain the friction coefficient. Figure 2-6 shows the test setup. The test setup has been designed to obtain the sliding friction of the rubber on different surfaces. The design's significant advantages are its capability to control the temperature *(* -30 °C < *T* < +40 °C) and humidity. Here are some other characteristics of the linear friction tester in this study: It can cover about 300 mm sliding distance, the range of the sliding velocity *is* 0.01 mm/s < *v* < 1100 mm/s, and the nominal contact pressure range is 1 bar < *p* < 30 bar. Figure 2-7 shows a part of the results obtained by this study. As shown, the friction coefficient on asphalt increased by raising the temperature, while a decreasing trend can be observed for concrete.

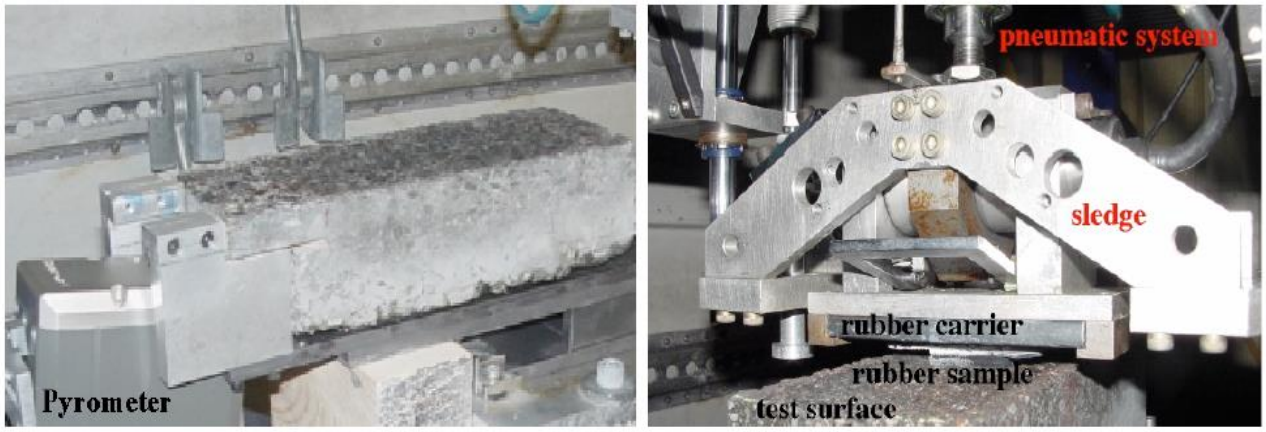

Figure 2-6: Sledge device (right), pyrometer (left) [18]

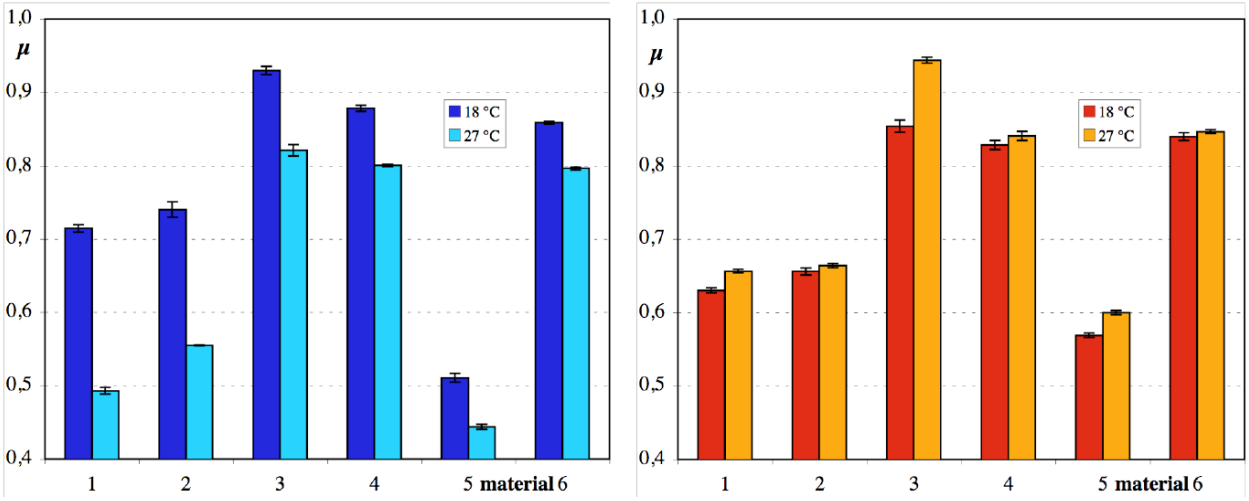

Figure 2-7: Test results for concrete (left) and asphalt (right) [18]

2.2 Theoretical approach

The study on contact mechanics, which means focusing on the deformation of two solids' surfaces in contact with each other, is an essential topic in mechanical engineering and has always been a matter of interest. Although numerous research has been conducted in this area, a limited number of them focused on the contact characteristics of two solids with randomly rough surfaces. It is not easy for the solids with randomly rough surfaces to define the contact area due to the complication of defining the contact points for two surfaces with roughness. Considering the distribution of the asperities on the surfaces, it is incorrect to say that two surfaces of the elastic solids with randomly rough surfaces have a contact at every point within the contact area. The real contact area is dependent on the scale of the study and the distribution of the asperities.

Practically, for different length scales, all macroscopic bodies have surfaces with roughness in nature. By increasing the magnification, small-scale surface roughness can be observed for even a highly smooth surface. Considering the magnification's effect on the roughness's existence, it is essential to consider all length scales for a comprehensive study on the contact mechanics. Three contact characteristics should be considered: the contact

regions stress distribution, the real contact area, and the non-contact regions due to the interfacial separation of the particles.

When two solids are in contact with each other, only a small fraction of the contact area is really in contact. This small fraction of the nominal contact area is called the real contact area and depends on the contact points' distribution. The contact points are highly dependent on the surface roughness. Thus, to consider all the surface characteristics to obtain the real contact area, it is crucial to investigate the effect of roughness for different length scales. This scale varies depending on the problem. For example, these scales may vary from minimal size (atomic resolution) to centimeter range for the tire-terrain study, which is the range of the roughness on the terrain and tread of the tire. A study on this phenomenon using a numerical approach is not possible due to computer resources limitations. Considering the number of particles involved in this problem, too many degrees of freedom will increase the computational cost. Thus, using an analytical approach will be required to understand the contact mechanics characteristics.

This section presents a summary of the research conducted on contact mechanics using the analytical approach. One of the first analytical models was developed and presented by Hertz [1]. In this study, he investigated the contact characteristics between two elastic solids with smooth surface profiles. Hertz assumed no friction within the contact and parabolic shape for the surface's deformation close to the contact area. This study obtained the relationship between the real contact area A and the squeezing force Fn (normal load).

For modeling rough surfaces, several approaches have been presented in the past. Figure 2-8 shows the idea behind three of these approaches. Figure 2-8 (a) illustrates the simplest model for modeling a rough surface presented by Hertz. The surface's roughness has been shown using an array of equal spherical bumps with equal height ‘h’ and equal radius ‘R’. Hertz's theory can be approximately applied to all of the asperities when a surface is in contact with the elastic flat surface. That means we have an increase in the real contact area by increasing the normal load. These results do not coincide with the results from an experiment that shows when we have a small contact area A; the real contact area is proportional to the normal load.

In another study, a more realistic hierarchical model was developed by Archard. In this study, the surface roughness has been described with different spherical bumps on top of each other. The results from this theory show that the real contact area is proportional to the normal load. Another model that delivers more precise and useful results is Greenwood and Williamson (GW). Figure 2-8 (b) shows that this model used an ensemble of identical spherical asperities with randomly distributed heights but equal radius R to model the surface's roughness.

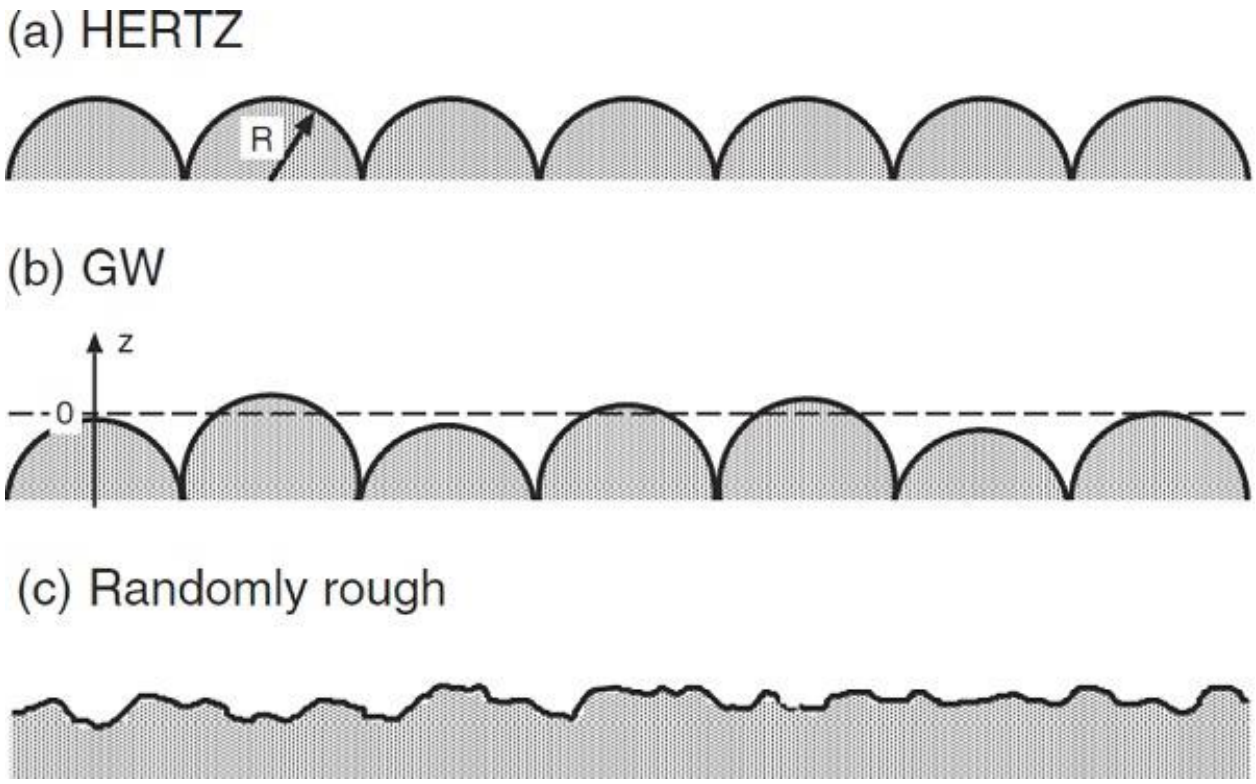

Figure 2-8: Modeling a rough surface with a different approach [19]

Bush, Gibson, and Thomas (BGT) presented one of the best multi-asperity contact theories. In their method, the asperities were modeled as paraboloids with different radius of curvature. In this theory, the surface roughness for different length scales was taken into account. In contrast, other theories such as the GW theory, a single length scale for the roughness, have been assumed, resulting in a slightly non-linear dependency of the real contact area on the applied load.

The BGT theory showed a relationship between the load and real contact area. These

results coincide with the experimental results that show that when we have roughness with different length scales, the real contact area is proportional to the applied load. However, this theory only works for shallow squeezing pressure. In general, multi-asperity theories will present the correct results only when the applied loads and contact areas are small. The main reasons for these results are two assumptions considered for these theories. The first and most important one is neglecting the long-range elastic deformation caused by changes in the contact between other asperities that happens when pushing downward on an asperity. The second problem is caused by modeling the asperities using bumps with an equal radius of curvatures [1], [20], [21],[2].

2.3 Friction

The resistance of the surfaces to the relative motion for two objects in contact with each other is called friction. Obtaining the frictional forces within the rubber materials' contact area in contact with different surfaces was studied extensively. Investigating the effect of different parameters on rubber friction was started in the early 1940s. The classic laws of friction were suggested by Leonardo da Vinci [22], who is known as a pioneer in tribology. Amontons [23] and Coulomb later rediscovered the primary laws of friction called Amontons-Coulomb Friction Laws. Several empirical and semi-empirical models to define the friction for different operational conditions were developed later.

The strong dependency of the rubber friction on the sliding velocity was shown by Grosch [13] in 1963 using an experimental approach. He shows that frictional value increases with an increase in the sliding velocity until reaching the maximum value, and then it drops. In addition, he suggested that the effects of the temperature and velocity on friction are similar to their effects on dynamic modulus. Using the results obtained by Grosch's experiments, Schallamach [24] later suggested a theory for dynamic rubber friction.

A semi-empirical model was proposed by Savkoor [25]. This model, which is based on experimental results obtained by Grosch, can be used for creating an isothermal master curve for friction coefficient values, as shown in Equation 2-1:

$$\mu(v) = \mu_s + (\mu_{max} - \mu_s) \exp\left\{-h^2 \log^2\left(\frac{v}{v_{max}}\right)\right\} \quad 2\text{-}1$$

Where v_{max} is the speed, μ_s is the static friction coefficient by which its maximum value is μ_{max}. h is a factor that can be obtained using experimental data. This factor determines the range of velocities. Both v_{max} and μ_{max} are dependent on the rubber compound viscoelastic properties and temperature. The changes in the temperature cause a shift in the friction curve towards higher velocities.

Another curve-fit model was proposed by Nackenhorst [26]. Average contact pressure effect on the friction coefficient was included in this model, as shown in Equation 2-7:

$$\mu(v,p) = c_1\left[\frac{p}{c_2}\right]^{c_3} + c_4 ln\frac{v}{c_5} - c_6 ln\frac{v}{c_7} \quad 2\text{-}2$$

All the parameters in this model needed to be determined using experimental data. In addition, pressure and sliding velocity effects are decoupled in this model.

A quadratic curve-fit equation is used by Dorsch et al. [27] to model the friction coefficient. This model is a function of normal pressure p and velocity $\boldsymbol{v}$ as shown in Equation 2-8:

$$\mu(v,p) = c_1 p + c_2 p^2 + c_3 v + c_4 v^2 + c_5 pv \quad 2\text{-}3$$

Experimental data are required in order to obtain the coefficients of this model.

Huemer et al. [28] proposed an empirical model shown in Equation 2-9 to obtain the friction coefficient between macroscopically smooth surfaces and a rubber:

$$\mu(v,p) = \frac{C_1|p|^{C_2} + C_3}{C_4 + c_5\|\vec{v}\|^{-\frac{1}{C_6}} + c_7\|\vec{v}\|^{-\frac{2}{C_6}}} \quad 2\text{-}4$$

The parameters of this equation needed to be found via the experimental approach. The effect of temperature on the friction coefficient is considered in this model. The WLF method can obtain the friction coefficient for different temperatures by shifting sliding velocity and predicting the equivalent velocity for the desired temperature.

A model for rubber friction was proposed by Rado [29]. The model can predict the friction coefficient for different slip velocity changes during the test. The effect of substrate texture is separated from the rubber material behavior in his model:

$$\mu(v) = \mu_p \; e^{-\left(\frac{\ln\left(\frac{v}{v_p}\right)}{C}\right)^2} \qquad 2\text{-}5$$

Where factor *C* depends on the substrate surface macrotexture, this factor is a function of surface Root Mean Square (RMS). $\boldsymbol{v_p}$ and μ_p are the velocity and maximum values of transient friction coefficient.

The main problem of all these models is that they only can predict the friction coefficient at the contact for a specific condition. Moreover, for most of these models, to obtain the model's parameters, an extensive experimental study is required.

Thus, a comprehensive physics-based model that can describe the effect of different physical parameters on the friction coefficient is an essential tool to design the optimum condition for the rubber's interaction with different surfaces.

2.4 Wear

The rubber's wear rate in contact with different types of surfaces was investigated in different studies.

In a study by Schallamach, a simple theory for predicting the wear rate of the rubber was developed [30]–[32]. According to this theory, the wear rate is dependent on the normal pressure σ_0, r as the curvature radius, A_o as the apparent contact area, and constant G which is the elastic constant. Factor C in Equation 2-6 can be obtained using the empirical method.

$$\frac{\Delta V}{\Delta L} = c\frac{\sigma_0 r}{G}A_o \qquad 2\text{-}6$$

Grosch and Schallamach [32] improved the theory by defining a non-linear relationship between the wear rate and the pressure at the contact area. In Equation 2-7, parameters m and n are for the specific rubber compound and substrate roughness, respectively.

$$\frac{\Delta V}{\Delta L} = m\,\sigma_0^n \qquad n > 1 \tag{2-7}$$

In another study by Gent and Pulford [33] two-scale wear mechanisms were introduced: micro-scale and macro-scale. According to this study, the wear that occurs on the rubber surface is called microscale abrasion, and those that appear on the ridge pattern are called macro-scale abrasion.

In another study by Archad [34], Equation 2-8 was proposed to predict the rubber wear rate.

$$\Delta V = K\frac{F_N \Delta L}{H} \tag{2-8}$$

In this model, the wear rate depends on parameters such as normal load (F_N), sliding distance ΔL, the hardness of the material (H), and wear factor K. Factor K depends on different conditions that the wear occurred. This model is similar to the model introduced by Lewis [35]. However, in Lewis's model, instead of ΔL, the velocity and time duration of sliding were replaced and the effect of the hardness did not appear in the equation directly as shown in equation 2-9

$$\Delta V = K_L F_N v \Delta t \tag{2-9}$$

Modeling the rubber wear rate has been improved gradually by considering more parameters in the governing equation. Ratner et al. [36] and Lancaster [37] introduced Equation 2-10 to model the wear rate:

$$\Delta V = K_r \frac{\mu F_N v}{H \sigma_u e_b} \quad 2\text{-}10$$

According to this equation, the wear rate is dependent on parameters such as friction coefficient, ultimate tensile stress, and elongation at the break.

Several semi-analytical models were introduced for the rubber wear rate using the data collected by conducting the tests using a razor blade. From the studies like [21], a non-linear exponential relationship between the frictional work and the volume loss of the rubber was presented, shown in equation 2-11 and equation 2-12

$$W_f = \mu F_N \Delta L \quad 2\text{-}11$$

$$\Delta V = K_l {W_f}^n \quad 2\text{-}12$$

The values of K_l and n should be defined using an experimental approach. These parameters depend on the testing condition as well as the rubber compound properties. The volume loss ratio of the rubber over frictional work is called abrasion energy.

As shown in Figure 2-9, from the study by Grosch and Schallamach [13], abrasion energy depends on various parameters such as temperature and material properties of the rubber compounds.

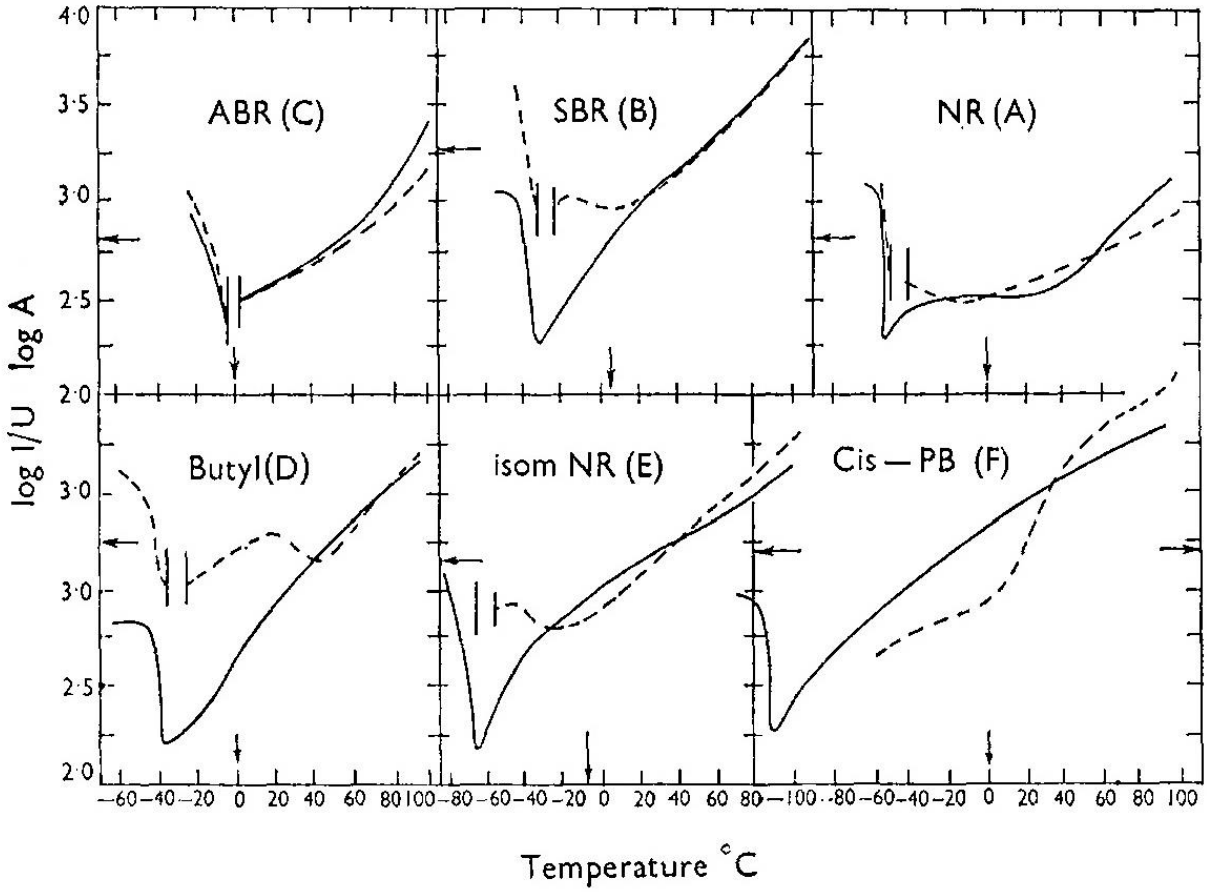

Figure 2-9: Abradability vs. temperature for different rubber compounds [13]

From their study, by decreasing the temperature, the abrasion energy decreases until reaching the minimum value. The solid line in Figure 2-9 shows the reciprocal of the energy density of the break. As can be seen, there is a similarity between the trends of changing the abrasion energy and the energy density concerning temperature.

Among the conducted studies in this field, a limited number focused on both micro-scale and macro-scale rubber wear. Persson [8], [38]–[41] is one of these limited references that developed an analytical model for predicting the wear rate. He proposed an approach to predict the wear rate and called it a Theory of Powdery Wear Model. In Section 2.4.1, more detail on this model is provided.

2.4.1 Persson Model

Persson's contact model [8], [40], [42] is an analytical model for predicting the wear and friction of the rubber. This model is based on multiscale modeling of surface roughness. Power spectrum density is a technique for measuring the roughness of the surface [43][44][45][46]. Using Persson theory, the friction coefficient can be obtained by Equation. 2-13:

$$\mu_H(v) = \frac{1}{2}\int_{q_0}^{q_1} q^3 P(q) C(q) \left\{\int_0^{2\pi} \cos\varphi \, Im\left\{\frac{E(vq\cos\varphi)}{(1-\vartheta^2)\,\sigma_0}\right\} d\varphi\right\} dq \qquad 2\text{-}13$$

Where in the above equation, the power spectrum of the surface roughness can be given by Equation 2-14:

$$C(q) = \left(\frac{1}{2\pi}\right)^2 \int d^2x \langle h(x)h(0)\rangle e^{-iq.x} \qquad 2\text{-}14$$

Moreover, (q) is the area ratio which is a function of different length scales, as shown in Equation 2-15 and Equation 2-16:

$$P(q) \approx \left(1 + [\pi G(q)]^{3/2}\right)^{-1/3} \qquad 2\text{-}15$$

$$G(q) = \frac{1}{8}\int_{q_0}^{q} \left\{q^3 C(q) \left\{\int_0^{2\pi} \left|\frac{E(vq\cos\varphi)}{(1-\vartheta^2)\sigma_0}\right|^2 d\,\varphi\right\}\right\} dq \qquad 2\text{-}16$$

Using this theory, a linear relationship between applying normal force and the value of the real contact area can be found. In this theory, the real contact area is equal to the nominal contact area when the normal pressure is significant. However, as shown in [40], the results

obtained by using the original theory are also acceptable for intermediate values of normal forces. The other existing contact theories are only valid when the nominal contact area is much larger than the real contact area.

The Persson theory was later modified by adding a correction factor to this model. The results from the new model show a better correlation with the numerical results [47]. An essential advantage of this theory is that it can be used for different materials and also operational conditions [8], [47], [48].

In a study by A.Emami [9], Persson's contact theory was improved by developing a new method to calculate the real contact area. The friction and wear were obtained, and the results from the new model improvement were presented in her thesis.

2.5 Numerical method

A numerical method is one of the approaches that can be implemented for a study on contact mechanics. In this section, a summary of the numerical models developed in different studies is presented.

Madge [49] developed a finite element model using ABAQUS commercial software. He used the developed model to predict fretting fatigue life, which included material removal from fretting wear. Two methods were implemented in this study. The first one was based on the Smith-Watson-Topper (SWT) parameter and the Archard wear equation for determining the total life. The second method was used for modeling the crack nucleation with a separate FE routine to evaluate crack propagation using fracture mechanics.

FE models were created for 'cylinder on flat' and 'rounded edge punch on flat' geometries, as shown in Figure 2-10. First, in ABAQUS, one fretting test cycle (Jin & Mall, 2004) was simulated, and the results at each time step were used to calculate the wear depth at each node using the Archard equation. In ABAQUS, the geometry was updated with the UMESHMOTION command to move affected nodes. Because wear changes the specimens' geometry, and thus the mesh, a 'material point mesh' was used for damage accumulation; the

material points accumulate damage interpolated from the FE nodes but do not move as the specimen wears. When material point represents worn away, that point no longer accumulates damage.

For the next step, each element's damage was calculated using the SWT parameter with Palmgren-Miner criteria. In order to reduce computing time, it was also assumed that the wear and damage were constant over a block of N cycles. If the damage of any element exceeded 1, indicating failure, the component was considered failed. If not, another test cycle was simulated to calculate new wear and damage. This procedure will continue until the component failure occurs.

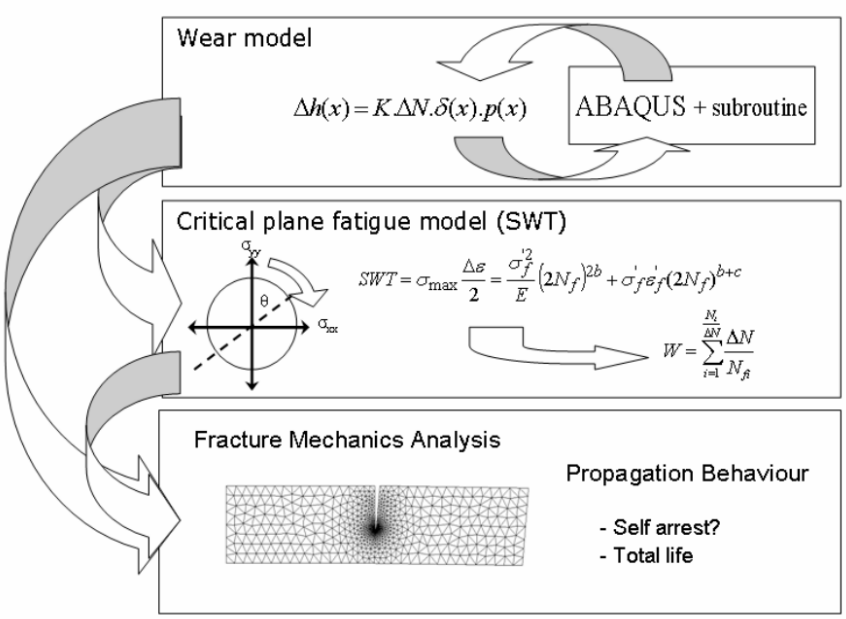

Figure 2-10: wear-nucleation-propagation fretting fatigue methodology [49]

Rosu [50] developed a FE model for the prediction of temperature diffusion in aircraft tires. Both rolling and skidding tires were considered, and a variable coefficient of friction was used to include the effects of temperature and pressure on friction force. The model was validated with both a test rig and temperature measurement of an aircraft tire in use. The test rig model predicted the temperature distribution in the test rig sample reasonably well, except in high wear areas; this suggests that wear must be accounted for in large-scale sliding models. The full tire model disagreed with the tire's initial experimental behavior, but it predicted its final temperature with reasonable accuracy.

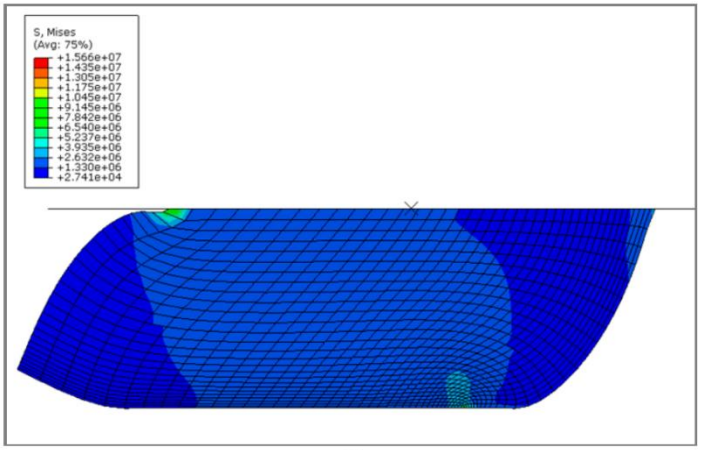

Figure 2-11: specimen shape after sliding, Von Mises's stress distribution. [50]

Yang [51] developed implicit and explicit full-time FE models in order to determine estimation models for tire behavior based on strain gauges. The models were validated with experimental data from a test rig and provided data for reasonable global tire behavior estimates based on strain gauges.

Yang also presented testing procedures for rubber hyperelastic and viscoelastic properties, tire reinforcement properties, and tire profile detection. Because tire characteristics are mostly not available from manufacturers, the relatively simple test presented in [51] could be helpful for modeling tires with unknown properties. ABAQUS was used to convert test data to material properties using Yeoh strain energy for hyperelastic properties and stress relaxation to describe viscoelastic properties. The tire reinforcements were assumed to remain in the linear elastic region. The tire profile was determined using an image captured with an inexpensive digital camera and enhanced in MATLAB.

The FE model was created by first modeling the tire cross-section with 2D axisymmetric elements with embedded rebar elements representing the tire reinforcement. The 2D model was then converted to 3D solid elements around the center axis; the implicit

model, for steady-state rolling analysis, used a variable circumferential mesh size for more refinement at the contact patch, while the explicit model, for transient analysis, used a constant circumferential mesh. The road was modeled as a rigid, flat surface. Four static tests were used to validate the FE model: Deflection due to inflation pressure, vertical stiffness, footprint, and sidewall strain. The model predicted vertical stiffness very well and deflection and footprint reasonably well; The general trends of sidewall strain behavior for circumferential angle were predicted, but the predicted values did not agree exceptionally well. Those results suggest that the model is capable of global tire behavior prediction but not accurate local strain prediction.

In the steady-state rolling analysis, the combined Eulerian-Langrangian method was used where the material rotated, but the mesh did not, allowing for a well-refined mesh at the contact patch with coarse mesh elsewhere for reduced computation time. Estimation models created with data from this FE model provided the right prediction of rolling speed and tire inflation pressure based on strain gauge data. Models of cornering force based on strain gauge data were reasonably close to experimental data but the under-predicted force at high slip angles.

Ultimately, these models did not predict local behavior exceptionally well, which could be due to a lack of detail in modeling materials in the tires and a simple Coulomb friction model in the contact patch. Wear of the tire was also not considered. Global tire behavior, however, was predicted with reasonable accuracy.

Wu et al. [52] developed a numerical model to predict the wear rate in rolling rubber samples using an FE model and experimental results. Savkoor's friction law was used to model dynamic friction, while the Mooney-Rivlin model was used for the rubber. Wu et al. found that generally: the friction coefficient first decreases with increasing velocity, then increases. Increasing velocity increases the wear rate and surface temperature. Wear rates are low at zero slip angle, and wear unevenness increases with increasing slip angle. The surface temperature of the specimen increases up to a certain angle, then decreases. An FE model was validated by comparing the contact patch area with experimental results to determine frictional energy dissipation per revolution. This model shows a perfect correlation with

experiments under 20 km/h but could be improved by including the effects of temperature on friction.

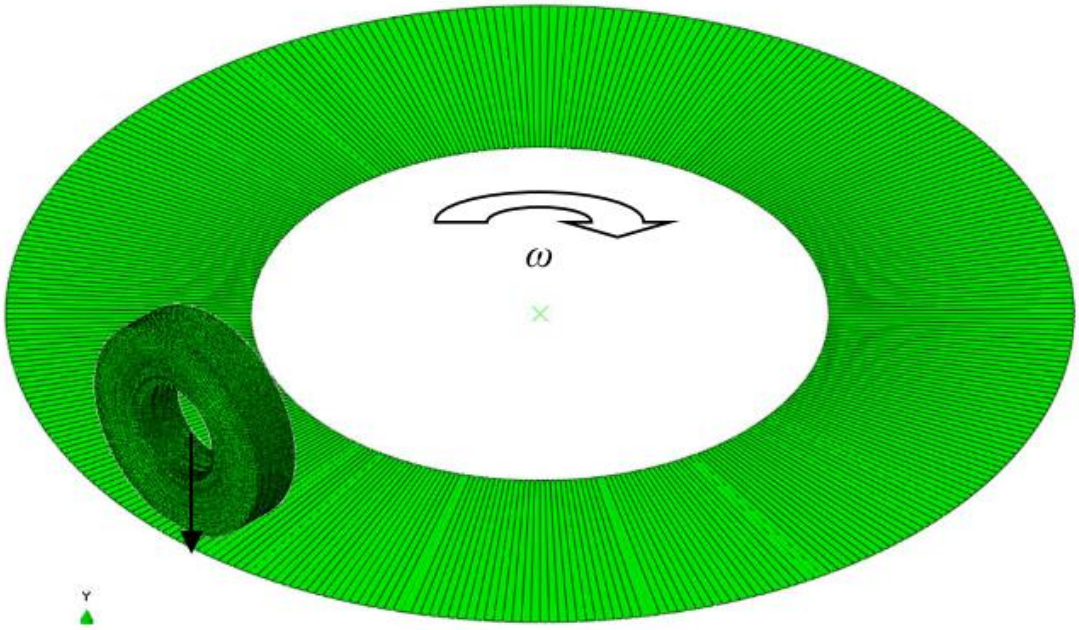

Figure 2-12: a 3D model for a round rubber sample [52]

Vadakkeveetil [53] developed a model to include multiscale surface profile effects, including asperity interaction. The model was meant to determine the friction coefficient and wear properties based on damage mechanics. This setup was modeled with 2D deformable elements in ABAQUS, with penalty contact. The rubber used a Prony series viscoelastic model and Mooney Rivlin hyperelastic model with data from DMA and uniaxial tension tests, respectively. Next, a 2D sliding rubber sample with the normal load was modeled on a rigid plane surface. A friction coefficient of zero and plane strain was assumed. Initially, with sharp corners, the leading edge buckled under the sample; the leading and trailing edges were thus rounded in future models.

A 2D sliding rubber sample was then modeled in contact with a rigid surface with a rough surface profile. This model showed an increase in load corresponded to an increase in

penetration depth, as did a decrease in velocity. Also, this model shows agreement with the previous Kluppel [54], [55] model. However, the models did not quantitatively agree, likely because of the analytical Kluppel model's lack of dynamic and viscous effects and asperity interactions.

A simplified asperity friction model was investigated, which assumed a linear elastic material. This model could find frictional losses across the contact interface. It showed an infinite COF at zero pressure and zero COF for symmetrical contact, agreeing with Persson's previous work [56]–[59]. The effects of fluid on the rough surface were investigated, assuming that fluid fills asperity, reducing their sufficient depth; this should decrease the hysteresis component of friction.

A multiscale model of the rubber sample was then developed. Macroscale was considered profiles with wave vectors between 10^3 and 10^4 and microscale between 10^4 and $10^{4.8}$. These surface profiles were extracted from a measured profile with fourth-order bandpass filters. First, the macro surface profile was imported to ABAQUS as a rigid body, and contact with the rubber sample was considered frictionless. Normal pressure and sliding velocity were applied to the sample, and pressure data was analyzed and sent to a second model. The second model used a small, refined section of the rubber block on a rigid surface with the micro-scale surface profile, again with zero COF. The average pressure distribution from the macro-scale model was applied to the rubber section, and a sliding velocity was applied. The COF of this micro-scale model was then calculated and output into the previous macro model. Finally, the macro model was re-run with the new COF for overall behavior.

The previous model showed decent agreement with analytical models, which assume spherical asperities; however, the FE model did not accurately predict COF values. In addition, the model did not account for adhesion friction components or the flash temperature rise at the sample's leading edge. Finally, wear prediction was added to the model using a continuum damage mechanics approach and compared against Archard's [21] wear law and experimental results. Next, an indenter sliding on rubber was considered, with plane strain, Neo Hookean, Prony series rubber models. This procedure indicated a low wear rate of 0.044 g/s per unit length. An FE model of a sliding rubber sample with the normal load was

developed. Four versions of this model were compared, with varying wear rates per unit length:

1. A plane surface model, with wear based on the Archard wear equation, 0.22 g/s
2. A rough surface model, again with Archard wear, 0.215 g/s
3. A plane surface using a damage mechanics approach; damage occurs if strain energy density reaches a critical value, 0.01059 g/s
4. A rough surface using the same damage mechanics approach, 0.0108 g/s.

The damage mechanics approach predicts wear rates with an order of magnitude difference from experimental results. This difference could be due to the lack of adhesion friction and flash temperature effects. Overall, the models presented by Vadakkeveetil show good agreement with analytical hysteresis friction but not total experimental friction and wear.

Arunachalam and Idapalapati [60] developed an FE model to predict a spinning polishing pad's pressure distribution and wear profile on an aluminum block. The rubber-backed polishing tool was modeled with 3D elements in ABAQUS using the Yeoh model for hyperelastic properties. The tool model was first validated by comparing numerical static pressure distributions to actual pressure distributions obtained with pressure films, which showed good agreement. Next, for the wear model, the wear coefficient for Archard's equation was determined experimentally. An implicit analysis was conducted in ABAQUS for 12.5 revolutions of the tool, and the average contact pressure and sliding distance for each node were calculated. This data was sent to a UMESHMOTION subroutine in ABAQUS General Static, which moved the aluminum nodes based on wear. The new geometry was imported to the implicit dynamic analysis, which was restarted. The use of average contact

pressure values was justified by their small change in between geometry adjustments.

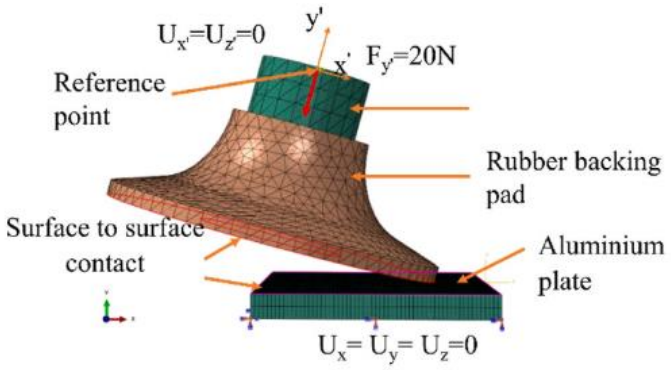

Figure 2-13: 3D model of Rubber pad and aluminum [60]

The previous model showed good agreement with experimental results regarding material removal area and depth, although the distribution of removal depth was different, attributed to the polishing tool's random warping.

Chmiel [61] details two FE methods to predict sliding wear. First, a macro-scale approach based on the Archard wear equation is considered to model a pin-on-disk sliding problem. The thesis describes in detail the ABAQUS procedure used to update the mesh to obtain a wear profile. However, the wear profile appeared wave-like, with excessive wear on specific nodes. It was found that both decreasing the distance increment between each mesh update and averaging pressure across several nodes were needed to reduce this effect. After these corrections, the model showed a respectable average wear height agreement with the Archard wear equation. No experimental validation was performed.

A model based on a damage initiation criterion from Hooputra et al. [62] was then developed for a slipper sliding on a rail. A global model was used for the whole slipper to determine pressure and displacement distributions sent to a microscale sub-model. This sub-model was then simulated to run over an arc asperity, and the damage was calculated to predict wear. However, the wear was not incorporated into the global model, and thus once the sub-model wears, it will not be in contact with the surface. This approach was not validated, and the two approaches were not compared with the same geometry, so accuracy and usefulness are not visible.

Chapter 3

Experimental method

This chapter focuses on experimental design. Experiments with sliding a rubber on different surfaces using two types of test setups, the Dynamic Friction Tester (DFT) and a novel Linear Friction Tester (LFT), are presented separately. The author designed and manufactured the linear friction test rig which was used along with the DFT to conduct several experiments for various rubber samples with different geometries.

The DFT design was improved in this study to enable controlled experiments, i.e., to provide consistency and reliability across experiments and make it possible to control temperature and oxygen levels.

These experimental results were used to investigate the effects of various parameters such as velocity, temperature, and normal load on the wear and friction of different rubber samples. LFT results were validated in comparison with experimental DFT data as well as results from an analytical model developed in this study.

3.1 Dynamic Friction Tester

In order to conduct the test for studying the wear rate and friction of the rubber for tire studies, the Dynamic Friction Tester (DFT) at the CenTiRe laboratory at Virginia Tech was used [63]. The dynamic friction tester is a system to measure the friction/wear for small-

scale studies. This test setup can measure rubber samples' friction and wear with a round shape geometry under different operational parameters, such as normal loads and velocities. The sample's speed and the road surface velocity could be adjusted to obtain the desired sliding velocity. A FUTEK load cell that is connected in the longitudinal direction is measuring the frictional force. Another capability of this test setup is measuring both the dynamic normal load and the temperature at the contact area using non-contact infrared sensors. Figure 3-1 shows the dynamic friction tester.

Figure 3-1: Dynamic friction tester

As part of this project, to improve this test setup's capability and to achieve the goals of this investigation, several modifications were done to this test setup.

3.1.1 Dynamic friction tester modifications

3.1.1.1 Adding Environmental Chamber

In order to investigate the effect of parameters such as the temperature of the environment and level of oxygen, the test setup needed insulation and some other systems for controlling the desired parameters. Thus, the DFT setup is improved by adding a chamber for isolating the testing environment. The chamber is made of Polypropylene with Thermal conductivity of 0.1-0.22 W/(mK). The inside area of the chamber was covered with some isolating plates. A 'T' slot aluminum was mounted on the table to support the chamber. A fan was mounted on the back of the evaporator to provide better convection in the chamber. Besides, a switch box and a gauge were mounted on the chamber for measuring the pressure.

Figure 3-2: Dynamic Friction Tester Modification

3.1.1.2 Adding a chiller/heater system

After insolating the test setup, a chiller/heater system shown in Figure 3-3 was added to

control the chamber's temperature.

Figure 3-3: The chiller/heater system is added to the dynamic friction tester

3.1.1.3 Adding a nitrogen cylinder

To control the level of Oxygen, the percentage of nitrogen inside the chamber was controlled. As shown in Figure 3-2, to change the nitrogen level, a nitrogen cylinder was connected to the chamber. With this modification, the rubber sample's Wear and friction could be measured for different oxygen levels.

3.1.2 Design of experiment

To investigate the effect of parameters such as the temperature of the environment and the level of oxygen, several tests were conducted using the dynamic friction tester for two different rubber samples, A and B. Table 3-1 shows the experiment's design for the test using DFT. As can be seen, the temperature changes from -5˚C to 50˚C and four levels of oxygen have been considered for this study.

Table 3-1: Design of experiment for dynamic friction tester

Dynamic Friction Tester	
Sample type	A, B
Temp [°C]	-5, 0, 10, 25, 35, 50
Level of oxygen	5%, 10%, 15%, 20%
Surface	Sandpaper 120 Grit

3.1.3 Results of DFT

In this section, the data obtained by the tests with DFT that were conducted according to the design of the experiment table (Table 3-1), the wear rate, and friction for two rubber samples are presented. Figure 3-4 shows the sample output for the friction data calculated from DFT with a round sample of diameter 3.11 in and thickness 0.51 in for five different velocities and 0.2 MPa pressure. The friction coefficient was obtained based on the ratio of longitudinal force over the normal load.

Using the modified design, The dynamic friction tester can be capable of testing at different temperatures and different oxygen levels. A set of sample results obtained from the experiment are presented in Figure 3-5 and Figure 3-6. As shown in Figure 3-5: Wear rate of

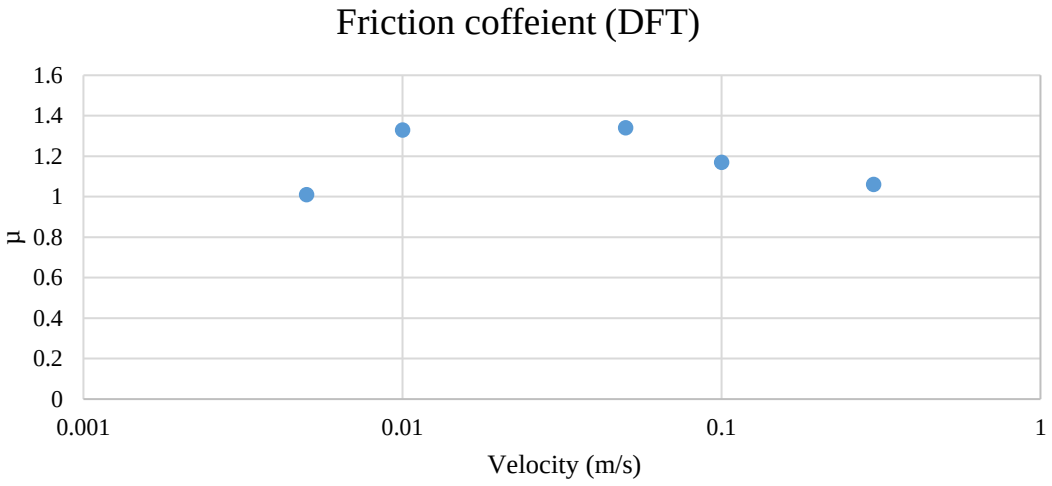

Figure 3-4: Friction coefficient of rubber sample A in different velocity and 0.2 MPa and 25℃ obtained by DFT,

rubber sample B in different velocity in 3 temperature 10℃, 35℃, 50℃, the average wear rate for sample A with 0.2 MPa pressure and different speeds decreases by increasing the temperature. However, the friction coefficient increases by increasing the temperature.

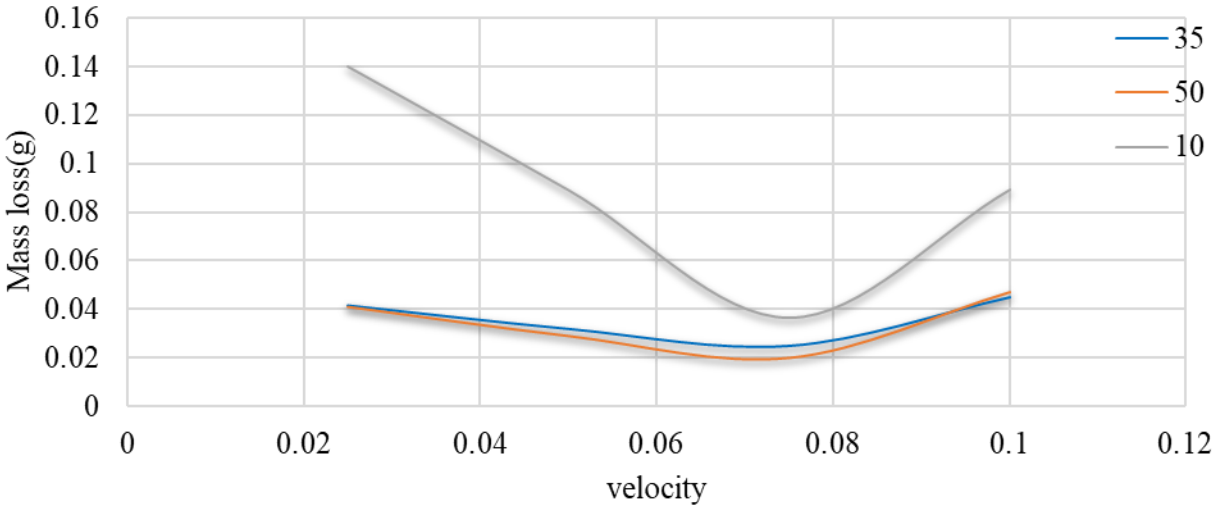

Figure 3-5: Wear rate of rubber sample B in different velocity in 3 temperature 10℃, 35℃, 50℃

Figure 3-6 shows the wear rate for samples A and B in different velocities. As can be seen, the wear rate has an inverse relationship by the temperature and a direct relationship by the velocity.

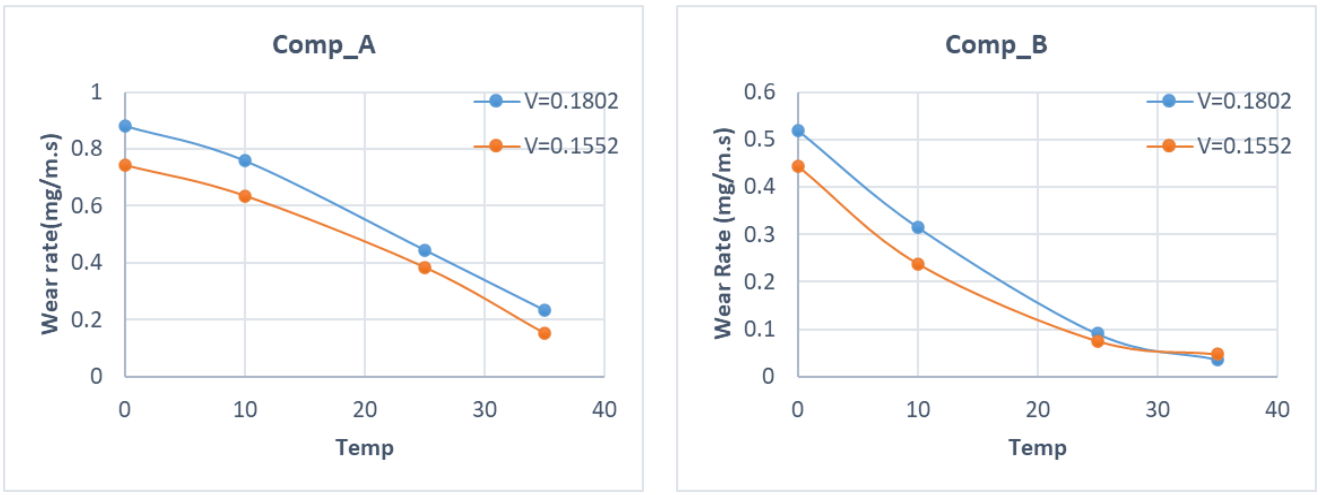

Figure 3-6: Wear rate of rubber samples A, B in different velocities and temperatures

3.2 Linear Friction Tester

3.2.1 Overview

Figure 3-7 shows the test setup designed and manufactured for conducting the tests on the sliding friction of the rubber needed for this study. The linear friction tester (LFT) can slide flat rubber samples approximately two meters across a large flat surface. Two main measurements are possible using this test setup. Measuring the frictional force of rubber samples being pressed onto a surface with various normal loads for different velocities and surface conditions and measuring the rubber sample's wear (or loss of mass) under various conditions. The normal load on the sample is controlled dynamically, and thus the coefficient of friction can easily be calculated from the real-time frictional force. The sample's mass can automatically be measured after each test cycle, which continuously measures the rubber's wear rate. In addition, the contact patch can be captured by a high-resolution camera that can be mounted under the surface of the test setup. The linear friction tester can measure the contact patch's temperature, and for a better understanding of the contact dynamics, the linear friction tester can collect noise data as needed.

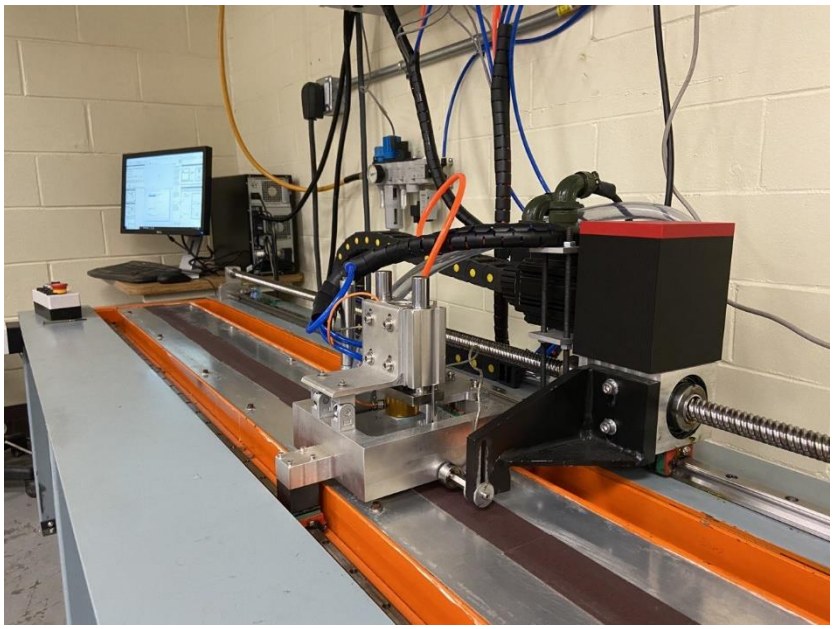

Figure 3-7: Linear friction tester

A similar device to measure the rubber samples' friction and wear rate was developed by other researchers at CenTiRe, as introduced in the literature review section. The new linear friction tester designed for this study has several advantages and improvements compared to the existing test setups. For example, in this design, the normal force changes can be applied dynamically, and the amount of material reduced at each test can be measured automatically. The unique design of the linear friction test setup in this study will allow us to conduct the test at higher speeds and higher precision compared to the existing design in this field. Besides, comparing to the Dynamic friction tester, the Linear friction tester does not apply lateral force to the sample.

3.2.2 Design of the linear friction tester

The part of this study, which is related to the design of the linear friction tester, has three main sections. The first step was designing the mechanical parts of the test setup. After completing the design of all the components using Solid Work software, as shown in Figure 3-8 for a sample part, the parts required for this test setup were manufactured with the Machine shop office's help at Virginia Tech. The rest of the parts required, such as the sensors, were mounted. After completing the test setup assembly, the next step of the design project began, which was working on the power of the system. The second step provided the servo motors required, connecting them to the test setup, and finally assembling the Electrical box. Many parts related to the test setup's power and control, such as DAQ, fuses, solenoid valves, proportional valves, and servo drivers, were included in this box.

The last step was developing the software to control the test setup and programming several codes for performing the analysis required for the linear friction tester to provide the needed data on the friction coefficient and the wear rate. For collecting data and controlling the servo motors, LabVIEW codes were developed and used. For the post-processing of the data, Python software was used.

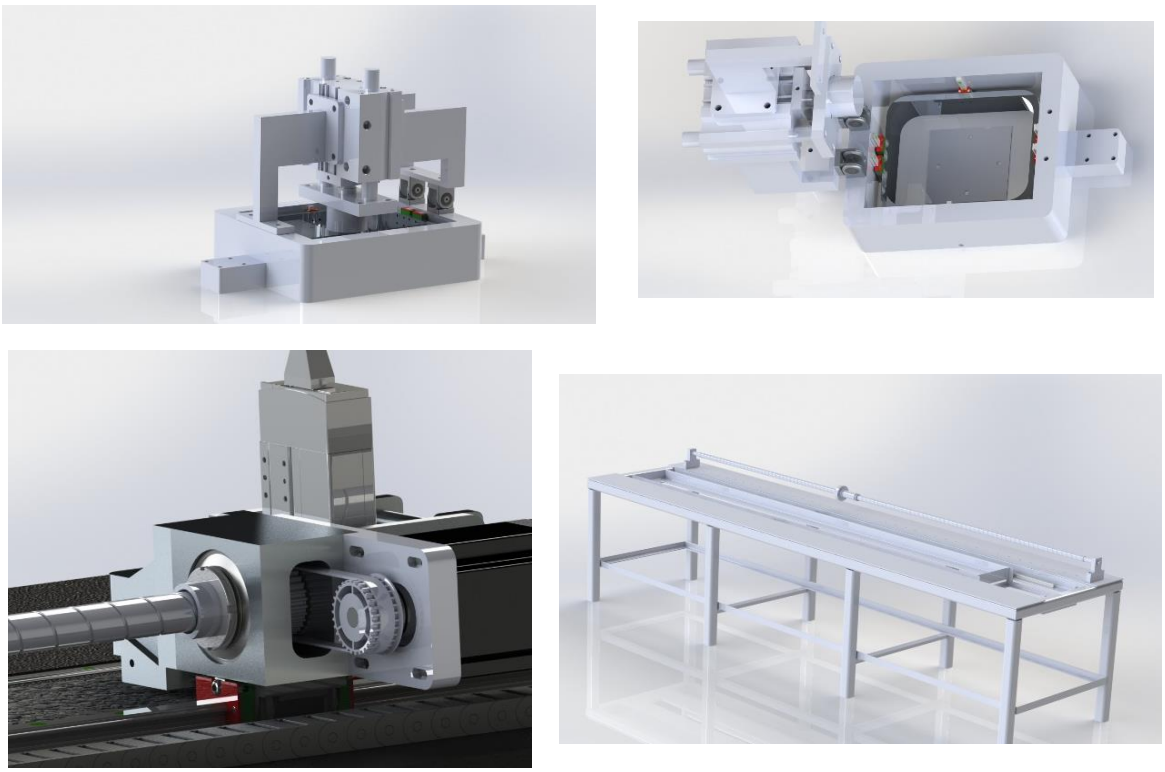

Figure 3-8: Solid work was used to design the components

Table 3-2 shows the linear friction tester characteristics designed for this study.

Table 3-2: Linear friction tester characteristics

Total Length	$2.7\ m$
Sliding Distance	$2\ m$
Velocity Range	$0 - 1.28\ m/s$
Load Range	$0 - 110\ lbs$

The following section will discuss the physical components that make up the LFT, and design justification will be presented.

3.2.3 Components

3.2.3.1 Actuators

The LFT includes four actuating devices: a ball screw and servo motor, which provides linear motion for the sample to be moved down the table; a pneumatic cylinder, which provides the normal load applied to the sample; 10 pneumatic cylinders which lift the sample when no contact between the sample and surface is desired; and one pneumatic cylinder for swiping and cleaning the surface.

3.2.3.2 Ball screw assembly

A ball screw is used to provide the linear motion along the length of the table. The ball screw is a 2600 mm long Stainless-steel screw with a 25 mm lead. The novel approach was used for this test setup to achieve high-speed velocity by decreasing the system's vibration and increasing the system's accuracy. So, rather than being mounted in bearings, the screw is fixed on both ends and pretension. Fixing the screw reduces the vibration in the system dramatically and allows for more precise velocity and normal load control of the sample. The ball nut is rotated with the servo, providing a maximum linear velocity of 3 m/s at maximum motor speed. Figure 3-9 and Figure 3-10 show the trailing side and leading side of the ball screw assembly.

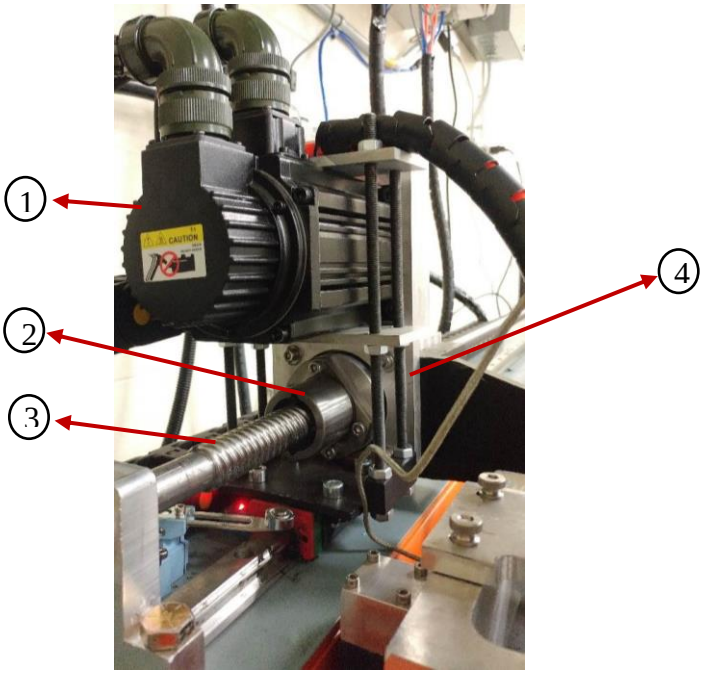

Figure 3-9: Trailing side of the ball screw assembly. 1) The servo motor 2) the ball nut 3) the ball screw 4) the aluminum support plates

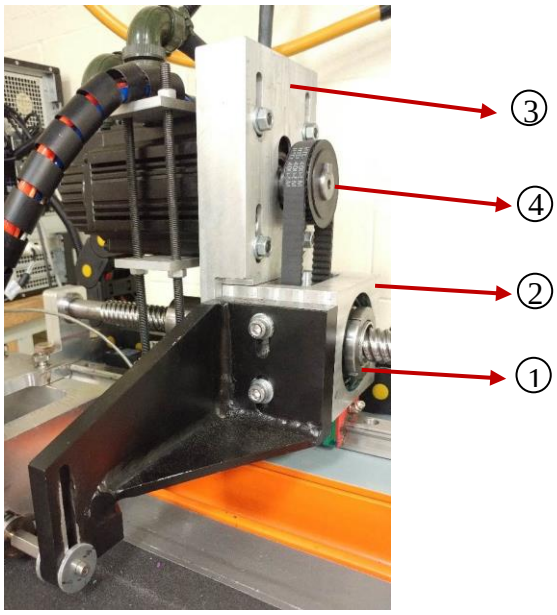

Figure 3-10: Leading side of the ball screw assembly. Piece 1 is the carriage arm; 2 is the bearing house; 3 is the motor fixture; 4 is the primary pulley

3.2.3.3 Servo with driver

A 2kW ECMA-C11020RS Motor drives the ball screw with ASD-A2-2023 servo drive. This servo provides speed accuracy of at least 0.01% and input position resolution of 5000 pulses per revolution. The driver implements closed-loop control using an encoder with a

Figure 3-11: a 2kW ECMA-C11020RS Motor with ASD-A2-2023 servo drive

20-bit resolution. The servo has a maximum speed of 5000 RPM. Figure 3-11 shows the servo motor and drive that is used in this test setup

3.2.3.4 Pulley

The motor is connected to a ball nut with a simple 1:1 belt and pulley system. A 35mm diameter primary pulley is shown in Figure 3-12 is mounted on the keyed motor output shaft, and a 15mm belt connects the pulley to an identical secondary pulley that is slip-fit on the bearing shaft.

Figure 3-12: 36 Tooth HTD5 Pulley (36-5M-15F) (HP36-5M-15F)

3.2.3.5 Bearing shaft

The bearing shaft shown in Figure 3-13a connects the secondary pulley to the ball nut and sits in the bearings in the bearing housing. It is machined from 6061 aluminum and is held in place against the housing with a lock nut. The bearing shaft is hollow because it must fit around the ball screw.

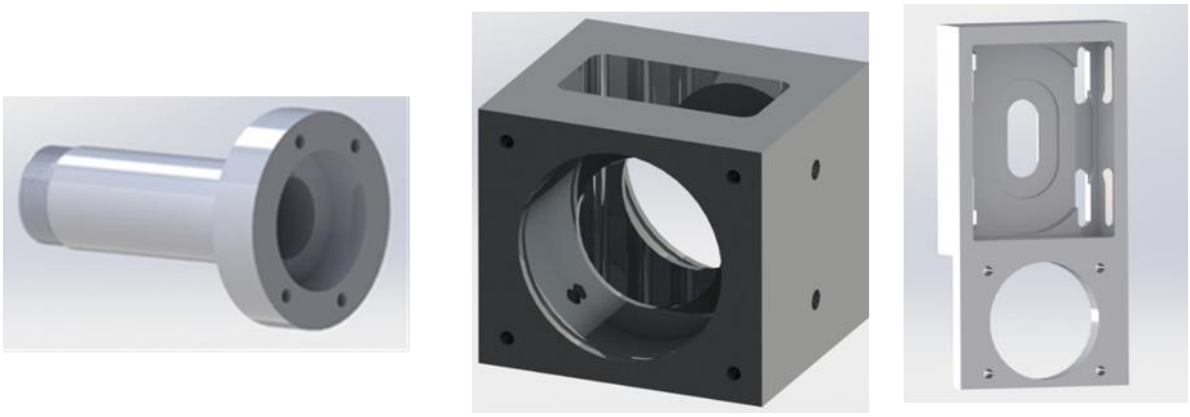

Figure 3-13: a) Bearing shaft b) Bearing house c) the fixture for holding the motor and connecting motor to House bearing

3.2.3.6 Bearing house

The bearing housing connects the motor fixture and carriage arm to the bearing shaft so that they are pulled down the length of the table as the ball nut spins. Two Timken 30207 tapered roller bearings are pressed into the housing, through which the bearing shaft passes. A slot on top of the bearing housing allows the secondary pulley to be installed on the bearing shaft inside the bearing housing and allows the pulley belt clearance. Figure 3-13b illustrates the bearing housing that is designed with Solid Works.

3.2.3.7 Motor fixture

The motor fixture holds the motor above and behind the bearing housing. The fixture shown in Figure 3-13c is a custom 6061 aluminum part bolted onto the leading face of the motor and the trailing face of the bearing housing. Slots are used rather than holes to mount the motor, which allows for easy tensioning of the pulley belt. Extra support was needed to hold up the motor, so aluminum plates were attached to another linear guide underneath the motor and supported with threaded rods and nuts. The plates support the heavy rear part of the motor and reduce stress on the main motor fixture.

3.2.3.8 Carriage arm

An arm is connected to the bearing housing on the inboard side in order to pull the carriage. It is made from welded aluminum plates rather than one machined billet to reduce material cost. A load cell is connected in a vertical slot at the end of the arm, in the middle of the table. The other side of the load cell is threaded into a hole in the carriage, and the slot lets the load cell move freely up and down, allowing the carriage to be raised when no sample contact is desired.

A Futek model load cell is attached between the arm and carriage to sense the rubber sample's frictional force (Figure 3-14). It has a load capacity of 300 N, with a nonlinearity of ± 0.25% of the rated capacity.

Figure 3-14: Futek sensor for measuring the friction force

3.2.3.9 Pneumatic

The pneumatic cylinder for normal force control shown in Figure 3-15a has two 50mm pistons and can deliver forces up to 900N. The air is supplied with a 32 mm sized pneumatic bore.

Figure 3-15: a) The Pneumatic cylinder for applying normal load b) QBX Electro-Pneumatic Pressure Regulator (Proportion-Air proportional valve)

3.2.3.10 Proportional valve

A Proportion-Air proportional valve (Figure 3-15b) controls the]airflow proportional to the supplied voltage. The DAQ provides the voltage input, which sets the pneumatic cylinder's pressure via the PID controller implemented in LabView. A load cell is attached to the end of the pneumatic cylinder to sense the rubber sample's downward force to implement feedback control. It has a load capacity of 500N, with a nonlinearity of ± 0.1% of the rated capacity. A metal plate is attached to the side of the load cell that is not attached to the pneumatic, which presses against the rubber sample.

3.2.3.11 Carriage

The carriage shown in Figure 3-16 is machined from a solid billet of 6061 aluminum. A

threaded hole connects the load cell to the leading face of the carriage. Two 100mm linear guides are attached to the inside of the carriage to allow the sample housing to slide freely in the vertical direction. The guides are necessary to isolate the pneumatic piston from bending loads and associated binding of the cylinder.

3.2.3.12 Fixtures

Fixtures were needed to hold the pneumatic cylinder in place. Fixture 2 is connected with pivoting joints to allow the sample to be removed more easily. Fixture 1 is fixed to two M6 studs in the carriage with knurled thumb bolts that can be easily tightened or removed. (Figure 3-16)

3.2.3.13 Inner fixture

The sample is held in a small aluminum inner fixture that is fixed to the linear guides on the carriage. These linear guides allow the sample to move freely up and down, so the normal force from the pneumatic cylinder and the measurements from the scale represents the actual downward forces on the sample and are not affected by any sort of binding in the system. (Figure 3-16)

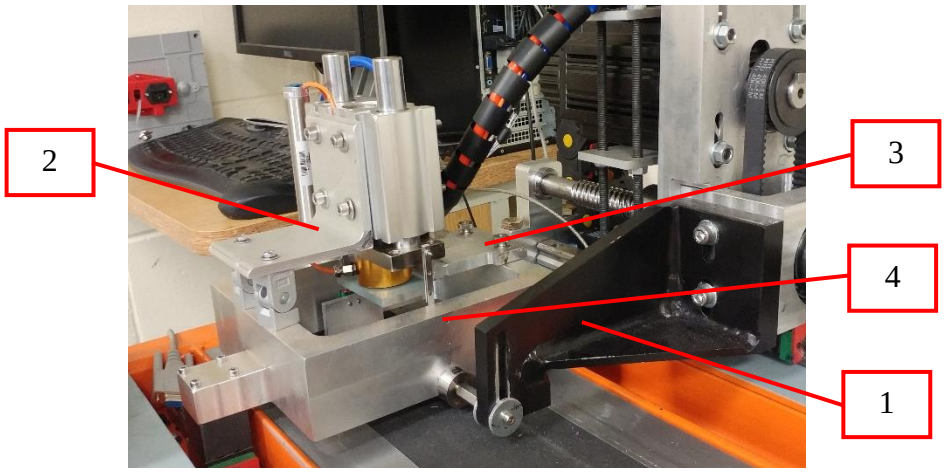

Figure 3-16: 1. Carriage 2. fixture base 3. fixture door 4. inner fixture

3.2.3.14 Linear guides _Track raising pneumatics

Two linear guides allow the carriage to move freely down the length of the table. One bearing is used on each 2400mm rail to support the carriage.

3.2.3.15 Cylinders

The rails are not attached to the table; instead, they are attached to the ends of five pneumatic cylinders, as shown in Figure 3-17. Each cylinder has a 16mm diameter piston and is capable of applying a 500N force. Each cylinder is fixed to the bottom of the table

Figure 3-17: 10 Pneumatic cylinders for raising the track. The cylinder housing is bolted to the bottom of the table, and the cylinder is free to pass through holes in the table, moving the linear guides and carriage upward.

with 4 M5 bolts and the track with one M4 bolt on the end of the piston. They are supplied with air from the same source as the pneumatic cylinder that provides the normal load. The air supply is turned on or off using solenoid valves to raise or lower the linear guides, carriage, and sample.

3.2.3.16 Scale

A US Solid USS-DBS15 scale, shown in Figure 3-18, is used to measure the mass of the sample. This scale has a maximum capacity of 300 g, a resolution of 1 mg, and repeatability and linearity of ±2 mg. The scale allows for the mass of the rubber sample to be measured between trials. An RS232 serial connection to a PC is used to record data from the scale easily.

Figure 3-18: Scale located at the end of the table.

3.2.3.17 Table

As shown in Figure 3-19, the table's frame is composed of 2 inches by 2690 mm wall square tubing, 2in by 4in by 2690 L-angle. The tabletop is 0.5 in thick steel. All parts are welded together. The legs are fixed to the ground using eight thick L-angle brackets. The brackets are attached to the legs with ¼ in bolts and the ground with ¼ in concrete anchor bolts. These leg fixtures reduce vibrations in the table when tests are being run.

To conduct the tests for sliding the rubber on different surfaces, sandpapers with different roughness grades were placed on the linear friction tester's surface using high-strength glue.

Figure 3-19: Frame of linear friction tester

3.2.3.18 Electrical Box

Figure 3-20 shows the electrical box for operating the test setup. The electrical box has several parts, including the DAQ, fuses, solenoid valves, proportional valve, and servo driver. Detail description of each part is provided in the Appendix.

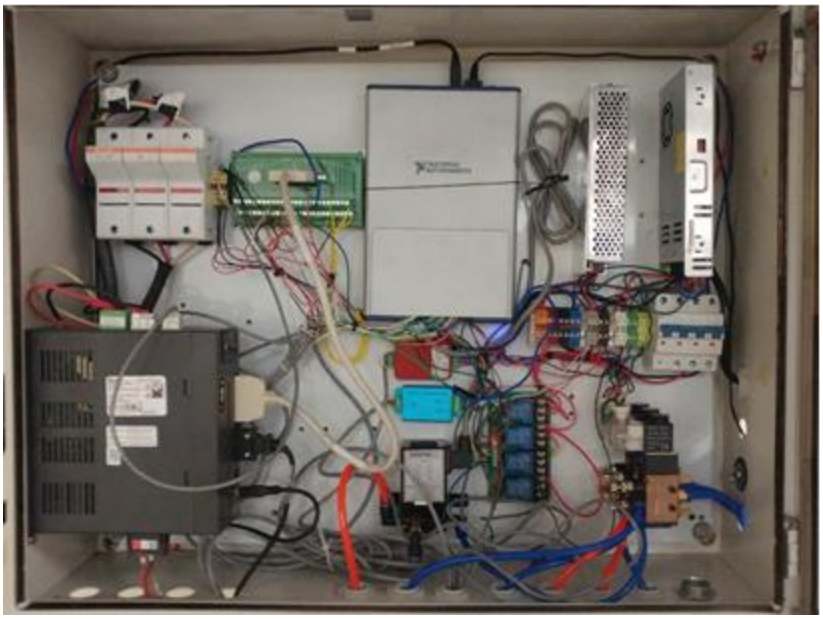

Figure 3-20: Electrical box with important components

3.2.4 Advancements on LFT

The new linear friction tester designed for this study has several advantages compared to the existing test setups for measuring the friction and the wear rate of the rubber. The summary of these advantages is mentioned here:

- New LFT has an adjustable normal load using a proportional valve and pneumatic cylinder.
- It has an Efficient design for easy mounting and replacing the sample.
- LFT is a high-accuracy testing machine by implementing a ball screw.
- Feasibility for continuous testing using ten pneumatic cylinders.
- Capable of testing on different surfaces (dry/wet).
- Capable of automatic weight measurement after each run.
- More realistic results by implementing the special design to remove the pitch that occurred toward the sample's leading edge.
- This design is capable of automatic self-cleaning after each run.
- Capable of measuring the contact patch and temperature of the contact between the rubber sample and surface.

A pitch toward the leading edge of the sample was observed during the tests. According to the feedback that we received from the companies, this phenomenon does not happen for the real tread section on the tire. Three approaches were followed to remove this extra pitch and solve the issue: first, four linear bearings were used to restrict the inner fixture moment. 4 MGN7c linear bearings and 2 MGN5H linear bearings were used to eliminate the moment

imposed on the sample. Then, the larger area of the rubber sample was fixed using the fixture sample's new design to decrease the shear force and moment on the sample.

Finally, the around edge sample was used to reduce the shear force and moment on the sample. Figure 3-21 shows the new design considered for this test setup. Figure 3-22 shows the results obtained after modifying the design.

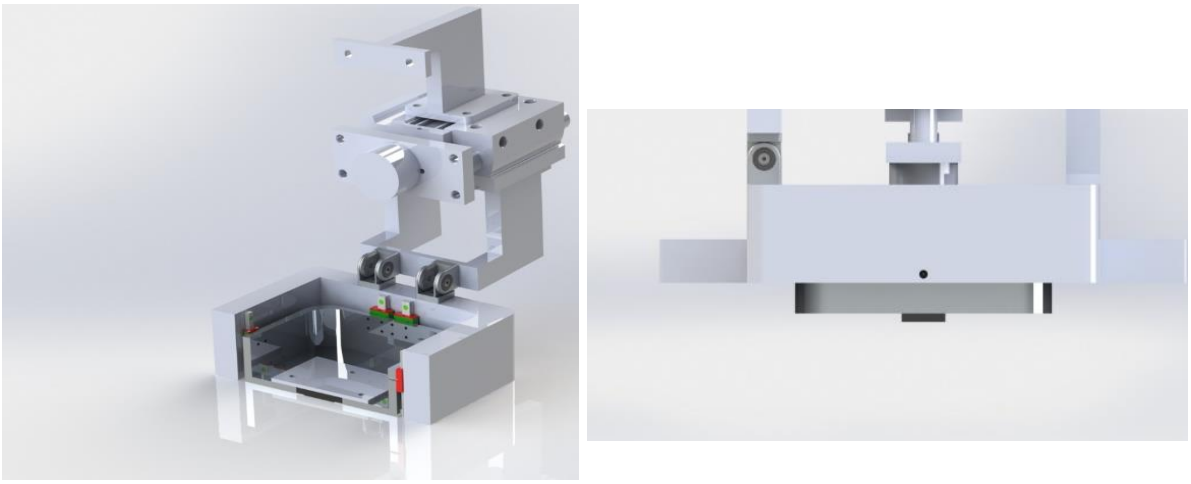

Figure 3-21: New design of the fixture to solve the problem of the pitching

As shown in Figure 3-22, the geometry of the sample after the modification is changed. The results obtained were compared with the results from the finite element modeling. As shown in Figure 3-23, the pitch toward the sample's leading edge was reduced by applying the modifications.

Sample A
Modified linear Friction tester

Sample A
Original design of the linear friction tester

Figure 3-22: Comparison between the wear pattern of the samples before and after the design modification

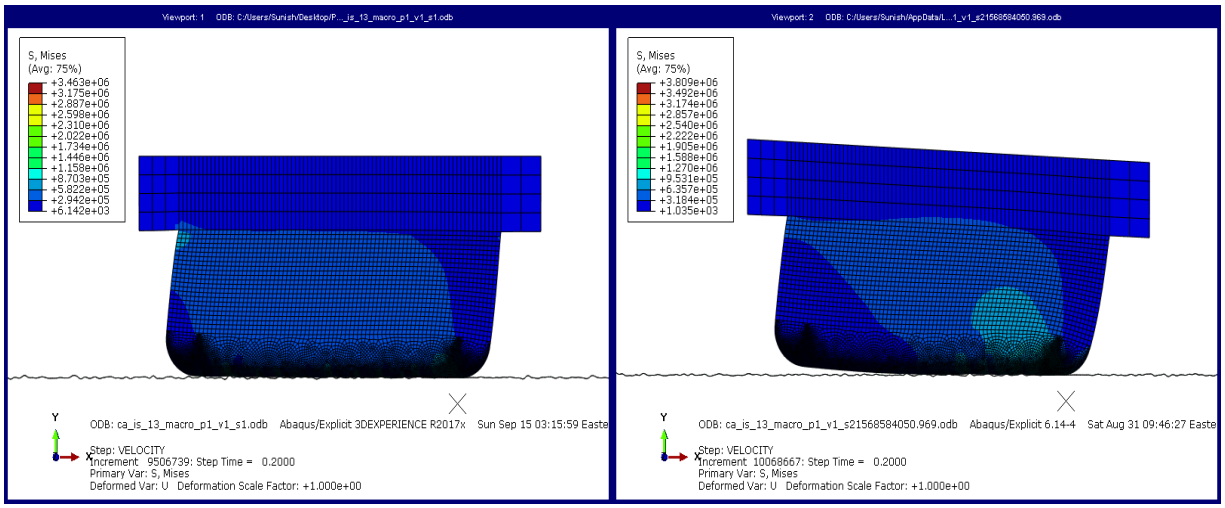

Figure 3-23: Results from the finite element modeling [64]

3.2.5 Testing procedure

In this section, a brief description of the testing procedure is presented. For conducting a test, these steps should be followed:

1. The sample will be mounted on the carriage. (Figure 3-24)

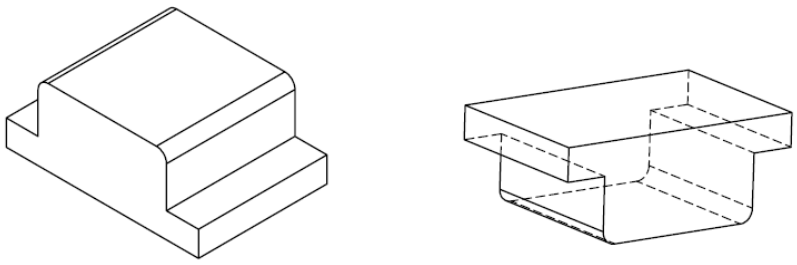

Figure 3-24: the rubber sample used for linear friction tester

2. Carriage with a sample is returned to the origin with linear guides in the raised position.
3. The guides are lowered, and the normal load is applied to a sample.
4. Servo starts to rotate and move the carriage to Position 1 with constant speed.
5. Once Position 1 is reached, the servo stops, the normal force is released, and linear guides are raised.
6. The servo moves the carriage to Position 2.
7. Linear guides are lowered, and the sample settles on the scale. Scale sends mass to the PC.
8. Linear guides are raised, and the servo moves the carriage back to the origin.
9. Steps 2-7 are repeated until a digital input or emergency stop ends the loop.

After testing the rubber samples on the linear friction tester, rubber debris covered the simulated road surface. To obtain accurate and controlled results, this surface must be cleaned of debris during tests. It was desired to automate this clean-up process, so the existing compressed air system was utilized to operate a brush and vacuum combination. Cleaning was done with a pneumatic cylinder that would lower a strip brush into contact with the surface in tandem with a vacuum funnel attached to the testing fixture routed to a shop vac.

A vacuum head and brush can be attached to the carriage's trailing face (Figure 3-25) to remove rubber particles that were shed from the sample. The brush is pressed into the table with a pneumatic cylinder at 100 N.

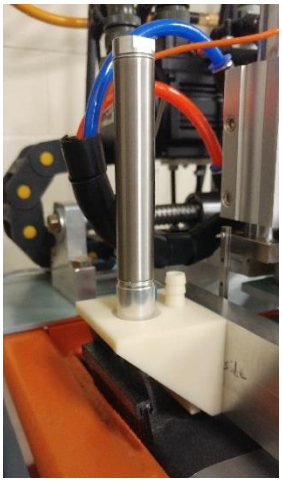

Figure 3-25: Brush and pneumatic. A nozzle to mount a vacuum to is also visible to the right of the pneumatic

The ¾ in bore 3in stroke double-action pneumatic cylinder and the two positions four-way solenoid valve were acquired from Automation Direct. 1/8in NPT elbow push connectors with tubing were reused from the original build.

In order to route the vacuum through the cable carriage, the hose was dropped from the 3 in shop vac hose to ½ in inner diameter PVC tubing. This was done with a custom-designed

and 3D printed attachment that slid over the existing hose and possessed a nipple that was inserted into the PVC tubing, as shown in Figure 3-26.

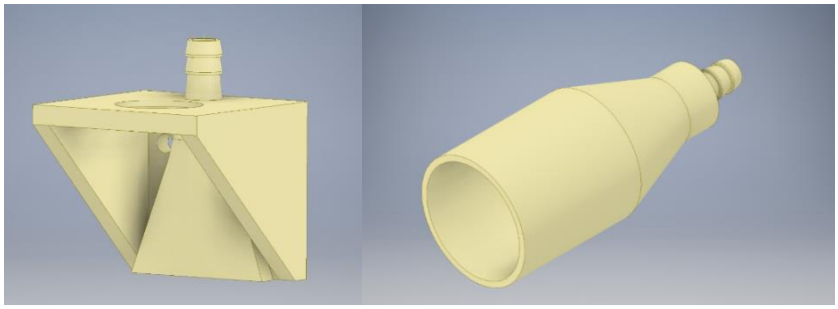

Figure 3-26: a. part for the head of the vacuum system b. the connector between shop vac hose and PVC tubing

Secondly, a custom piece was designed that combined the ending vacuum funnel with the fixture that would hold the cylinder. (Figure 3-27)

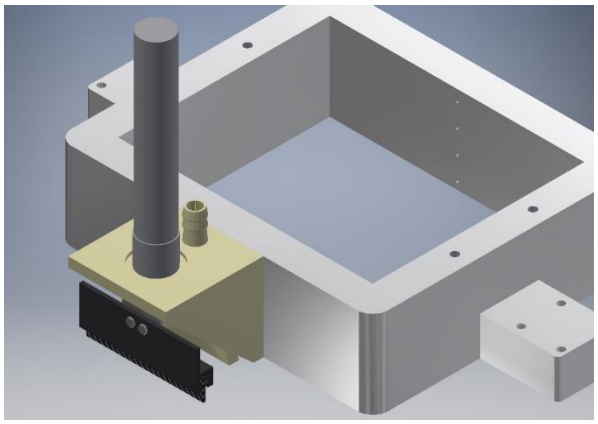

Figure 3-27: Piece for hold the cylinder

3.2.6 Design of experiment

Table 3-3 shows the design of the experiment, which is used for the study on the wear rate and friction of the rubber with different material properties as well as different operational

conditions. As shown in Table 3-3, two types of rubber compounds, three levels of normal pressure, five different velocities, and three different types of surfaces were chosen for the tests. The results obtained for this study are shown in section 3.2.7.

Table 3-3: Design of experiment for linear friction tester

Linear Friction	
Sample type	A, B
Normal-pressure	0.1, 0.15, 0.2, 0.25, 0.3, 0.4 MPa
Velocity	5, 10, 20.50, 100
Surface	Sandpaper 120

3.2.7 Results for wear and friction

In this section, the data collected by the tests conducted according to the design of the experiment table for the wear rate and friction for two rubber samples are presented. The rubber sample was run five times in order to remove the sharp corner in the leading edge of the sample before performing the actual test. First, to show the linear friction tester outputs, a set of sample results for the applied normal load obtained from the experiment is presented in Figure 3-28 and Figure 3-29. As shown, the normal load at each run has minimal variation due to the highly accurate proportional valve used to control the normal load dynamically.

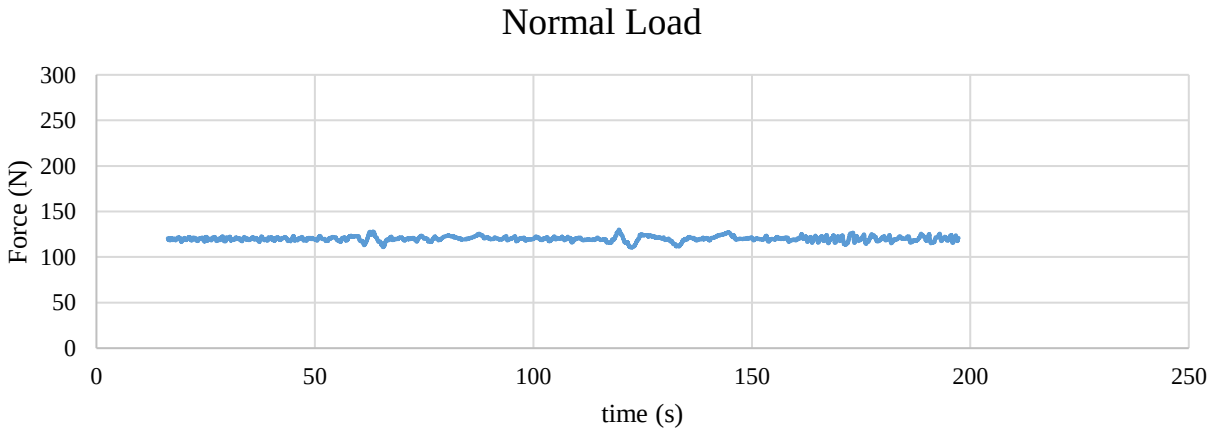

Figure 3-28: Dynamic normal load applying on the sample in one run with velocity 5 mm/s

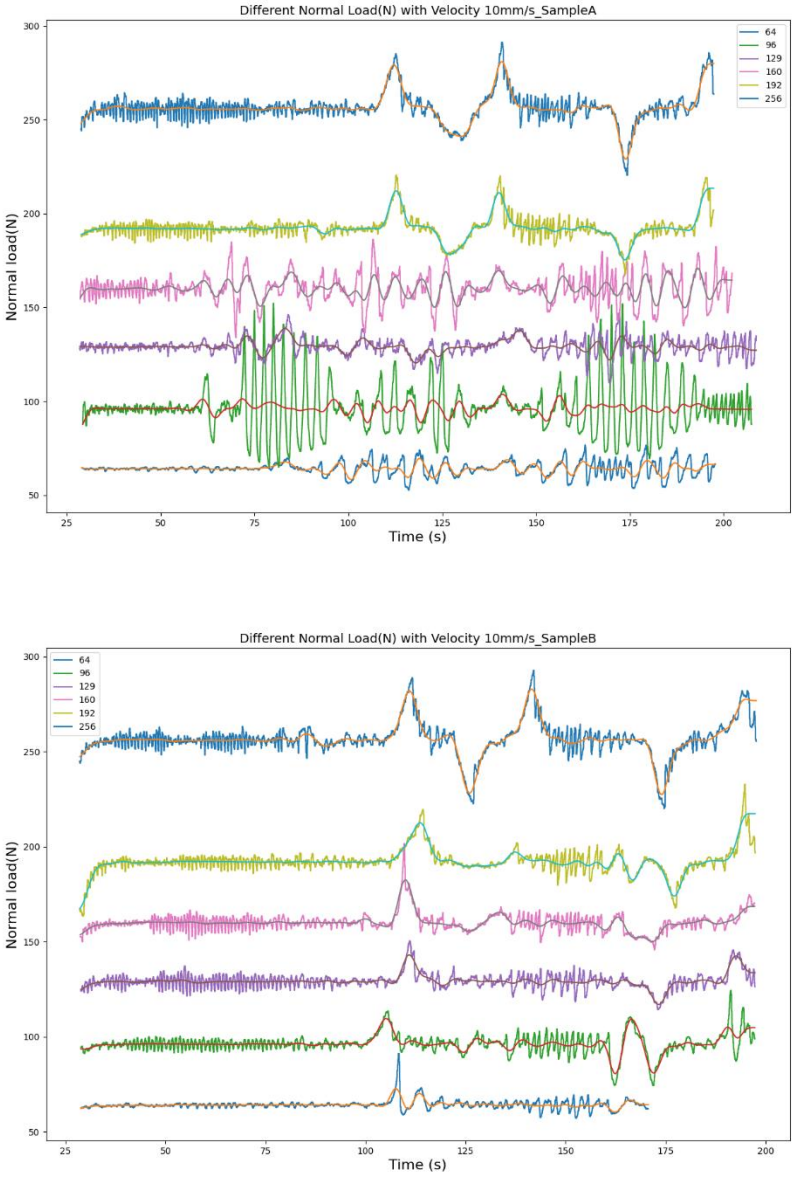

Figure 3-29 Dynamic normal loads applying on the sample A and B with 10mm/s velocity

For testing with Linear Friction Tester, the rectangular rubber sample with a length of 1 in, a width of 1 in, and a height of 0.314 in was used. Figure 3-31 shows how friction coefficient changes over time for component A at 0.2 MPa normal load and 0.01m/s velocity on sandpaper grit 120. Figure 3-30 depicts the friction coefficient for six continuous runs, where the distance for each run is around 2 m. Figure 3-31 and Figure 3-30 illustrate the gradual increase of friction coefficient over time. This is caused by the increase in the rubber sample's temperature over time due to the frictional heating when the rubber sample is in contact with the sandpaper.

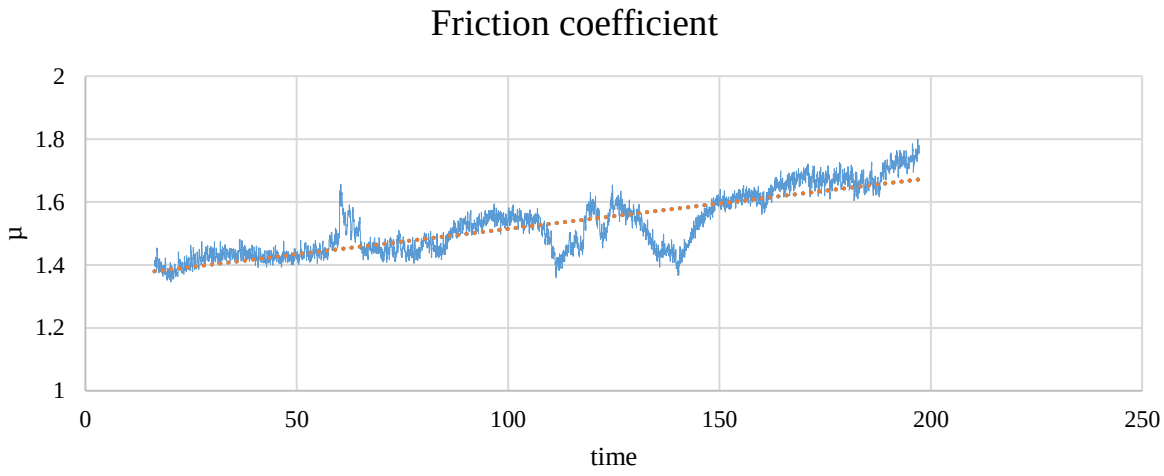

Figure 3-31: Friction coefficient over time

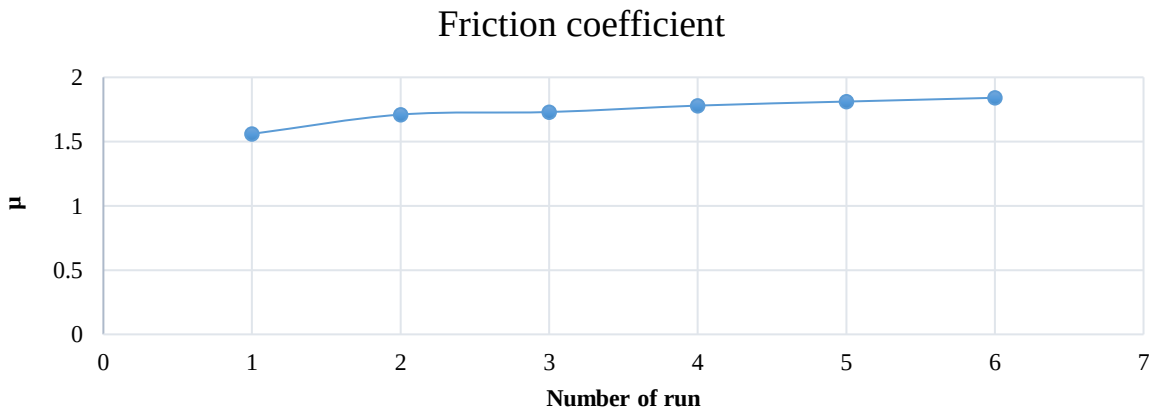

Figure 3-30: Friction coefficient for six continuously run

Figure 3-32 and Figure 3-33 illustrated the friction force and friction coefficient for different normal loads with velocity 10mm/s on sandpaper 120 grit for samples A, B. As can be seen by increasing the Normal load friction force increased; however, the friction coefficient decreased.

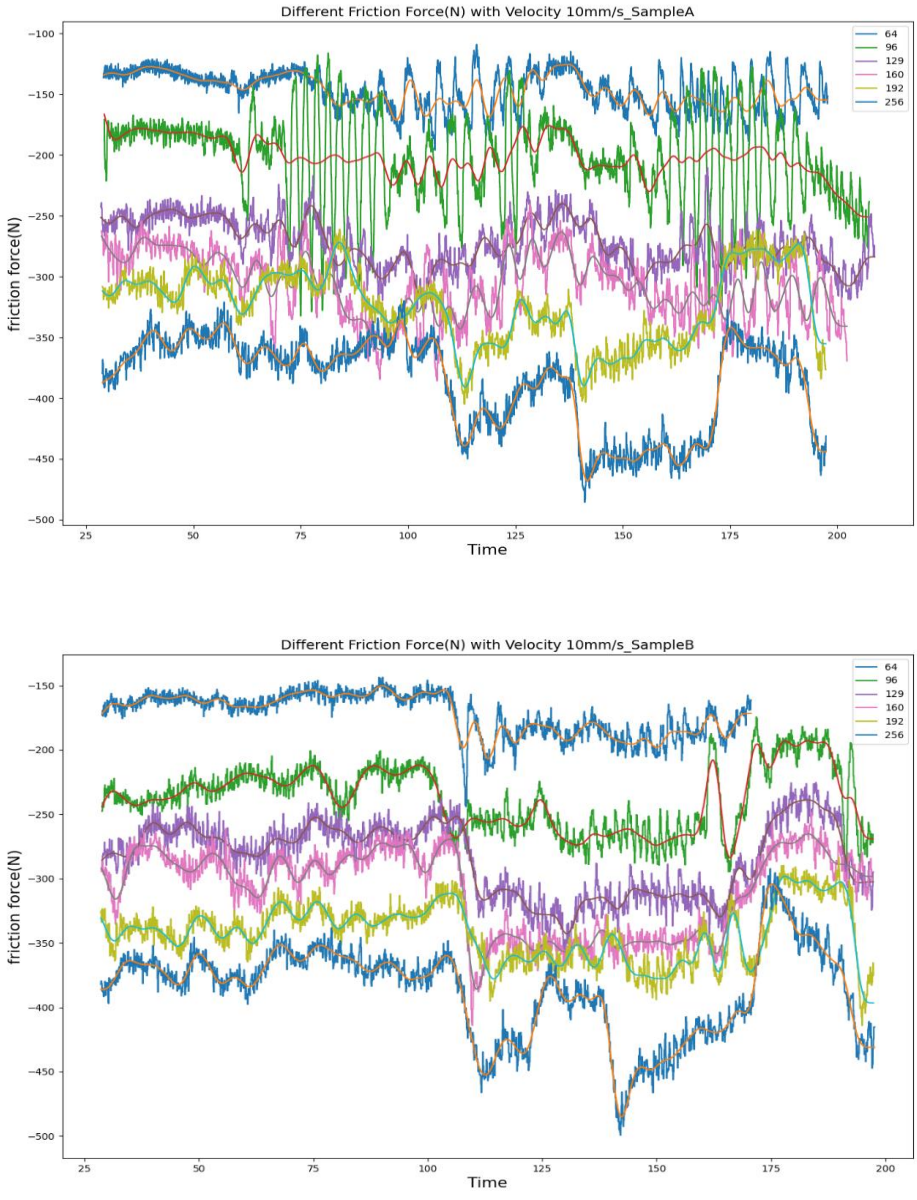

Figure 3-32: Friction force during the time for different loads with a velocity of 10 mm/s for samples A and B

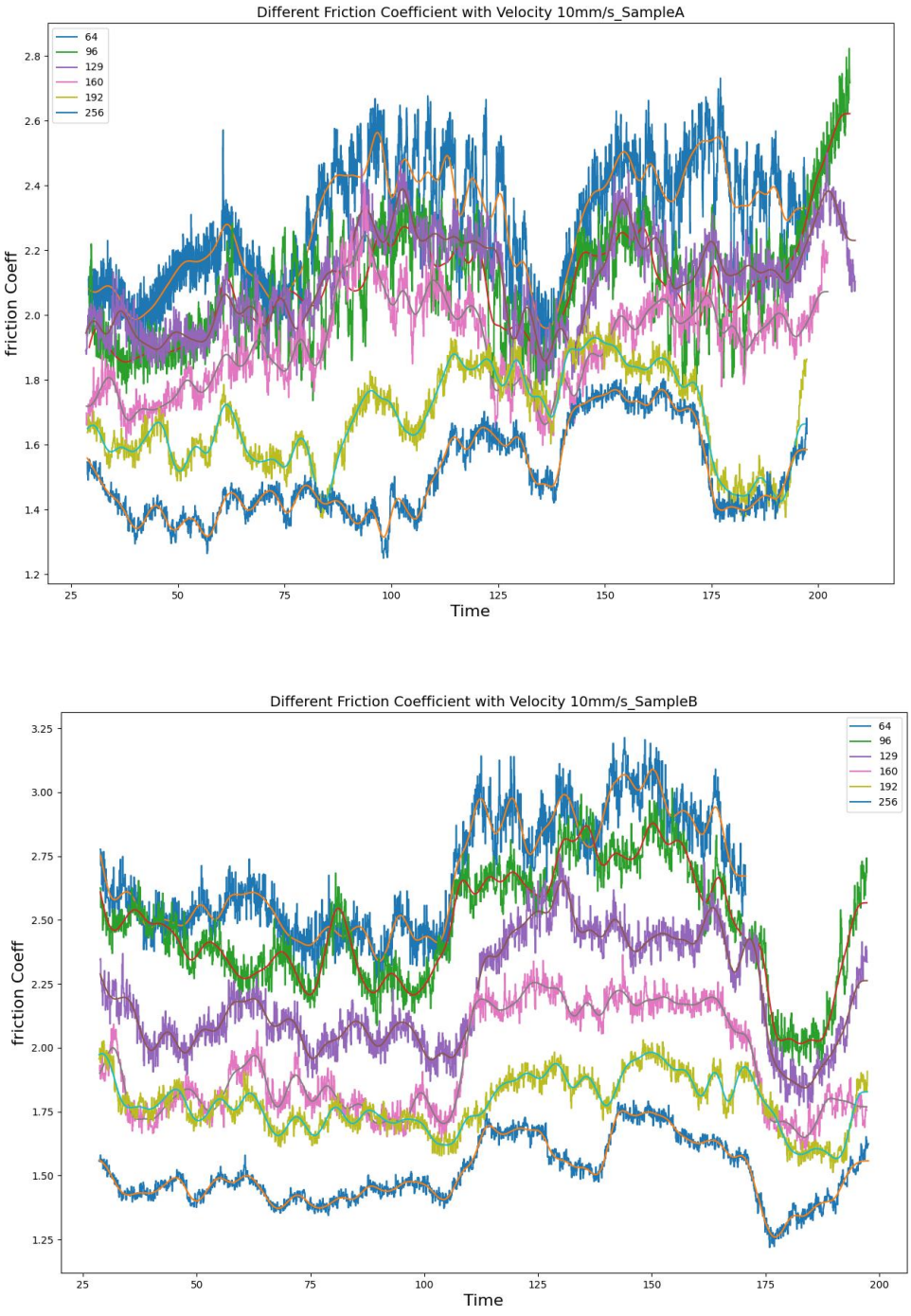

Figure 3-33: Friction coefficient during the time for different loads with a velocity of 10 mm/s for samples A and B

As shown in Figure 3-34 and Figure 3-35, by increasing the velocity, the rubber sample's friction coefficient increases gradually and goes to a maximum; then, the friction coefficient decreases by increasing the velocity as expected. The main reason for this phenomenon is that the breaking of the interfacial bonds, which caused thermal fluctuation within the contact area, reduces adhesive friction. Adhesive friction is developed due to the interaction between the molecules of two surfaces. The adhesive part of friction in very low sliding velocities of the rubber is small. The adhesive part of the friction will decrease for higher speed by increasing the rubber movement's speed or using lubricant. Therefore, the maximum value of the friction coefficient must happen at intermediate velocities. This intermediate velocity is changed by changing the operational condition of the test.

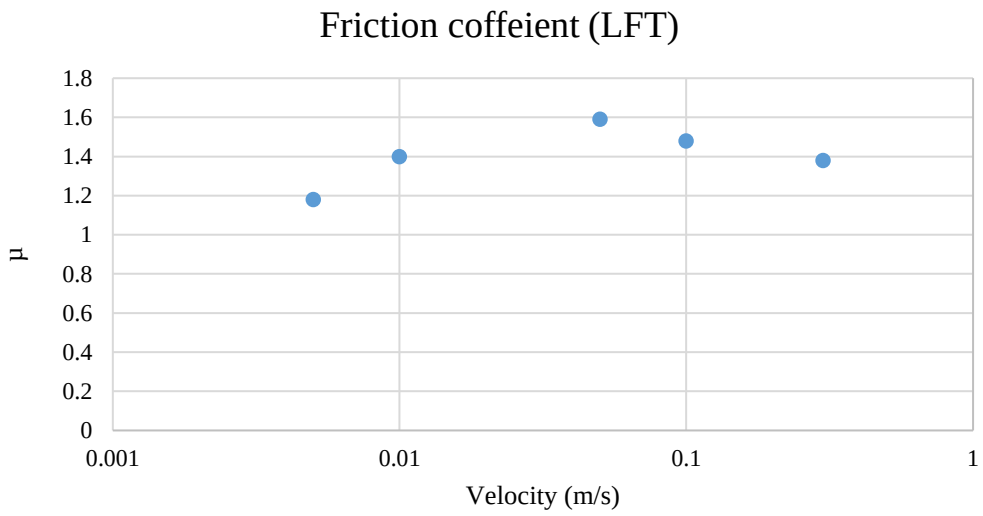

Figure 3-34: Friction coefficient obtained by Linear Friction Tester

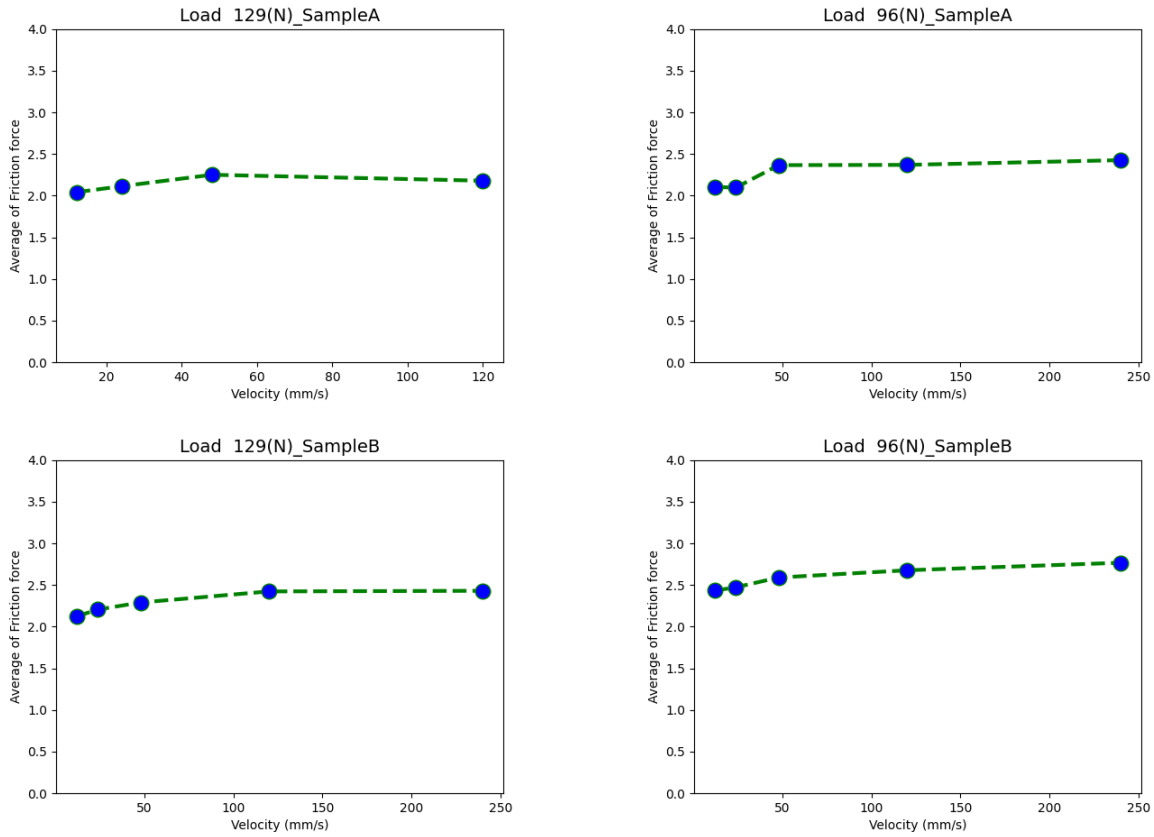

Figure 3-35: Friction coefficient obtained by Linear Friction Tester in different velocities for samples A and B

The effect of the change in the normal load on the friction coefficient values is illustrated in Figure 3-36 and Figure 3-37. As the friction coefficient has a reverse relation with the σ_0 (normal load), a decreasing trend will be observed for the values of the friction coefficient. Also, as these figures show, sample B has more dependency on pressure comparing with sample A. In addition, the nonlinear relationship between pressure and friction coefficient is apparent in these graphs.

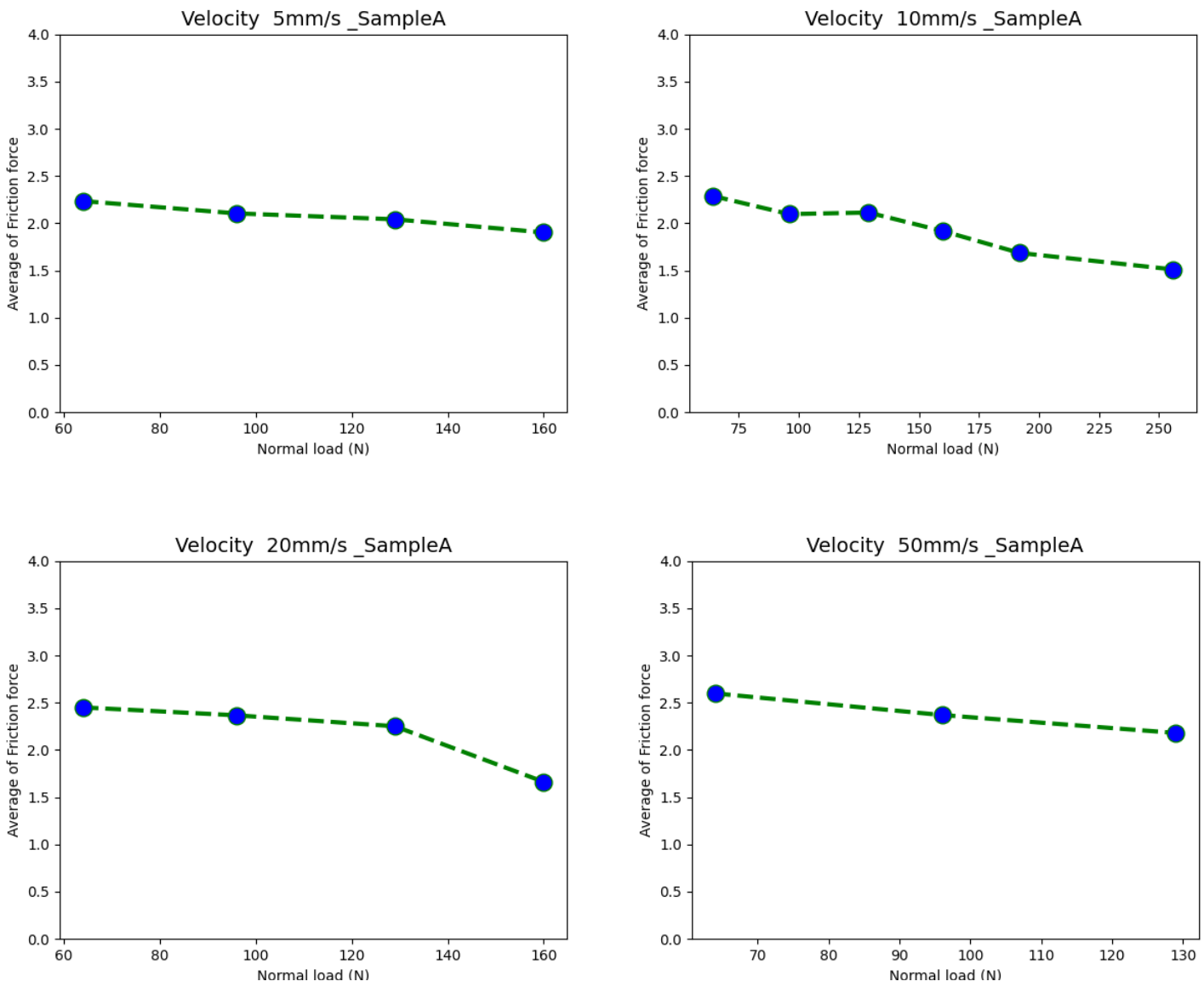

Figure 3-36: Effect of normal load on friction coefficient for sample A in different velocity

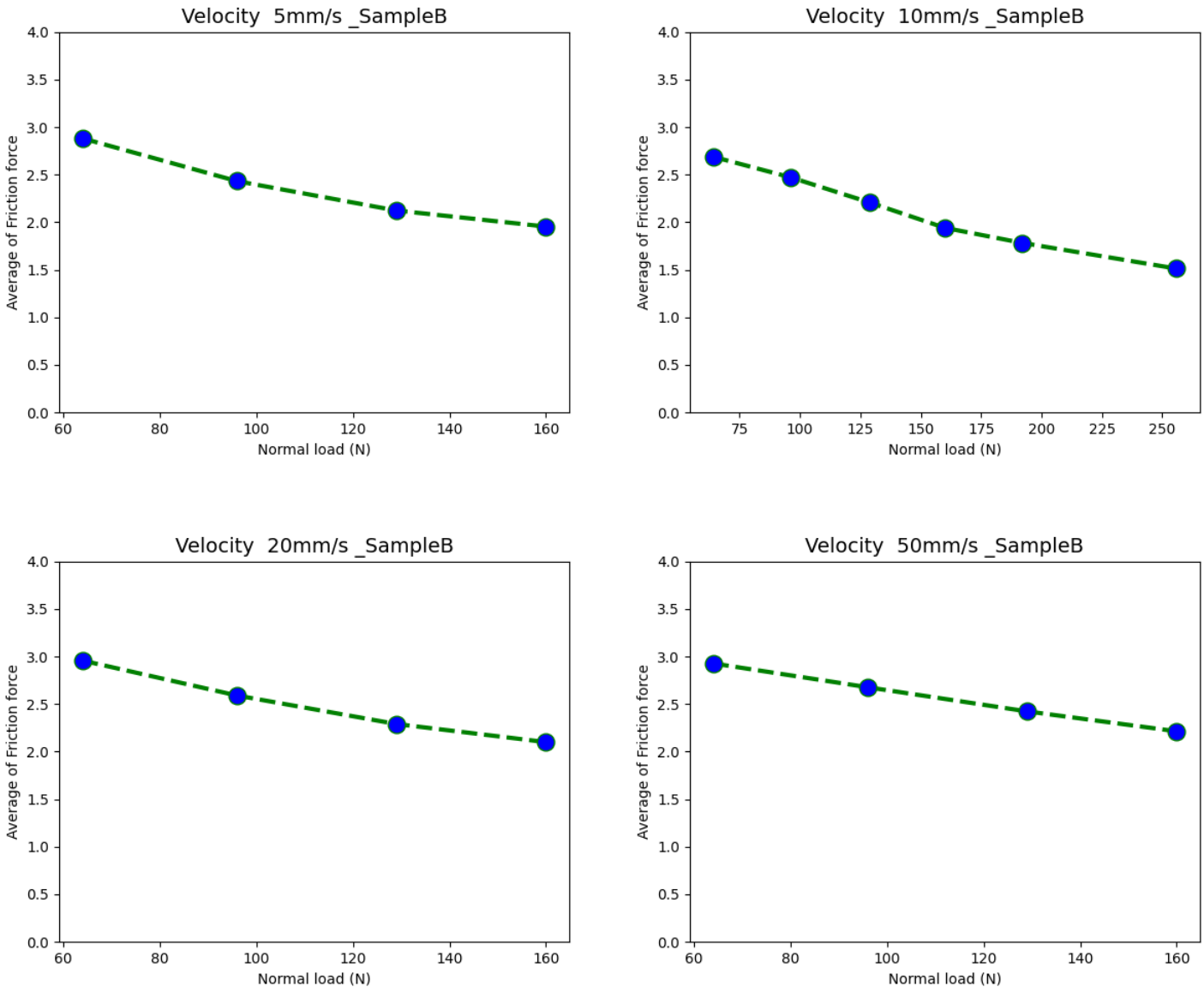

Figure 3-37: Effect of normal load on friction coefficient for sample B in different velocity

Figure 3-38and Figure 3-39 Show the effect of normal load on the wear rate of samples A and B on sandpaper 120 Grit. As seen, by increasing the normal load, the measured wear rate of both samples increases. In addition, as shown in these figures, changing the applied normal load has a higher impact on the values of sample B's wear rate than sample A.

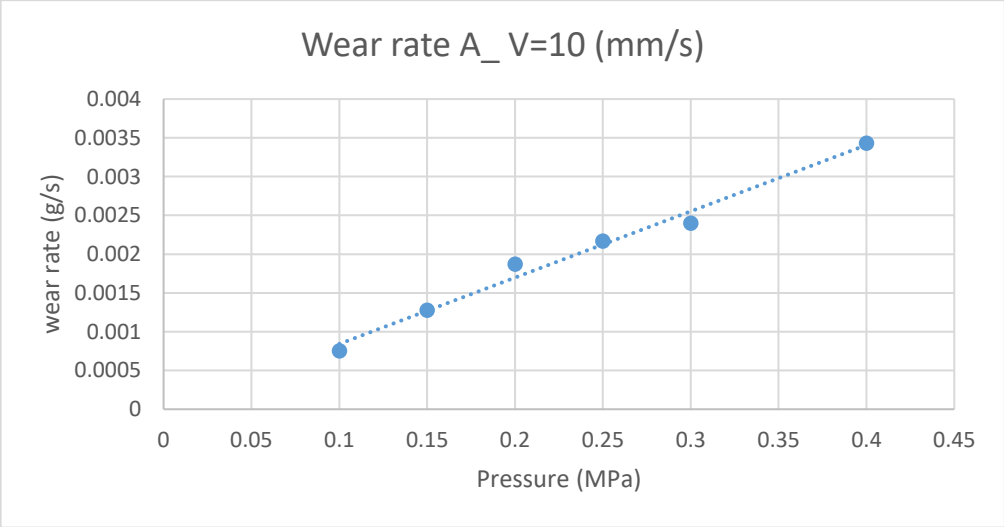

Figure 3-38: Wear rate for sample A on sandpaper 120 grit with10mm/s sliding velocity

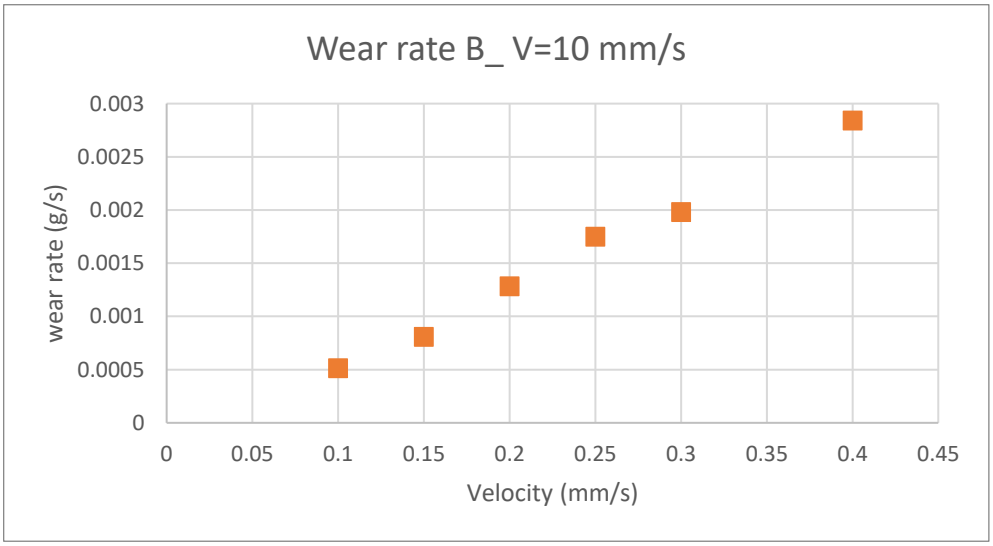

Figure 3-39: Wear rate for sample B on sandpaper 120 grit with10mm/s sliding velocity

A linear friction tester measured the wear rate of sample A in different normal loads in 5 different velocities at room temperature on the sandpaper grit 120 (3M) with a back stick. The data collected is shown in Figure 3-40 and Figure 3-41. As expected, by increasing the sliding velocity, the wear rate increases. The tests were conducted for sample A under different applied normal loads. Figure 3-41 shows the effect of change in the applied normal load and velocity in the same graph. Based on the presented graph, by increasing the normal load, the speed has more powerful impact on the values of the wear rates.

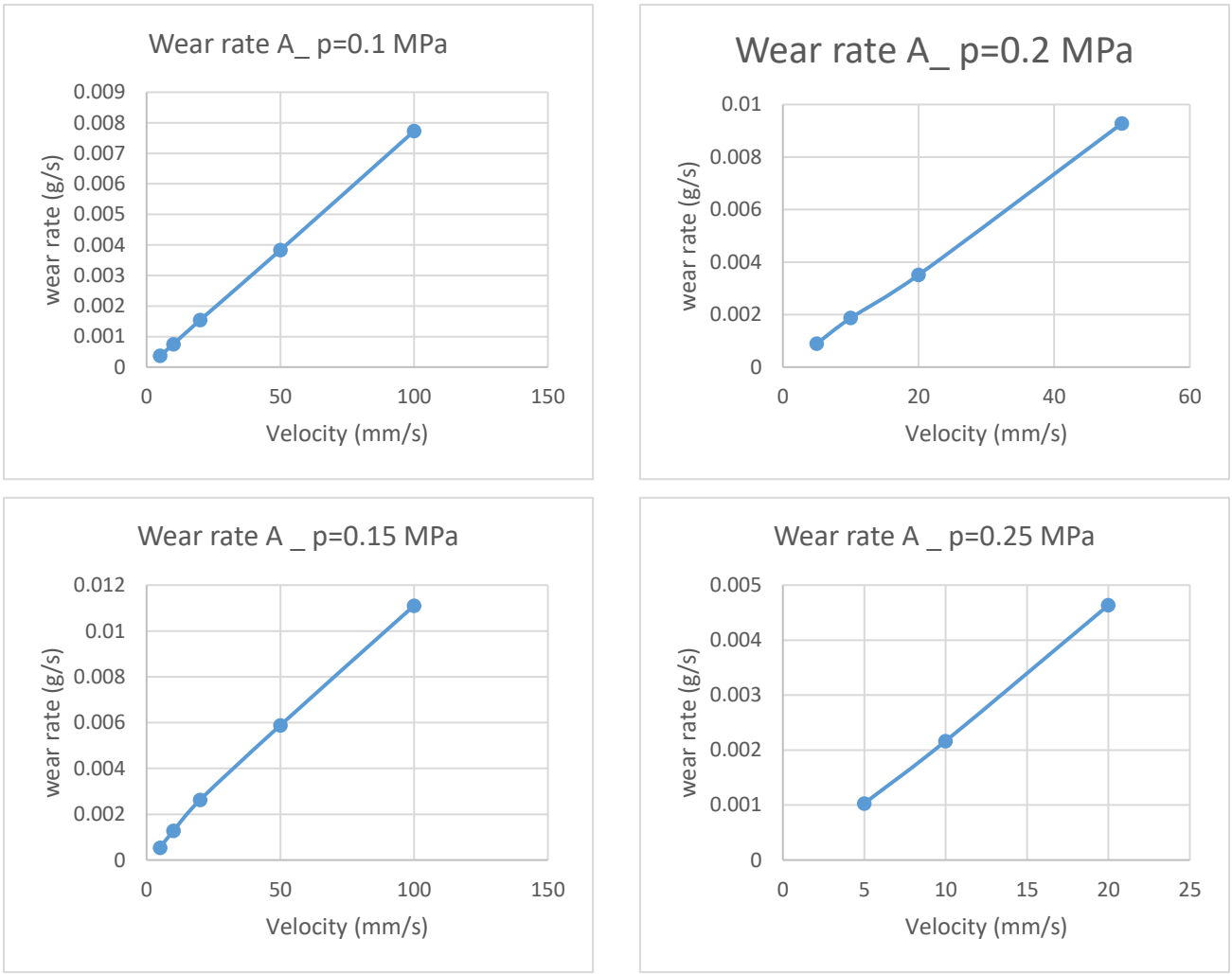

Figure 3-40: Wear rate of sample A in different velocity and contact pressure

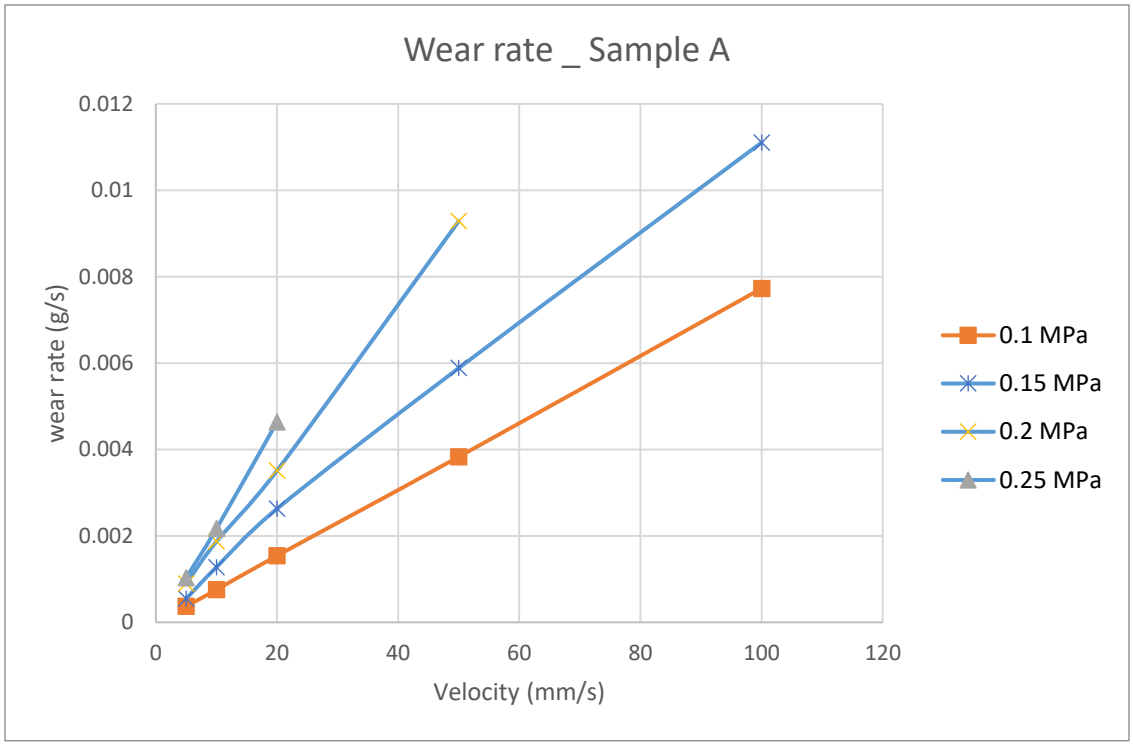

Figure 3-41: Wear rate of sample A in different velocity and contact pressure

Figure 3-42 and Figure 3-43show the data collected for the wear rate of sample B under different applied normal loads for five different velocities at room temperature on the sandpaper grit 120 (3M). The data was obtained using the linear friction tester. Similar to the data collected for sample A, the wear rate increases by increasing the sliding velocity. This is true for all applied normal loads were choosing for this study. In addition, the data collected from the test conducted under a higher value of the normal load shows a more noticeable change in the values of the wear rate when speed increase.

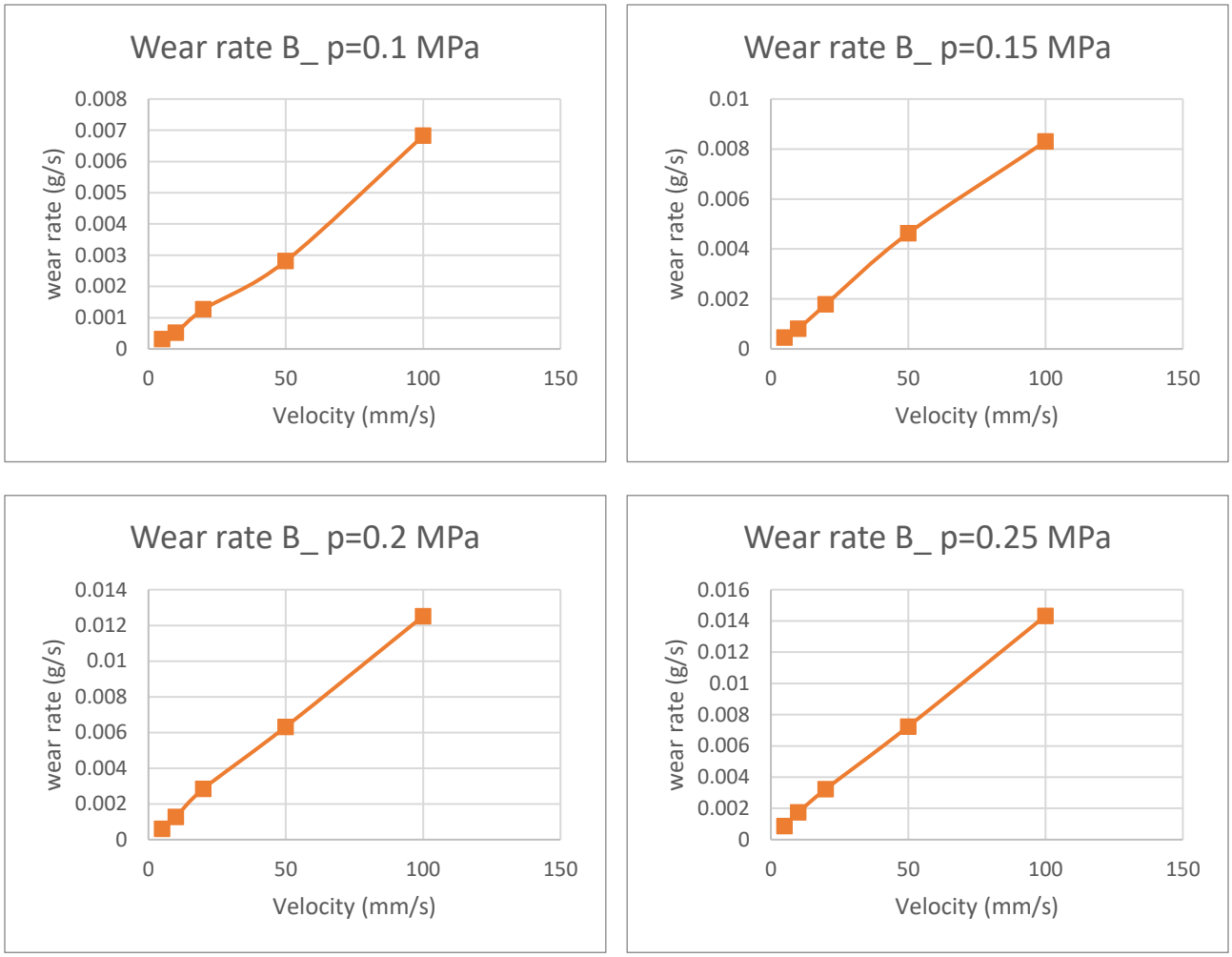

Figure 3-42: Wear rate of sample B in different velocity and contact pressure

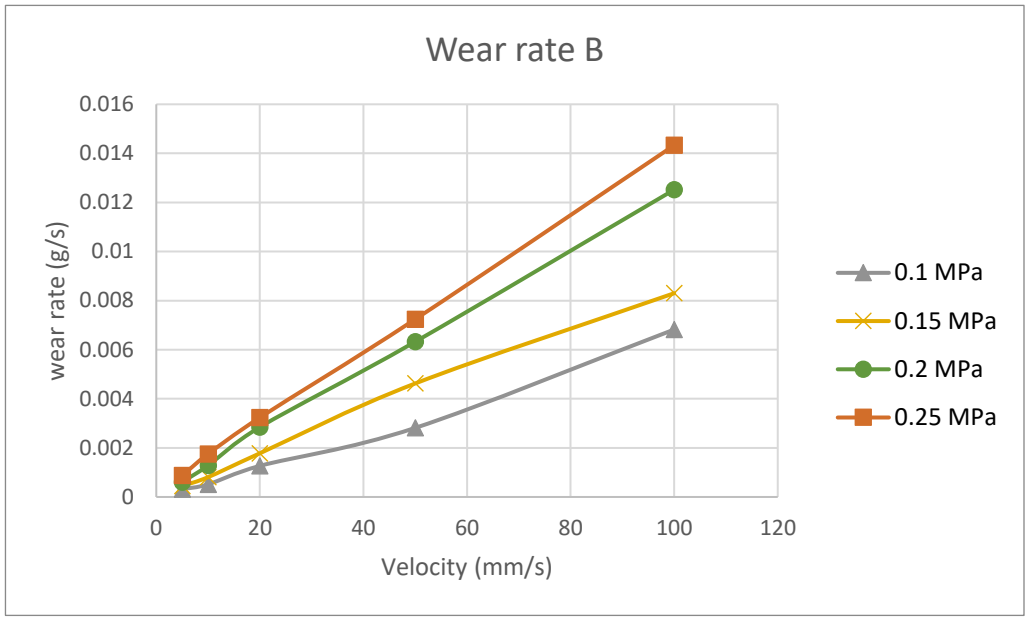

Figure 3-43: Wear rate of sample A in different velocity and contact pressure

Figure 3-44 is presented to compare the wear rates of samples A and B for different testing conditions. As shown, in all DOE cases, the wear rate of sample A is higher than the wear rate of sample B. In addition, based on the slope of the graphs, the dependency of the wear rate to the velocity is higher for sample A.

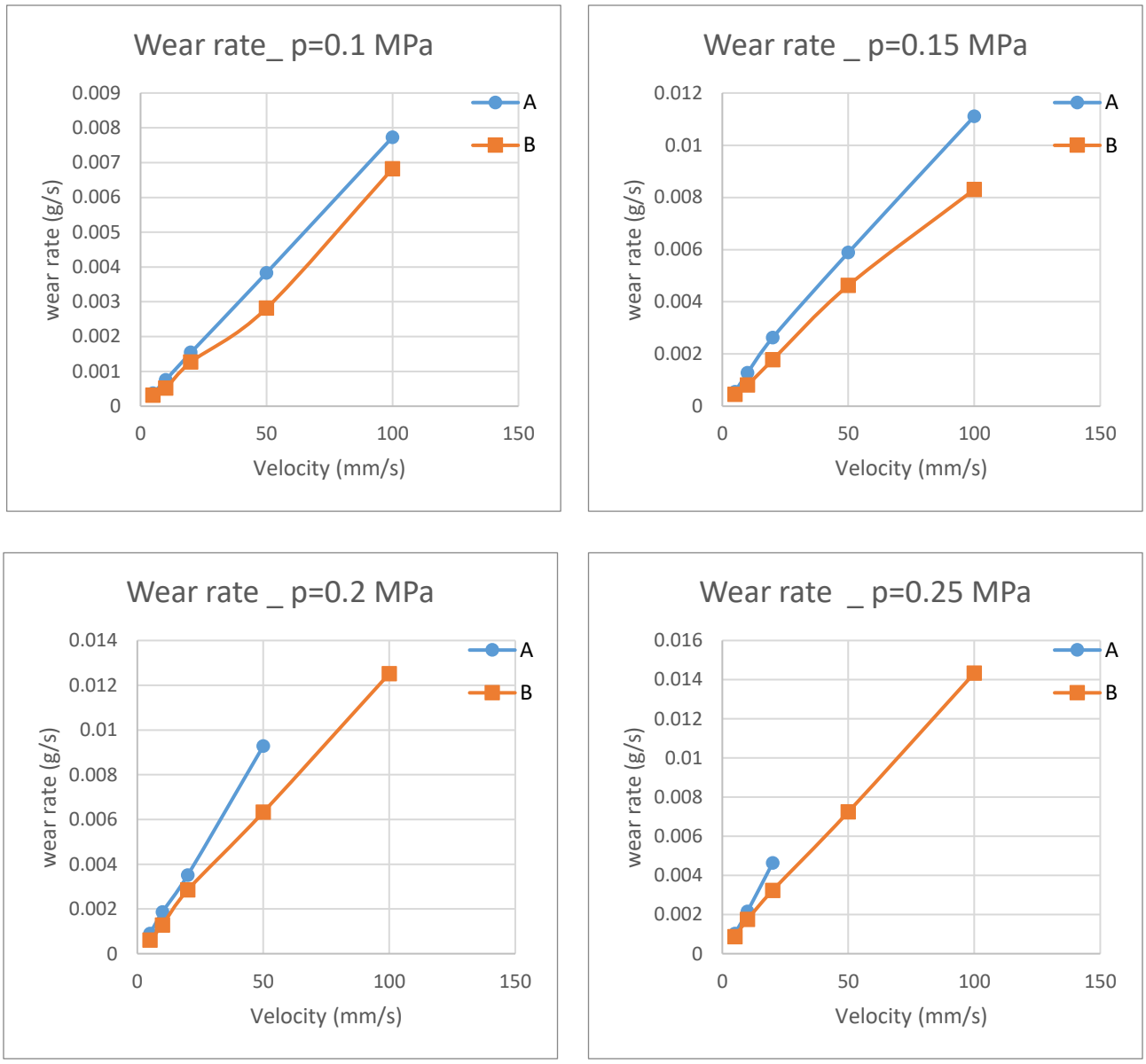

Figure 3-44: Wear rate for samples A,B in different velocities and pressures

3.2.8 Validation of the data collected using the linear friction tester.

After completing the linear friction tester's design and manufacturing, the test setup needed calibration and validation. To calibrate and validate the test setup, the data collected by the linear friction tester were compared with results collected by the dynamic friction

tester.

For the calibration and validation step, several tests were conducted for rubber sample A for different velocities and normal pressures in order to find the sliding friction coefficient. The results obtained are compared with the data collected using the dynamic friction tester in Figure 3-45. As shown in this figure, the data collected by the linear friction tester is in agreement with the data collected using the Dynamic Friction Tester. In addition, the results obtained by the linear friction tester are compared with the results obtained from the analytical approach explained in chapter 4.

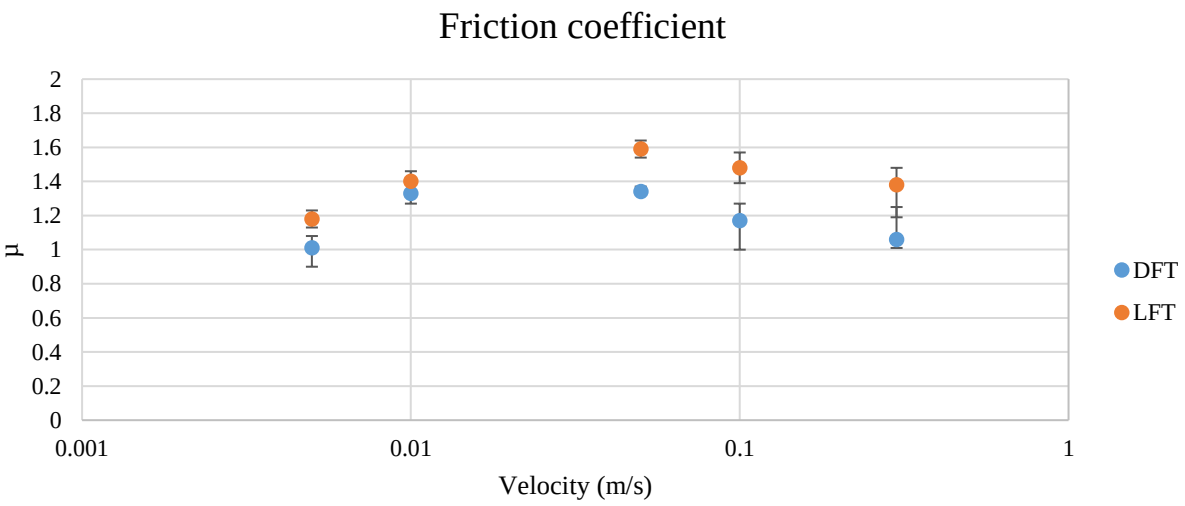

Figure 3-45: Comparison between the data obtained by linear friction tester and Dynamic friction tester on sandpaper grit 120

Figure 3-46 indicates the rubber sample patterns after five initial runs, which was for removing the sharp edge of the sample. Figure 3-46 b, c, and d show the rubber block sample after sliding on sandpaper grit 120 for 2, 4, and 6 runs, respectively. The distance of each run is around 2 meters.

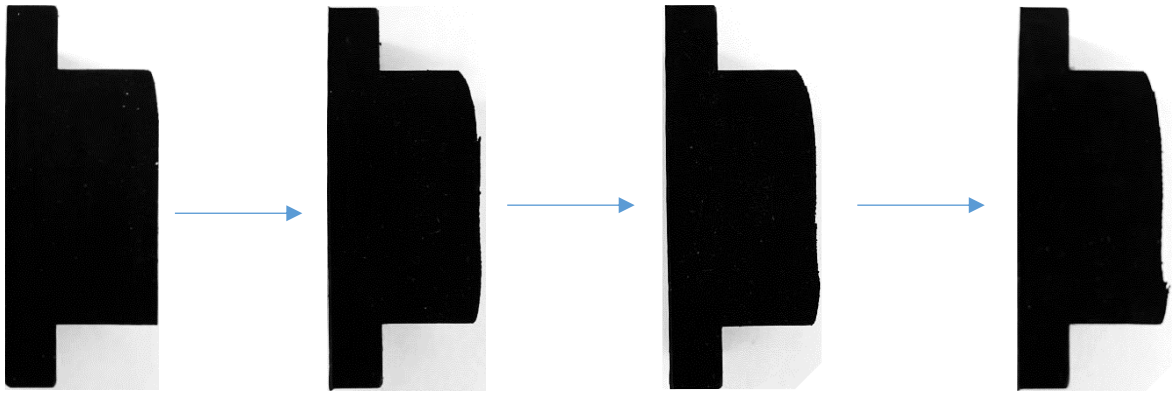

a) After 5 initial b) After 2 c) After 4 d) After 6

Figure 3-46: Wear rate of tread block

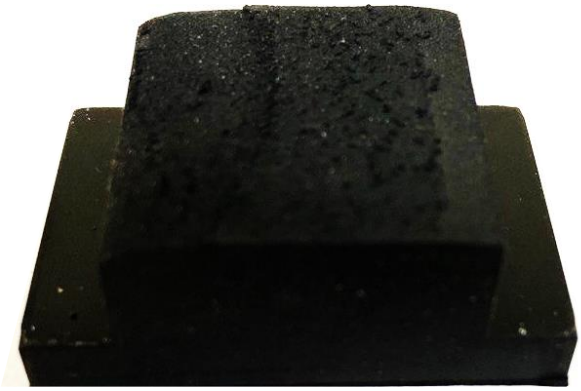

Figure 3-47: Wear rate pattern of tread block

Chapter 4

Analytical Modeling

This section presents the methodology for developing an analytical model to predict the wear rate and friction for material in contact with a rough surface. As explained in the literature review section, friction coefficient and the wear rate can be defined for two materials in contact with each other.

In order to obtain the wear rate of the rubber using an analytical approach, the first step is calculating the real contact area and friction of the rubber. There are several empirical, theoretical, or semi-analytical approaches to predict the friction coefficient. The Persson model presents acceptable results for the rubber's friction coefficient in contact with the rough surface among the existing methods. The Persson model results were improved by A.Emami [9] by removing the errors caused by the previous estimation of the real contact area. To improve the results for predicting the real contact area, she calculated the original height profile using a new approach. In this approach, the large distance between the terrain asperities that do not have any contact with the deformed material and thus do not contribute to the displacement field's value can be eliminated.

In order to obtain the real contact area, it is needed to have the data for the surface characteristics. To obtain this data, a Profilometer can be used. Another approach to obtaining the required data for the surface uses the theoretical model to simulate a surface using a random surface approach to obtain the power spectrum density. The simulation creates the surface to obtain the friction coefficient and the real contact area.

After obtaining the friction coefficient and the real contact area, the rubber's wear rate is calculated. There are several methods to obtain the wear rate of the rubber. Persson Powdery Rubber Wear's theory is one of the popular analytical approaches to estimate the wear rate. Despite this method's popularity, this approach's results are not as accurate as they should be. In order to improve the results of this method, a novel approach is implemented in this study. In this approach, the author combined the Persson Powdery Rubber Wear model with the Crack Propagation model. The results of the improved model are presented in this section.

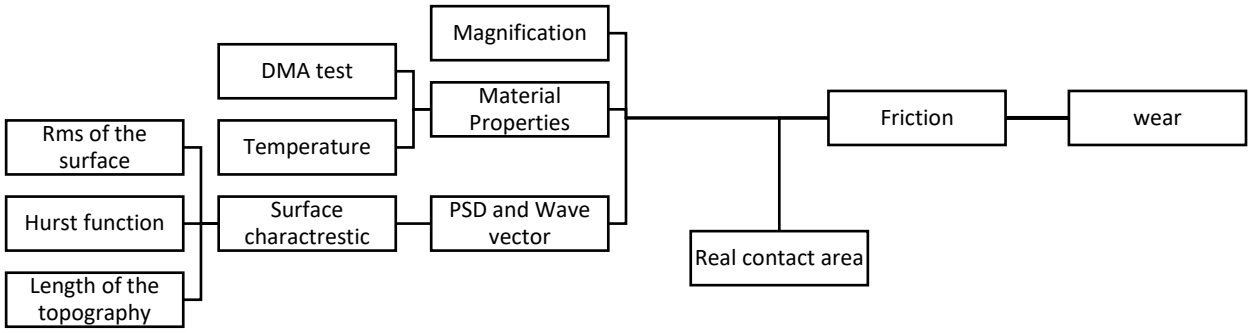

Figure 4-1: Analytical approach to obtain friction and wear

4.1 Obtaining the material properties

Three parameters are required for presenting the Viscoelastic material properties in the loss modules, the storage modules, and the Loss factor.

Viscoelastic materials' properties are time-dependent; viscoelastic materials are represented using a combination of linear elastic springs, for their elastic response and linear

dashpots, for the vicious part of the material. As shown in Figure 4-2, there is a relationship between the rubber's complex modulus and the frequency or time rate. As shown in Equation 4-1, the complex modulus has two parts. The real part is called the storage modulus, and the imaginary part is called the loss modulus. The result of the application of sinusoidal stress on a viscoelastic material is a sinusoidal strain. However, there is a phase difference between stress and strain that is called the loss factor ($\tan\delta$). Equation 4-2 shows that the loss factor is equal to the loss over storage modulus.

$$E^* = E' + iE'' \qquad 4\text{-}1$$

$$\tan\delta = \frac{E''}{E'} \qquad 4\text{-}2$$

where E' is the storage modulus, E'' is the loss modulus

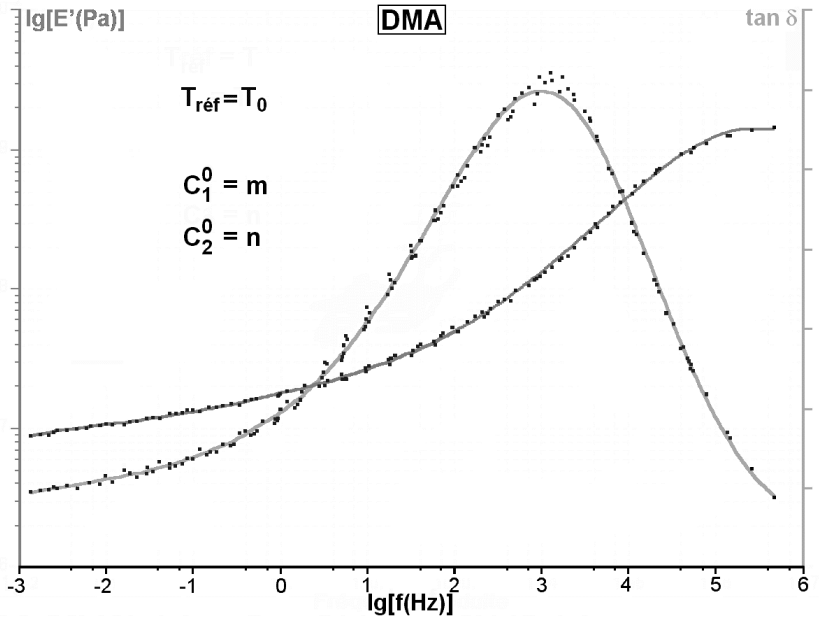

Figure 4-2: Master Curve on polymer [65]

Although models such as Kelvin-Voigt and Maxwell can obtain the storage modulus and loss modulus, those models cannot predict the material property accurately for a viscoelastic material like rubber. In this study, to have an accurate result for material properties, the experimental approach is used.

The data required for the material properties were provided by the company that sent the rubber samples for the sliding friction tests. To obtain the rubber's material properties as a viscoelastic material, the DMA test setup was used. The DMA machine has the limitation of collecting the data only for the frequency range of 0.1 HZ to 10HZ. To obtain the required data for a higher frequency, William_Landel_Ferry (WLF) approach is used to create the high-frequency master curve. As shown in Equation 4-3, the WLF approach illustrates a relation between the temperature and frequency and the modulus parameter.

$$E(w_{ref}, T) = E(a_T w_{ref}, T_{ref}) \quad 4\text{-}3$$

where T_{ref} is the reference temperature and w_{ref} is the reference frequency.

a_T is the WLF shift factor that can be obtained from Equation 4-4.

$$\log a_T = -\frac{C_1(T - T_{ref})}{C_2 + (T - T_{ref})} \quad 4\text{-}4$$

C_1, C_2 are the factors that can be obtained using an experimental approach.

Figure 4-3 illustrates WLF in different temperatures for SRI Compound A. Figure 4-4 shows the master curve obtained using the company's data and the modified results using the William_Landel_Ferry approach for Component A.

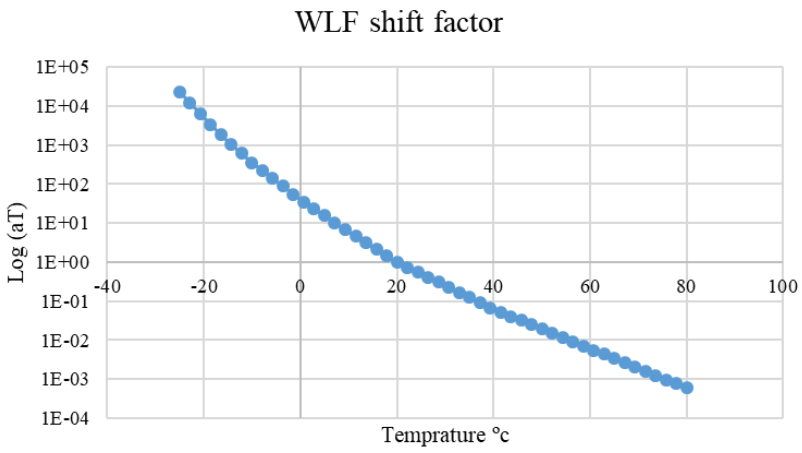

Figure 4-3: WLF shift factor for component A in different temperatures

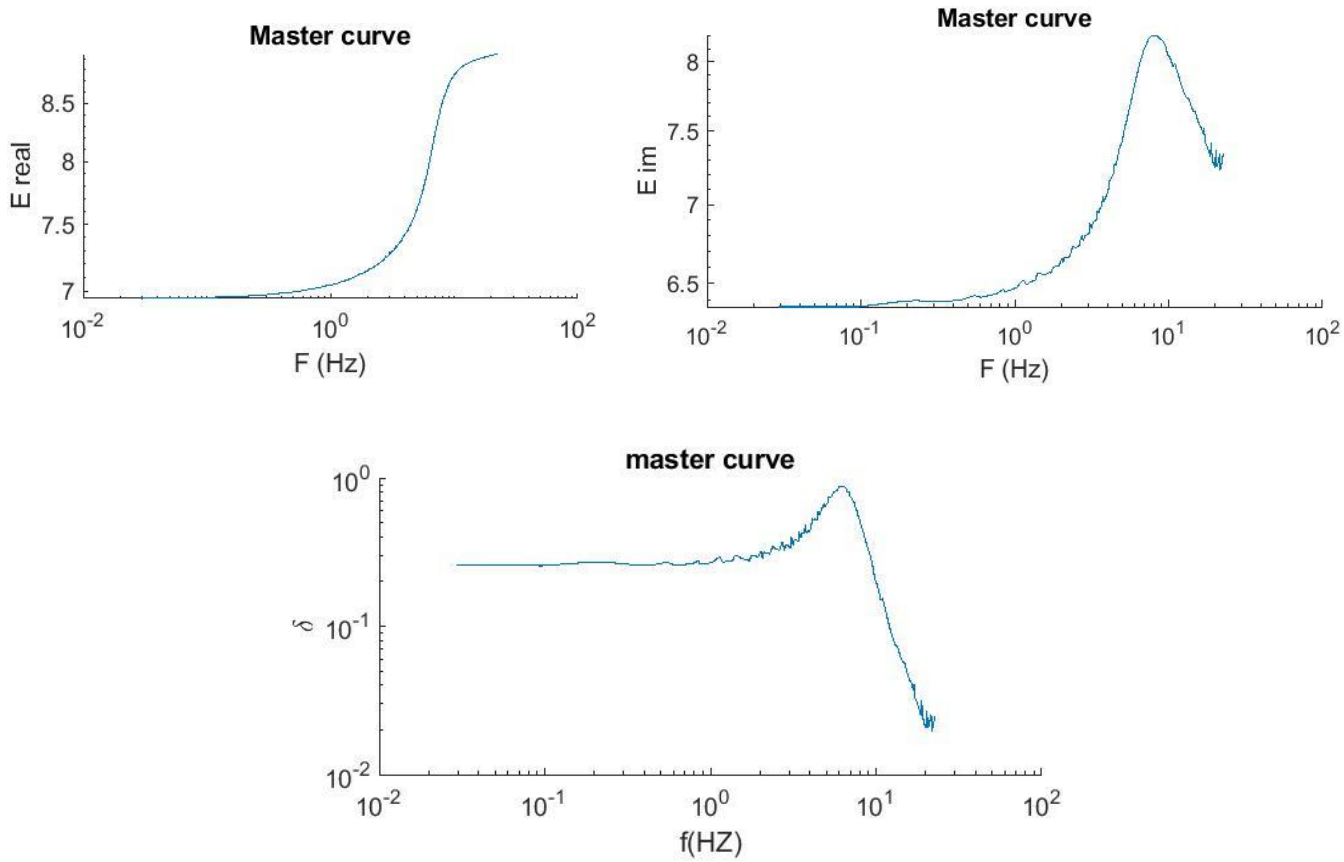

Figure 4-4: a) storage modules b) loss modulus c) Loss Factor in different frequencies for Component A by using the WLF approach.

4.2 Surface characteristics

The surface characteristics are the following parameters that are required for estimating the friction coefficient. For finding the characteristics of the surface, two approaches were used in this study: The experimental method by implementing a profilometer and the analytical method.

A profilometer is an apparatus to measure the profile of any type of surface. The measurement techniques can be classified based on the type of analysis: Contact and Non-contact methods. For measuring based on the contact methods, a stylus instrument is mainly used. In this type of instrument, the resolution, depending on the tip size, is between $20nm$ to $50\mu m$. For non-contact measuring, methods such as interferometry or holography, confocal microscopy, laser scanning that all are optical methods can be implemented. An area of profile can be obtained using the non-contact method. However, the contact method will only give the line profile of the surface.

A profilometer in the CenTiRe laboratory at Virginia Tech was used to collect the data related to the surface's characteristics. Figure 4-5 shows the profilometer used in this study.

The Non-Contact Profilometer Nanovea Jr25 was used to obtain the height profile of the surface. A maximum value of the surface area equal to 50×50 mm can be measured by the Profilometer. The resolution of this test setup is seven μm in both x and y directions. As shown in Figure 4-5, this profile will be used later to predict the surface characteristics. This apparatus's measurement method utilizes the raster scan concept and is based on Chromatic Confocal optical technology. It uses a series of lenses from the optical pen. White light is emitted with a high degree of chromatic aberration. A pinhole filter will reflect the light into the optical pen. Based on the calibration set, the light passes through a spectrometer. The wavelength corresponds to the distance chosen at that point.

Although the experimental approach can present the characteristics with high precision, this approach is time-consuming. One of this study's objectives is to perform a sensitivity analysis on the real contact area, friction coefficient, and wear rate concerning different surface characteristics such as the Hurst function and RMS of the surface. In order to perform this sensitivity analysis using an experimental approach, several profilometer measurements are required, and considering the quality of the test and the type of surface, it can take a long time. Thus, an experimental approach is not the best option for conducting sensitivity analysis. Therefore, the author programmed the MATLAB code for creating a randomly rough surface based on surface characteristics.

Figure 4-5: Non-Contact Profilometer Nanovea Jr25

Several characteristics of the surface are required in this study to obtain the wear rate: roughness (RMS), the power spectrum density (PSD), Root Mean Square (RMA), and the wave vector. To obtain these characteristics, the data collected by the profilometer need to be modified and changed

4.2.1 Analytical method to find surface characteristics

Considering the drawbacks of the experimental approach, to achieve one of this project's main goals, sensitivity analysis on tire wear and friction for different materials, an analytical approach is used to make a random rough surface. This model needs several parameters as inputs such as the RMS of the surface, Hurst function, length of topography, and cutting wave vector. The model

used in this study to predict the rough surface has several outputs, such as the power spectrum density of the surface and the wave vector. These parameters are used for predicting the friction coefficient.

Another important parameter for obtaining the friction coefficient is the surface characteristic in the Persson model, which is obtained by changing the magnification of the system contact between the rubber sample and road. It can be demonstrated that some parts of rubber and rough surfaces did not come in contact with each other, as illustrated in Figure 4-6.

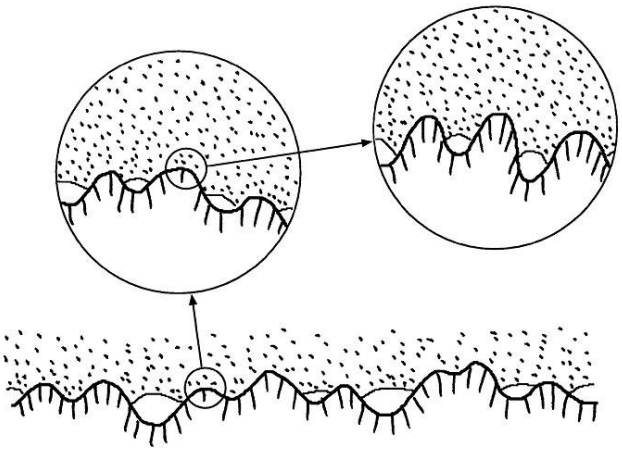

Figure 4-6: Rubber block in contact by rough surface in different magnification [20]

Roughness is an important parameter that has a vital role in the values of the surface's different characteristics, such as friction, adhesion, and (thermal and electrical) contact conductance. Several theoretical models were presented to estimate the surface topography's roughness value using PSD, which is the power spectral density of the surface topography. The PSD value is independent of the particular scan size and pixel resolution that the researcher will choose.

More details about the PSD can be found in [66]–[68].

Having the PSD values can help predict many of the functional properties of surfaces,

such as adhesion, contact stiffness, and the real contact area. These parameters have relevance to the friction coefficient [69]–[71] as well as the thermal [72] and electrical [73] conductance at the contact area, using several suggested theoretical models such as Persson's scaling theory for contact [74]–[76]. In some of these models, such as those introduced at [77], mathematical manipulations on PSD were used. The scalar quantity of the root-mean-square (RMS) height $h$rms was used as the input for this method. All three mentioned parameters can be calculated using the PSD. Considering that PSD plays an essential role in the input values of the suggested model for predicting the wear rate, calculating the PSD is one of the main challenges in this area. In the Persson model, the values of the PSD shown as C(q) can be obtained using Equation 4-5:

$$C(q) = \left(\frac{1}{2\pi}\right)^2 \int d^2x \langle h(x)h(0)\rangle e^{-iq.x} \qquad 4\text{-}5$$

For this study, sandpaper grit 120 made by 3M was used. Table 4-1 shows some surface properties for the mentioned sandpaper.

Table 4-1 Surface property for sandpaper grit 120

Surface Property	Sand Paper Grit 120
RMS height, $h0$ (m)	4.211 $e{-}5$
Fractal dimension, D	2.3
Small Wave vector, q_0 $(1/m)$	$10^{3.3}$

Figure 4-7 presents the results for the power spectrum density of the sandpaper grit 120 obtained by using the given data from the table as the inputs for the developed model. Figure 4-8 shows a sample result for 3D modeling of the random rough surface created using the programmed MATLAB code in this study for the sandpaper.

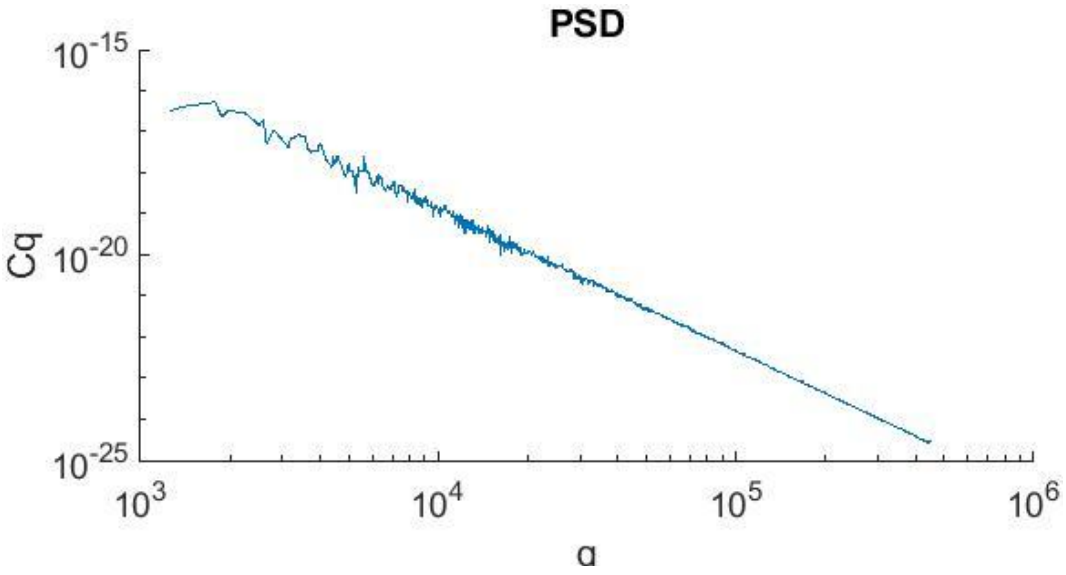

Figure 4-7: Power Spectrum Density of sandpaper

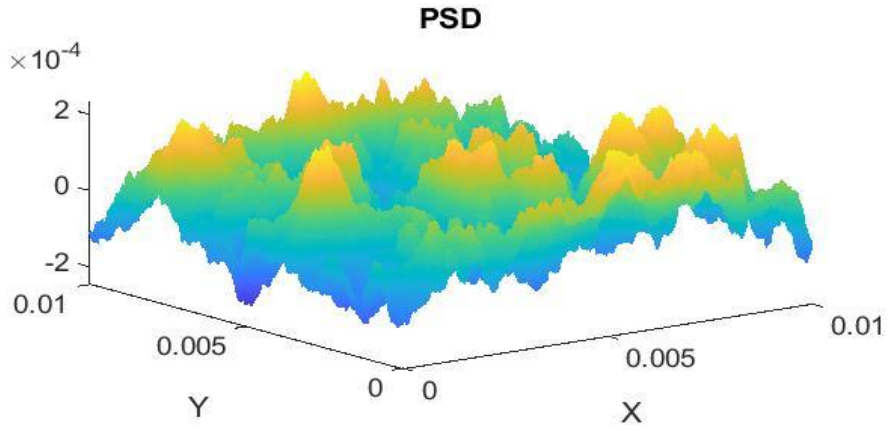

Figure 4-8: 3D random rough surface for sandpaper

4.3 Determining the real contact area

Persson was presented with one of the fundamentally different approaches for contact mechanics. This method starts from the opposite limit of a vast area of contact, which contrasts with the assumption for the multi-asperity contact theories, where the real area of contact is considered to be much smaller than the nominal area of contact.

In this theory, the theoretical predictions can be assumed to be exact when the squeezing force is so high that it will nearly complete contact in the area. When the force is small, the contact area projected on the XY-plane is proportional to the applied load. This results in the real contact area approaching the nominal contact area when the load increases. A diffusion-like equation was used in this theory in order to predict the stress distribution within the contact area. The characteristics of the interface in different magnification ζ were used to derive this equation.

To derive the equation, first, the surface assumes to be very smooth with almost no roughness when the magnification is low. For the next step, the magnification was increased successively so that more roughness components would be considered. The entire stress distribution can be observed by considering all length scales with the highest magnification. Using the stress distribution, the area of real contact can be obtained. This theory has several inputs: $C(q)$, which is the power spectrum of the surface roughness, E the elastic properties, and ϑ Poisson's ratio of the bodies in contact with each other.

The stress distribution for the magnification ξ in the contact area is shown as $P\ (\zeta, \sigma)$. Equation 4-6 can be obtained from this theory:

$$\frac{\partial P_d}{\partial \zeta} = f(\zeta)\frac{\partial^2 P_d}{\partial \sigma^2} \qquad 4\text{-}6$$

Where σ_0 is the nominal pressure and $f(\xi) = G'(\xi)\ {\sigma_0}^2$ where $G(\zeta)$ can be calculated by Equation 4-7

$$G(\xi) = \frac{\pi}{4}\left(\frac{E/(1-\vartheta^2}{\sigma_0}\right)^2 \int_{q_l}^{\zeta q_l} dq\, q^3\, C(q) \qquad 4\text{-}7$$

When time is replaced by magnification ζ, the diffusion-like term will convert to an equation with the stress σ as the spatial coordinate. $f(\zeta)$ is the "diffusion constant" and depends on ζ.

Figure 4-9 helps to understand the physical meaning of this equation. As shown in the figure, for the study on a system when the magnification ζ is low and close to 1, there will be no surface roughness that can be seen on the surface. Thus, the solid can have contact points everywhere within the nominal area of the contact. By assuming no friction in the contact area, the stress at the interface can be assumed to be equal everywhere to the applied stress σ_0, and then the stress distribution (Figure 4-9(a) right) will be a delta function $p(\sigma, 1) = \delta(\sigma - \sigma_0)$.

By increasing the magnification, the roughness with wavelength $\lambda = L/\zeta$ is added to the contact problem that causes emerging regions with no contact within the contact area. At the edges of the boundary between the non-contact and contact regions, the stress must be equal to zero continuously, similar to the theory presented by Hertz.

These results in the change in stress distribution P (ζ, σ), as indicated in Figure 4-9 (b). The stress distribution is more similar to a diffusion problem by increasing magnification, as shown in Figure 4-9 (c).

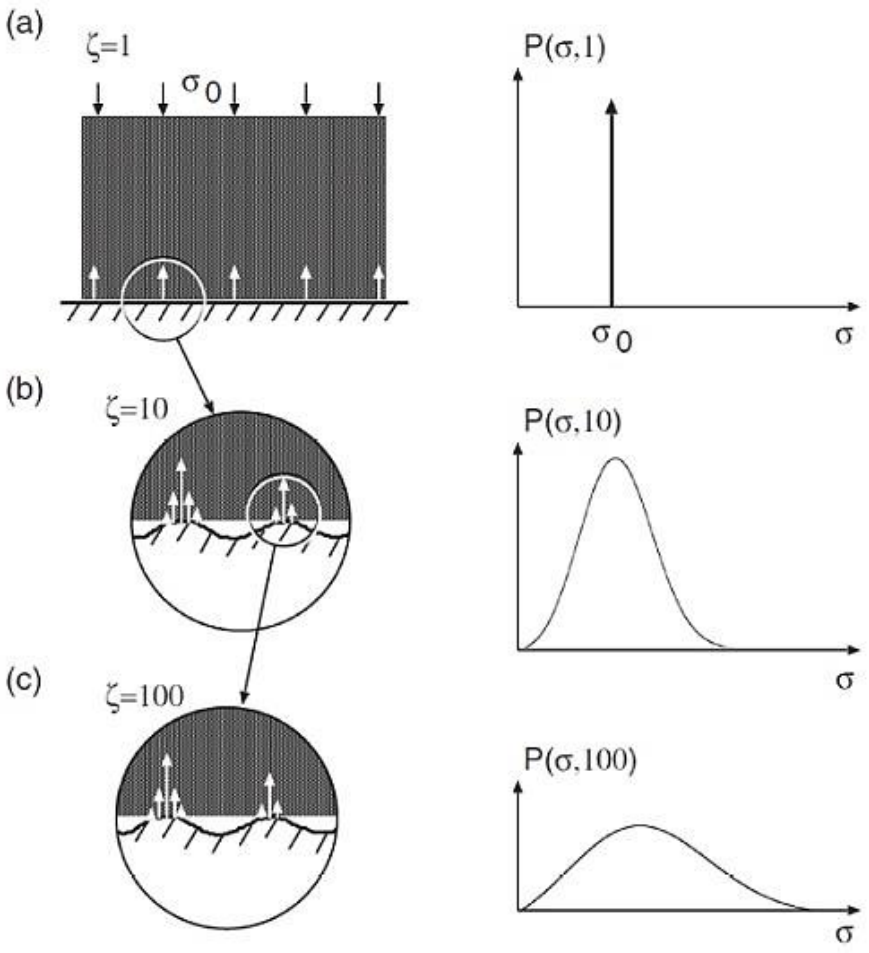

Figure 4-9: The stress distribution in the contact area in different magnification [20]

Equation 4-8 shows the stress distribution $P\ (\zeta, \sigma)$ at the interface. Where $\zeta = L/\lambda$ is the magnification and λ is the shortest surface roughness wavelength for magnification ζ

$$p(\sigma,\xi) = \frac{1}{A_0}\int d^2x\ \delta(\sigma - \sigma(x,\xi)) \qquad 4\text{-}8$$

For the surface roughness components with wave vector $q < \zeta * q_L$, $\sigma(x,\zeta)$ is the stress at the interface. In the equation, the integral is performed over the contact area A. By integrating over A_0, the function for stress probability will have a delta function $[(A_0 - A)/A_0]\delta(\sigma)$. However, this is not considered in this approach.

The area of real contact can be obtained directly from the stress distribution:

$$P(\xi) = \frac{1}{A_0}\int d\sigma\, P(\sigma,\xi) \qquad 4\text{-}9$$

the area of (apparent) contact when only partial contact occurs can be written as

$$P(\xi) = \frac{A(\zeta)}{A_0} = \frac{1}{\sqrt{\pi}}\int_0^{\sqrt{G}} dx e^{-x^2/4} = \text{erf}\left(\frac{\sqrt{G}}{2}\right) \qquad 4\text{-}10$$

$G(\zeta)$ is given by Equation 4-7. The area of contact can be obtained using this equation for the desired magnification. The actual contact area can also be predicted at an atomic resolution if the power spectrum is measured.

4.3.1 Effect of road characteristic and velocity in the real contact area

As shown in Figure 4-1 for the friction coefficient prediction process, after obtaining the material properties and modeling the surface, the next step is finding the real contact area.

Persson model was used for the prediction of the real contact area. In this model, a complete contact between rubber and substrate surface was assumed for the magnification's low values. However, when the magnification increases, more asperities will be detected; thus, the contact area's value will change.

Figure 4-10 presents the effect of the rough surface's different parameters, such as root mean square h_0 and Hurst exponent surface H, on the real contact area for different magnifications' values. As shown in this figure, by increasing the RMS of the surface that corresponds to the asperities with more height, the real contact area decreases. The figure

shows that by increasing the Hurst function, which means having a smoother surface, the real contact area for low magnification values does not significantly change. However, when the magnification value increases to over 8, the real contact area increases gradually.

Figure 4-11 shows the real contact area as a function of velocity by using the Persson model for different magnification values. The area ratio results show a decreasing trend by increasing the rubber block's sliding velocity when in contact with sandpaper surfaces.

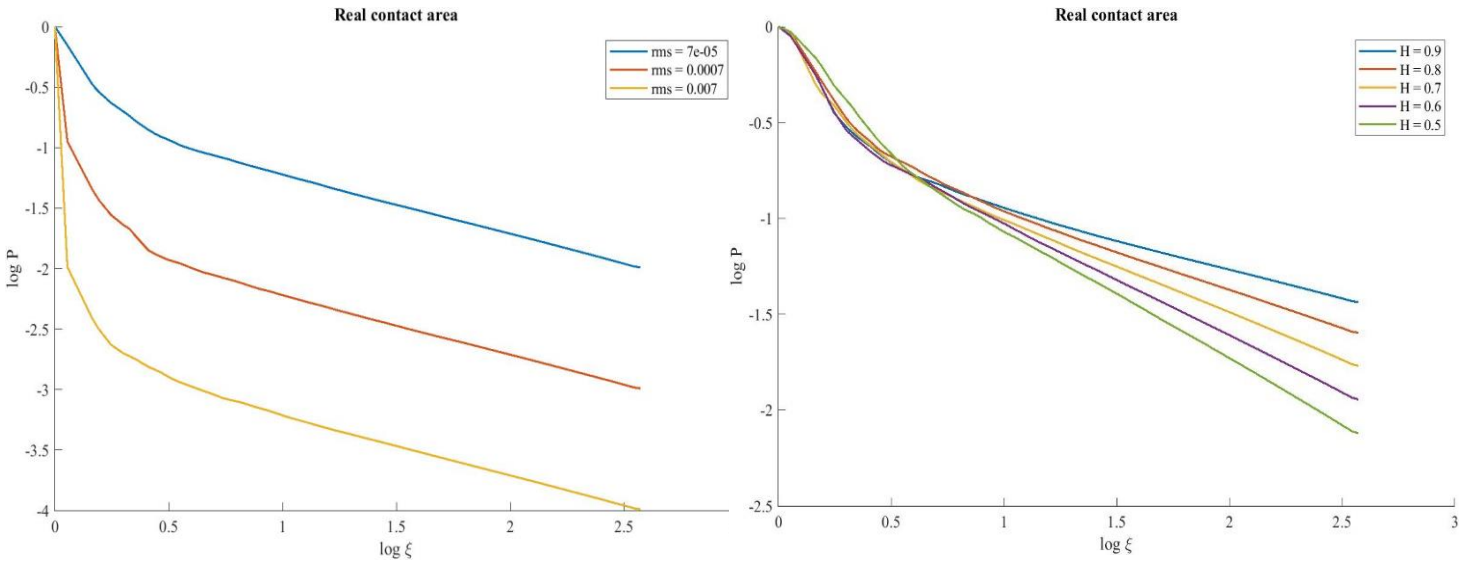

Figure 4-10: Effect of Hurst function and RMS of the surface in real contact area

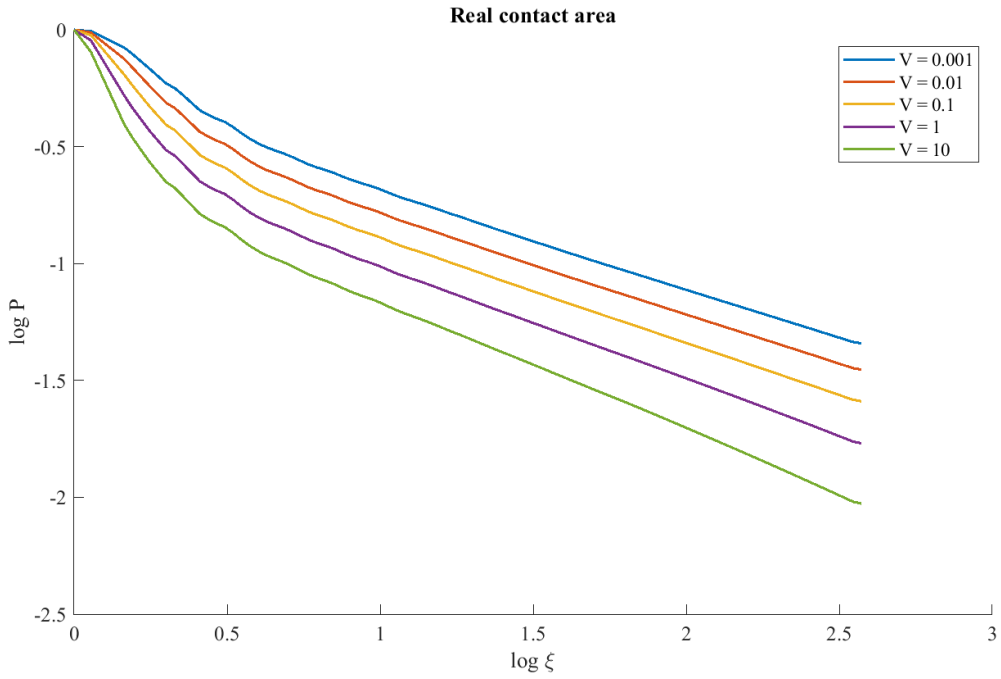

Figure 4-11: Effect of sliding velocity in different magnification on real contact area

4.4 Friction

To achieve the primary goal of this study, which predicts the wear rate of the rubber in contact with a rough surface, the first step is finding the friction coefficient. This study implements the Persson model to obtain the friction coefficient between the rubber sample and the rough surface. A brief description of the model is included in the literature review section. As shown in the figure, the friction coefficient's value in the Persson model is related to the materials' thermal properties, the real contact area, and the surface characteristics. Thus, to predict the friction coefficient, it is needed to find the mechanical and thermal properties of the materials and surface characteristics first.

The Persson model can obtain the friction coefficient by having the real contact area, material properties, and surface characteristics. Persson's friction model for a dry surface depends on two primary mechanisms: Hysteresis and Adhesion. In the Hysteresis mechanism, the internal damping due to the undulation in the surface causes Energy dissipation. Hysteresis is highly dependent on time-dependent material properties. For the rough surface at high speed, this mechanism governs the friction mechanism. Adhesion mechanism happens because of the intermolecular connection or Vander Waals attraction at the contact area. This mechanism is dominant for smooth surfaces, high loads, and low velocities. Thus, this type of friction will vanish in the presence of lubricants or contaminants or on the surface.

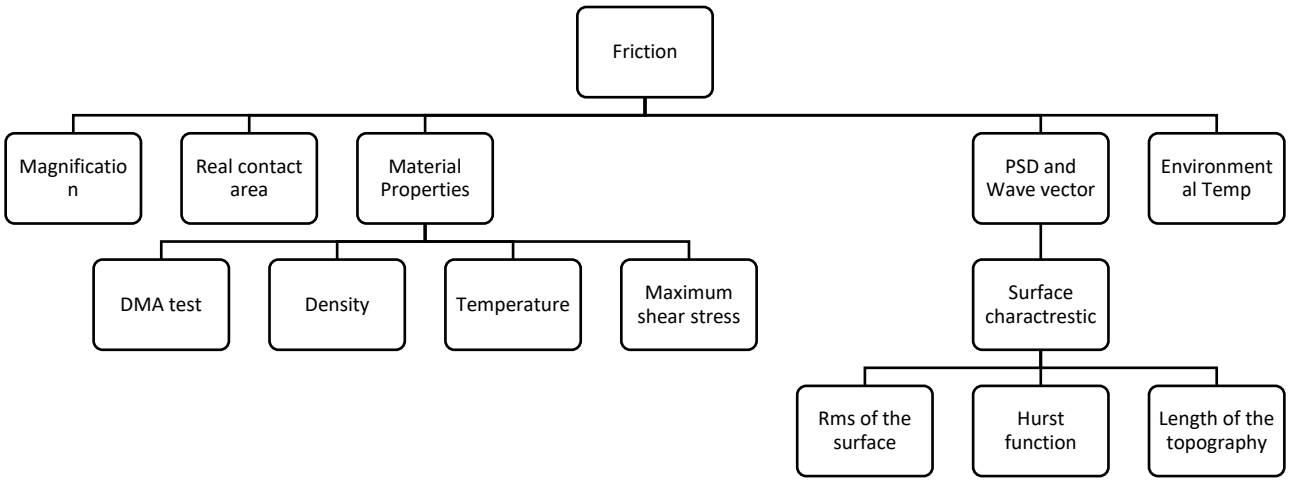

Figure 4-12: Inputs and approaches for obtaining friction

4.4.1 Hysteresis

In order to predict the hysteresis friction, Persson assumed that the energy dissipated due to the friction force is equal to internal energy loss in viscoelastic materials, as shown in the equation.

The energy dissipated due to the friction force during the time t_0 can be calculated by Equation 4-11

$$\Delta E = \sigma_f A_0 v t_0 \qquad 4\text{-}11$$

Where σ_f is frictional shear stress and A_0 is surface area. Also, internal energy can be written as equation 4-12

$$\Delta E_H = \int d^2x dt \, \dot{u}.\sigma = (2\pi)^3 \iiint_{-\infty}^{+\infty} (-i\omega)\sigma(-\vec{q},-\omega)u(\vec{q},\omega)\, d^2q d\omega \qquad 4\text{-}12$$

Now by considering changing the variables and also using PSD, Equation 4-13 is derived :

$$\sigma_f = \frac{1}{2}\iint_{q_0}^{q_1} q^2 \cos\varphi \, C(q) Im\left\{\frac{E(vq\cos\varphi)}{(1-\vartheta^2)}\right\} d^2q \qquad 4\text{-}13$$

Now by finding the ratio of the frictional shear stress overpressure σ_0, the coefficient of friction for hysteresis can be obtained as Equation 4-14:

$$\mu_H = \frac{1}{2}\iint_{q_0}^{q_1} q^2 \cos\varphi \, P(q) C(q) Im\left\{\frac{E(vq\cos\varphi)}{(1-\vartheta^2)\,\sigma_0}\right\} d^2q \qquad 4\text{-}14$$

Where $C(q)$ is power spectrum density and $p(q)$ is the real contact area in length scale $\lambda = \frac{2\pi}{q}$ that we chose for this study.

Since $C(q)$ and $p(q)$ are just functions of q, then Equation 4-15 can be written as

$$\mu_H(v) = \frac{1}{2}\int_{q_0}^{q_1} q^3 P(q) C(q) \left\{\int_0^{2\pi} \cos\varphi \, Im\left\{\frac{E(vq\cos\varphi)}{(1-\vartheta^2)\,\sigma_0}\right\} d\varphi\right\} dq \qquad 4\text{-}15$$

4.4.2 Adhesion

The adhesive part of friction is developed due to the interaction between the molecules of

two surfaces. The adhesive part of the friction will reduce for higher speeds by increasing the rubber movement's speed or using lubricant. We have a reduction in adhesive for very low sliding velocities of the rubber due to breaking the interfacial bonds caused by thermal fluctuations. Thus, the maximum value of the friction coefficient must happen at intermediate velocities.

Persson used an empirical model developed by B. Lorenz [20], [78] to find the friction's adhesion part. In this model, the friction coefficient for the adhesive mechanism is a function of the sliding velocity and real contact area:

$$\mu_{Ad}(v) = \frac{\tau_f}{\sigma_0} P(v, \zeta, T) \qquad 4\text{-}16$$

Where τ_f is defined in Equation 4-17, and P is the real contact area on specific magnification.

$$\tau_f = \tau_{f0} \exp\left(-c_0 \left[\log\left(\frac{v}{v_{\mathrm{m0}}}\right)\right]^2\right) \qquad 4\text{-}17$$

Where τ_{f0} is the maximum shear stress in a range of 5.3MPa-8.3MPa and for rubber material $v_{\mathrm{m0}} \approx 6\frac{m}{s}$ and $c_0 = 0.1$

The frictional shear stress that is obtained from the above equation is for the reference temperature $T_{ref} = 20℃$ so by using the Arrhenius shift factor, shear stress for other temperatures can be obtained by using

$$\tau_f(v, T) = \tau_f(a_T{}'T) \qquad 4\text{-}18$$

Where $a_T{}'$ can be defined by using equation

$$\ln a_T{}' = C_1'(\frac{1}{T} - \frac{1}{T_g} + C_2') \quad \text{4-19}$$

where $C_1' = 1.1e4$ and $C_2' = 8.4e - 4$ and T_g is glass transition temperatures.

In this study, the same model was used to find the adhesive part of the friction coefficient.

According to the Persson model, the friction coefficient can be obtained using Equation 4-20:

$$\mu_{Total} = \mu_H + \mu_{Ad} + \mu_C \quad \text{4-20}$$
$$= \frac{1}{2}\int_{q_0}^{q_1} q^3 P(q) C(q) \left\{ \int_0^{2\pi} \cos\varphi \, Im\left\{ \frac{E(vq\cos\varphi)}{(1-\vartheta^2)\,\sigma_0} \right\} d\varphi \right\} dq$$
$$+ \frac{\tau_{f0}}{\sigma_0} P(q_1) \exp\left(-c_0 \left[\log\left(\frac{v}{v_0} \right) \right]^2 \right)$$

Where μ_H is hysteresis friction coefficient and μ_{Ad} is adhesive friction coefficient and μ_c is calculated from the interaction between the train and the filler particles and within the order 0.1.

Figure 4-13 shows results obtained by the developed analytical model. The figure illustrates the values of friction coefficient versus velocity for different Hurst functions of the surface. As can be seen from the graph for all Hurst function cases, the friction coefficient increases for lower velocities, and after reaching the maximum values, it will decrease by increasing the velocity. For the Hurst function's different values, for lower velocity, by increasing the Hurst function, which means smoothing the surface, the adhesion component of friction coefficient is dominated over the hysteresis term. On the other hand, hysteresis friction is dominant for higher velocities, and the maximum friction occurs at higher slip velocities. The main reason for this phenomenon is that the more effective friction

mechanism is adhesive for lower speed. When speed is lower, and the surface is smoother, the adhesion between the surface and rubber increases. This will result in increasing the real contact area. However, the hysteresis mechanism is the governing mechanism in the friction coefficient's value by increasing the velocity.

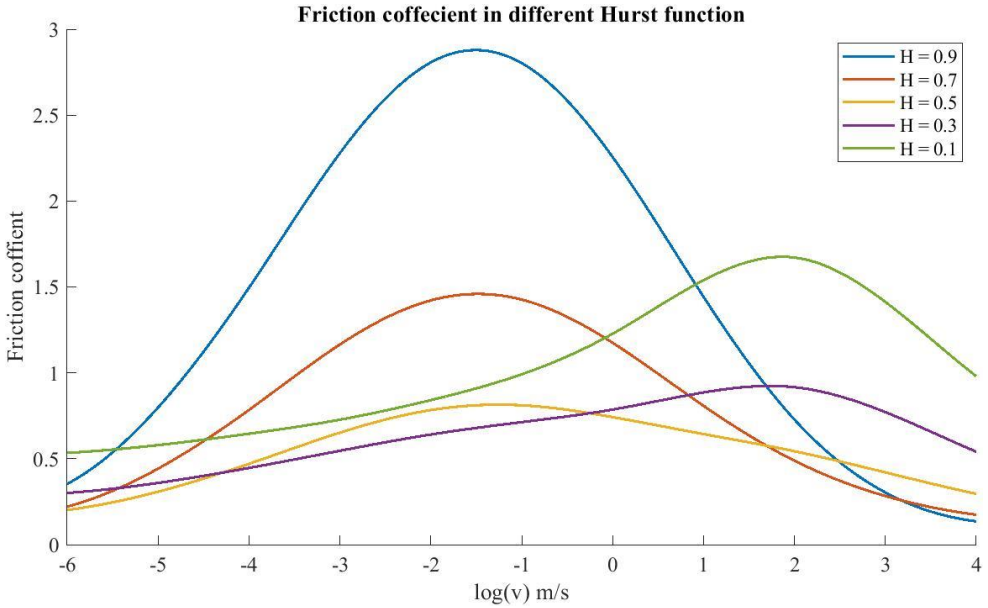

Figure 4-13: Changing the friction coefficient in different Hurst function

Figure 4-14 shows the friction coefficients' values with respect to velocity for different RMS of the surface. The graph shows that the friction coefficient has a similar trend to the Hurst function graph for different velocities. However, when the RMS of the surface increases for the lower velocities, the friction coefficient values decrease. On the other hand, an opposite trend can be observed for higher velocity. The main reason for this phenomenon is that by increasing the RMS function, the height of the asperities increases, and this results in reducing the real contact area, and consequently, the friction coefficient; because as mentioned, the adhesive mechanism is the governing mechanism in the friction values when the speed is low.

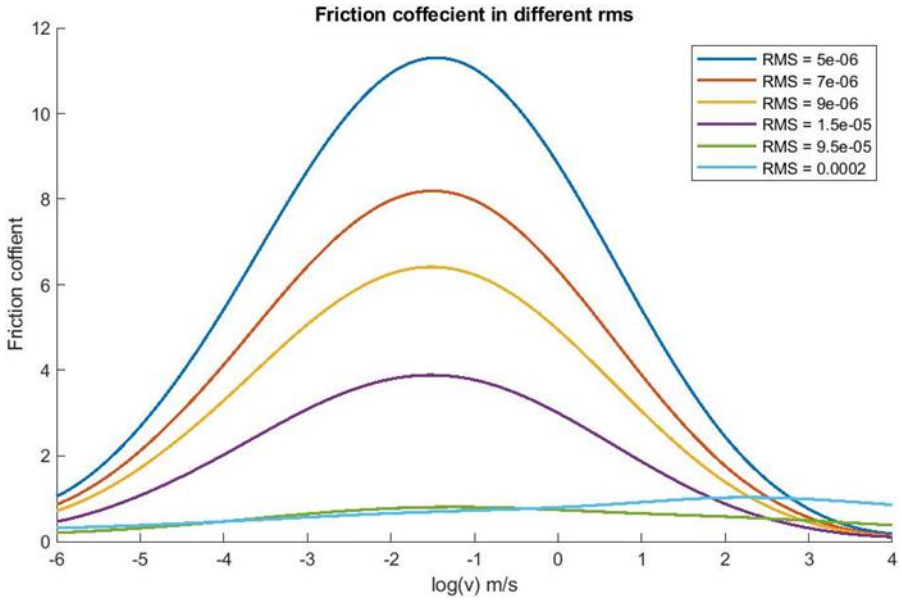

Figure 4-14: Changing the friction coefficient in different RMS

In order to validate the model, the friction coefficient for rubber sample component A in contact with sandpaper grit 120, with RMS value and Hurst function given in Table 4-1, is obtained using the developed model and experimental approach. The approach to conduct the required tests was presented in section 3.2.7. As can be seen from the graph, the friction coefficient values coincide with the experiment's data. In this graph, the dotted line presents the adhesive friction values for different velocities obtained by the developed model. As can be seen, for low velocities, the adhesive friction coefficient increases by increasing the velocity until reaching the peak value. After passing the peak value, the adhesive friction coefficient decreases by increasing the velocity. The graph shows that the hysteresis friction coefficient increases when the velocity increases for higher velocities for the hysteresis mechanism. The blue line shows the total friction coefficient, which is the sum of the hysteresis and adhesive friction values.

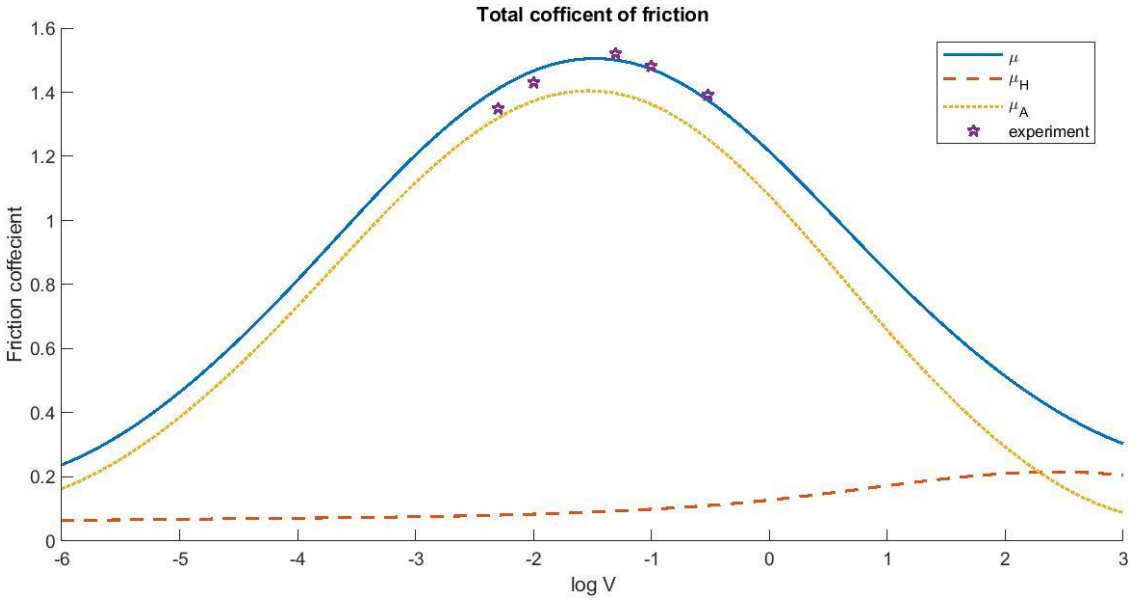

Figure 4-15: Friction coefficient obtained from experiment and analytical model

4.5 Wear rate

After finding the friction coefficient, the next objective is the prediction of the wear rate values. As shown in Figure 4-1, the wear rate value is closely associated with the real contact area and friction between two surfaces in contact. The powdery rubber theory is one of the models that can be used to predict the wear rate. However, the results of this theory show a considerable amount of errors. The theory of powdery rubber was explained in the literature review section.

Volume losing of two bodies that are in contact with each other is called wear. The material's wear rate is expressed as losing weight or volume of sample per unit of sliding distance. Wear as a complex process can be classified into five categories depending on the mechanism that caused the body's material removal: Adhesive, Abrasive, Fatigue, Corrosive, and Erosive. Here, a brief description of each is presented:

• Adhesive: This wear mechanism is a mechanical wear process. It depends on the surface asperities and rubber interaction. The transient adhesion of asperities causes material removal of the body. This is shown in Figure 4-16(A).

• Abrasive – This wear mechanism is a scratching process or micro-cutting process that is similar to the adhesive wear mechanism. However, abrasive wear happens for the surface with sharp projections or when the applied normal load causes an increase in the contact stresses until reaching the rubber tearing strength. Figure 4-16(B)

• Fatigue – repeated elastic deformations of material like rubber can cause fatigue wear. This mechanism happens due to the cyclic deformations caused by smooth surfaces or blunt projections or when the rubber shows elastic deformations. The crack's initiation and propagation cause the wear rate in the range of very slow to moderate. Figure 4-16(C)

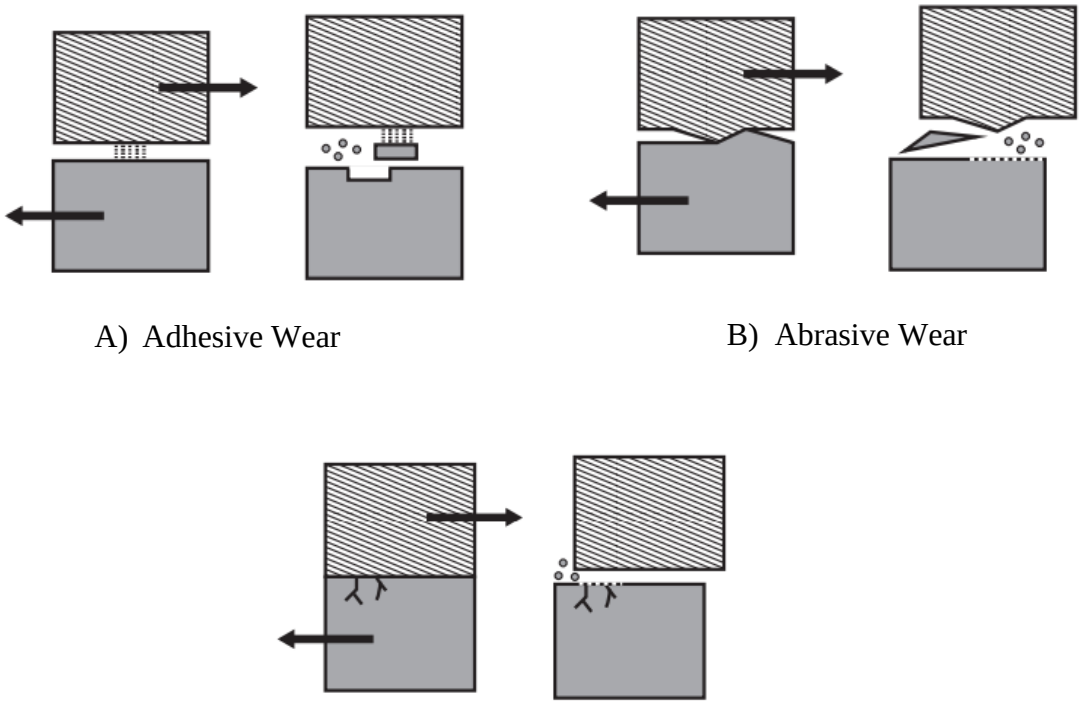

Figure 4-16: wear types

• Corrosive – This mechanism of wear is part of the aging process and happens mainly due to chemical degradation. When the polymer chains are breaking or when the high temperature at the contact area causes oxidation of the rubber material, this wear mechanism will happen.

• Erosive –This mechanism happens for concise sliding motion with short time intervals.

Several experimental and numerical studies suggested methods to predict the wear rate. However, the only acceptable analytical model that can present the results with acceptable errors in the model was presented by Persson. Persson developed a physics-based model for calculating fatigue wear, called the Theory of powdery rubber wear. Comparing the result obtained by the theory of powdery wear and the experimental data collected for the wear rate

shows there is still some error between the experimental data and analytical results. A novel approach is used in this study to improve the Persson model and to reduce the error. In this approach, the theory of powdery rubber wear is connected to crack propagation theory, as has been shown in the figure. In sections 4.6 and 4.7, the details of the crack propagation theory and theory of powdery rubber wear will be explained, and also the approach to connect these theories is presented.

4.6 Crack propagation theory

Crack propagation is one of the critical parts of the wear mechanism. Persson developed a model based on Crack propagation in rubber-like materials. He defined parameter G as strain energy release in his study, which is devoted to the required energy to propagate a crack plane per one-unit area. As shown in Equation 4-21, the strain energy released depends on the crack tip velocity and temperature.

$$G(v,T) = G_0{}^{*} g(v_c,T)[1 + f(v_c,T)] \qquad 4\text{-}21$$

Where G_0 is threshold values below which no fracture occurs and f → 0 as v → 0.

The energy loss method was used to generate the presented results in this section.

Gv_c which are the demands for energy conservation is equal to $G_0 v_c$ that is the fracture energy plus P that is the bulk viscoelastic dissipation:

$$Gv_c = G_0 v_c + P \qquad 4\text{-}22$$

A linear viscoelastic solid is also a homogeneous material. The energy dissipation per unit length and unit time of the crack can be written as Equation 4-23:

$$P(\vec{x},t) = \iint \sigma_{ij}\dot{\epsilon}_{ij} d^2x \qquad 4\text{-}23$$

The theory that Persson developed shows that

$$1 + f(v_c, T) = a(v,T)/a_0 \qquad 4\text{-}24$$

Where $a(v,T)$ is devoted to the crack-tip radius, with the crack velocity propagation of v.

For a crack with a shallow propagating velocity, a0 is the crack-tip radius. The function $a(v,T)/a_0$ can be found by Equation 4-25:

$$\frac{a(v_c)}{a_0} = \left(1 - E_0 \frac{2}{\pi} \int_0^{2\pi v/a} \frac{F(\omega)}{\omega} Im\ \frac{1}{E(\omega)} d\omega\right)^{-1} \qquad 4\text{-}25$$

Which also can be written as

$$\frac{a(v_c)}{a_0} = \left(1 - k \frac{\int_0^{2\pi v/a} \frac{F(\omega)}{\omega} Im\ \frac{1}{E(\omega)} d\omega}{\int_0^{\infty} \frac{1}{\omega} Im\ \frac{1}{E(\omega)} d\omega}\right)^{-1} \qquad 4\text{-}26$$

Where $k = 1 - \frac{E_0}{E_\infty}$ and $F(\omega) = [1 - \left(\frac{\omega a}{2\pi v}\right)^2]^{1/2}$

By using the change of variable $x = \frac{a\omega}{2\pi v} \rightarrow d\omega = \frac{2\pi v}{a} dx$ and defining $\omega_c = \frac{2\pi v}{a}$ Equation 4-27 can be written in the following form.

$$\frac{a(v_c)}{a_0} = \left(1 - E_0 \frac{2}{\pi} \boldsymbol{\alpha} \int_0^1 \frac{\sqrt{1-x^2}}{x} Im \frac{1}{E(x\omega_c)} dx\right)^{-1} \quad 4\text{-}27$$

And by using Equation 4-21, Equation 4-24, and Equation 4-27, we can illustrate the relationship between Crack tip velocity and energy dissipation in Equation 4-28

$$\frac{a(v_c)}{a_0} = \frac{G}{G_0} = \left(1 - E_0 \frac{2}{\pi} \boldsymbol{\alpha} \int_0^1 \frac{\sqrt{1-x^2}}{x} Im \frac{1}{E(x\omega_c)} dx\right)^{-1} \quad 4\text{-}28$$

The stress intensity factor under mode I and II loading are related to strain energy release rate and modulus as:

$$K^2 = G\overline{E} \quad 4\text{-}29$$

Where $\overline{E} = E_0$ for plane stress condition and E_0 is $E_0 = \frac{E_\infty}{1+E_\infty \frac{2}{\pi}\int_0^\infty \frac{1}{\omega} Im \frac{1}{E(\omega)} d\omega}$. Also, Persson calculated the α by dividing the area of crack into three areas (glassy region, transient region, and rubbery region) and found it equal to one. One can write Equation 4-30 that is the implicit function of v_c.

$$\frac{G(v_c)}{G_0} = \frac{a(v_c)}{a_0} = \left(1 - \frac{E_\infty \frac{2}{\pi} \int_0^{\omega_a} \frac{\sqrt{1-\left(\frac{\omega}{\omega_a}\right)^2}}{\omega} Im \frac{1}{E(a_T\omega)} d\omega}{1 + E_\infty \frac{2}{\pi} \int_0^\infty \frac{1}{\omega} Im \frac{1}{E(a_T\omega)} d\omega}\right)^{-1} \quad 4\text{-}30$$

4.7 Theory of powdery rubber wear

Persson shows that the wear process involves two significant steps. The first step is called nucleation of crack-like defects, followed by the second step, which is the propagation of the cracks. Thus, the wear rates depend on two parameters: the number of cracks nucleating and the cracks' rate propagating on the contact surface. To estimate the wear rate, it is needed to find the crack sizes probability distribution that can be found using Equation 4-31:

$$\Psi(D,t) = \langle \delta(D - c(t)) \rangle \qquad 4\text{-}31$$

D is the length of crack sizes, t is the time, and c(t) is the crack length located into the surface's bulk material. ⟨…⟩ refers to the averaging for all the cracks. The cracks could turn around if intense stress is applied at the crack tip, as shown in Figure 4-17.

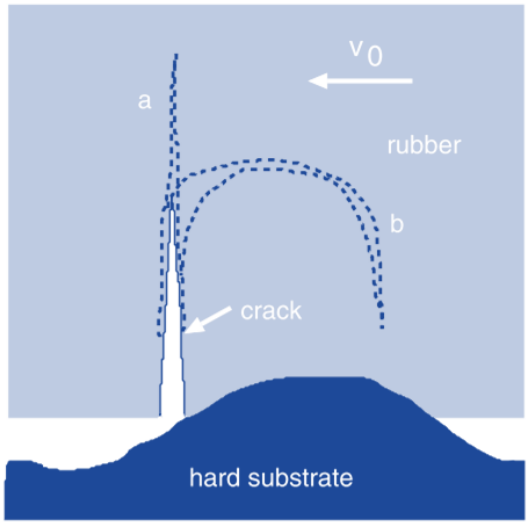

Figure 4-17: Crack propagation [41]

In this theory, there are N0 cracks on a rubber block with a nominally flat surface area A0, the volume of removed rubber per unit time becomes:

$$\frac{dV}{dt} = N_0 \int_{D_1}^{\infty} \left(\frac{\pi D^3}{6}\right)\left(\frac{v_c(D)}{l}\Psi(D)\right) \mathrm{d}D \qquad 4\text{-}32$$

where $N_0 \approx \xi \frac{A_0}{D_1^2}$ and D_1 is the effective diameter of the smallest wear particle that can be detected, and the average volume is $\frac{\pi D^3}{6}$ and volume removal rate is $\frac{v_c(D)\Psi(D)}{l}$ .Then, the volume loss per sliding distance (the wear rate) can be written by Equation 4-33 :

$$\frac{dV}{dL\, A_0} = \frac{\pi \xi l^3}{D_1^2 v} \langle \int_{D1}^{D\infty} \frac{e^{-\frac{D-D_1}{l}}}{v_c\zeta(D)P(\zeta)} dD \rangle^{-1} \qquad 4\text{-}33$$

Where v is the sliding velocity, $vc(D)$ is the average crack tip velocity over the contact area observed at the magnification ζ, and ⟨…⟩ refers to the average over the tire tread blocks in the footprint, and also average over the time. It is essential to know that P (ζ) and υ(D) depend on the location of the tread block within the contact area and

$$P(\zeta) = \frac{A(\zeta)}{A_0} \qquad 4\text{-}34$$

Equation 4-34 shows the relation between A0 (the nominal contact area) and (ζ) (rubber-substrate contact area at magnification ζ).

D1 is a short-distance cut-off length, and D is the crack length at magnification ζ that can be written by Equation 4-35:

$$D \approx \frac{1}{q} = \frac{1}{\zeta q_0} \qquad 4\text{-}35$$

Where q is the wave vector.

4.7.1 Improvement in the theory of powdery rubber wear

In order to improve the theory of powdery wear, a novel approach is used in this study. In this approach, the theory of powdery rubber wear is connected to the theory of crack propagation.

From the theory of powdery rubber, the wear rate is a function of crack tip velocity:

$$\frac{dV}{dL\,A_0} = \frac{\pi\xi l^3}{D_1^2 v}\left(\int_{D1}^{D_\infty} \frac{e^{-\frac{D-D_1}{l}}}{v_c(D)P(\zeta)}dD\right)^{-1} \qquad 4\text{-}36$$

Using this theory, one can predict the energy dissipation of the crack:

$$G(\zeta) \approx \frac{(\mu\sigma_0)^2}{2q_0\zeta\, P(\zeta)^2|E(vq_0\zeta)|} \qquad 4\text{-}37$$

On the other hand, in the theory of crack propagation, the energy dissipation is a function of crack tip velocity:

$$G(v_c) = G_0\left(1 - \frac{E_\infty \frac{2}{\pi}\int_0^{\frac{2\pi v_c}{a(v_c)}} \frac{\sqrt{1-\left(\frac{\omega}{\frac{2\pi v_c}{a(v_c)}}\right)^2}}{\omega} Im\ \frac{1}{E(a_T\omega)}d\omega}{1 + E_\infty \frac{2}{\pi}\int_0^\infty \frac{1}{\omega} Im\ \frac{1}{E(a_T\omega)}d\omega}\right)^{-1} \qquad 4\text{-}38$$

Considering Equation 4-36 through Equation 4-38, there is a way to connect these two theories. The figure shows the flowchart that presents how these two models are combined.

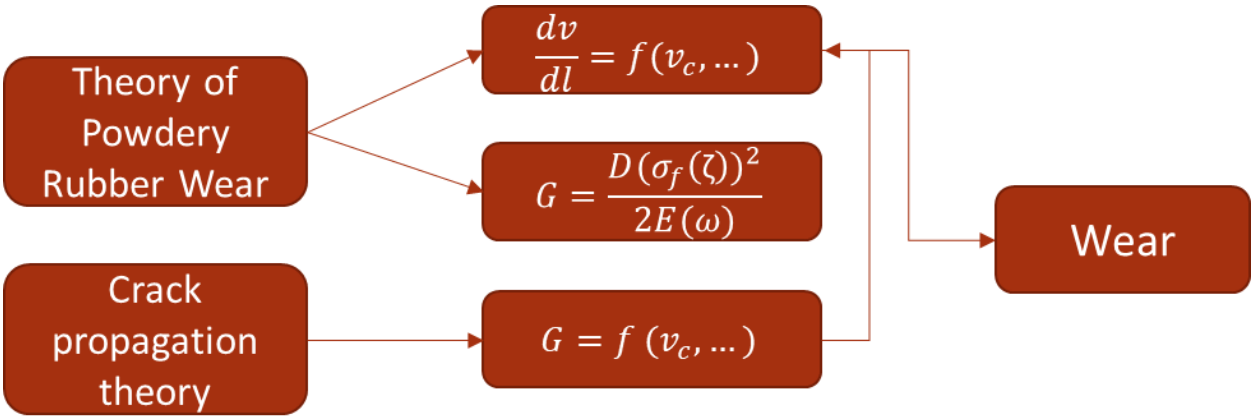

Figure 4-18: The procedure of combining the theory of powdery rubber wear and crack propagation theory

These two theories are connected by making an iteration to use the energy dissipation value obtained by the theory of powdery as an initial energy dissipation value. Then, using the crack propagation theory and having the initial value of the energy dissipation, the velocity of the crack can be calculated using the equation. When the crack propagation theory's velocity is predicted, it will be used in the theory of powdery to obtain the wear rate using Equation 4-36.

4.7.2 Result

As shown in Figure 4-19, the amount of error between the results obtained by the theory of powdery rubbery wear and results obtained experimentally is considerable. In this study, to improve the results from the theory of powdery rubber for obtaining the rubber sample's wear rate on the rough surface, the theory of powdery rubber is improved. The improvement

is obtained by connecting this model to the theory of crack propagation. MATLAB is used for programming the new model. The results of the improved model will be presented in this section.

Figure 4-19 compares the results obtained for the rubber sample's wear rate in contact with the sandpaper grit 120, using the developed model and the experimental approach. It can be seen from the simulation that there was an increase in the values of the wear rate when the speed increased. By comparing the results obtained via a new approach implemented for the modeling in this study and the results obtained by the previous study in this area, an improvement in the amount of error between the results obtained by modeling and data collected by the experiment can be observed.

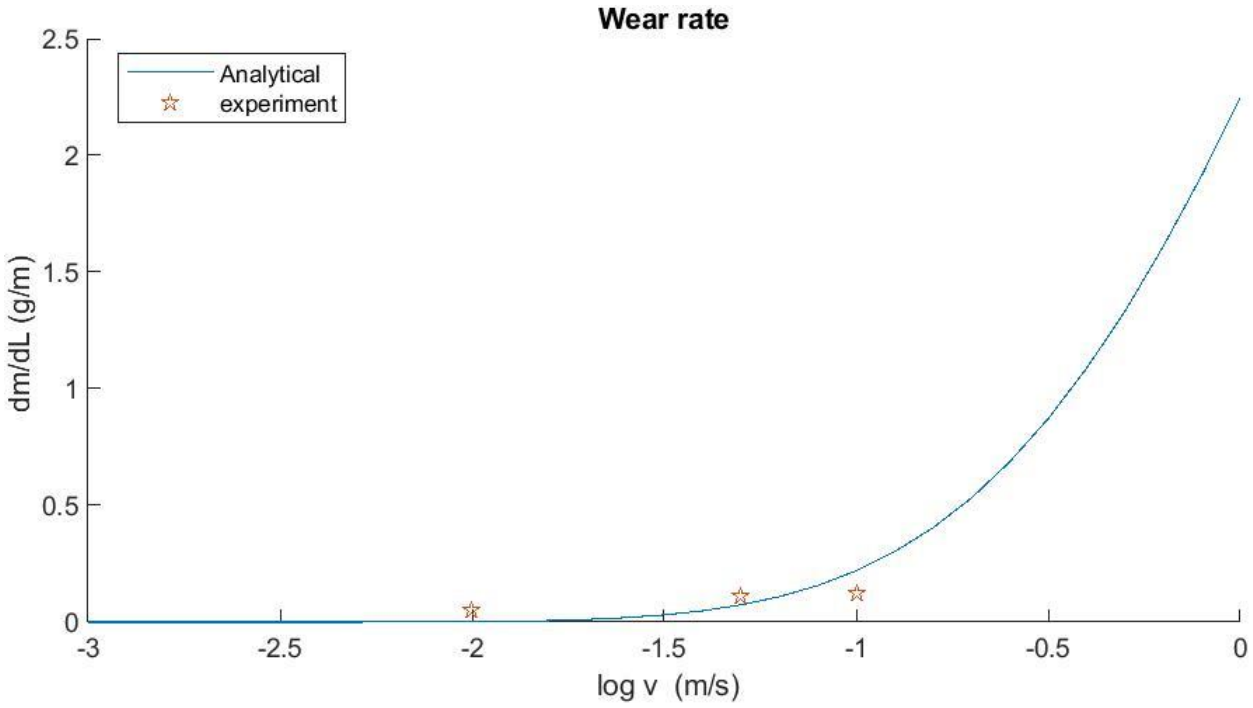

Figure 4-19: Comparison of wear rate result with experimental data

Chapter 5

Numerical Model

When two surfaces come in contact, the friction between these surfaces gives rise to a material removal phenomenon which is called wear. One of the essential applications of this concept, which has received extensive attention in the research and industrial communities, is measuring tire tread wear and, consequently, predicting tire life. In general, wear is correlated with friction. However, various parameters complicate the assessment and analysis of wear and material removal. Such parameters include, but are not limited to, chemical characteristics of the material, pressure, velocity, slip ratio, as well as temperature. Analysis of rubber wear is particularly complicated because of the hyper-elastic and viscoelastic properties of rubber. This level of complexity renders any attempt at accurate wear prediction with analytical models infeasible, if not impossible. In the absence of such explicit analytical models, numerical models have to be used to estimate wear.

In this chapter, the numerical method for predicting wear and friction is explained. In the first step, Savkoor friction model is defined in section 5.1. Several semi-empirical models can predict friction. In this study, the Savkoor Model was used due to its accuracy and the fact that pressure and velocity are taken into account in this Model.

Besides, a new semi-empirical wear model to predict the wear rate is developed. This model depends on the material and environmental properties, such as speed, slip ratio, pressure, and friction coefficient. As dissipation energy is almost constant [79] for surfaces with root mean square (RMS) between 20 – 60 micro mm, the empirical wear model is based on the surfaces' frictional dissipation energy. Two approaches are used for implementing the

wear: ribbon-based and node-based.

For the round sample and tire with longitudinal grooves, we used the ribbon-based model, and for the tire with a complicated tread pattern, we used the node-based model. In sections 5.4 and 5.3, the details of these two methods are explained.

5.1 Friction model (Savkoor model)

Savkoor proposed a semi-empirical model based on the Grosch experimental results [25]. This Model can be used for creating an isothermal master curve for friction coefficient values, as shown in Equation 2-15-1:

$$\mu(v) = \mu_s + (\mu_{max} - \mu_s) \exp\left\{-h^2 \log^2\left(\frac{v}{v_{max}}\right)\right\} \quad 5\text{-}1$$

Where v_{max} is the speed with maximum friction, μ_s is the static friction coefficient, and its maximum value is μ_{max}. h is a factor that can be obtained using experimental data. This factor determines the range of velocities. Both v_{max} and μ_{max} are dependent on the rubber compound viscoelastic properties and temperature. The changes in the temperature cause a shift in the friction curve towards higher velocities.

Researchers modified the Savkoor Model by adding the effect of pressure on this equation.

The modified Savkoor modal is shown in Equation 5-2:

$$\mu(v, P) = \left(\frac{p}{p_0}\right)^{-k}\left[\mu_s + (\mu_{max} - \mu_s)e^{-h^2 ln^2\left(\frac{|v|}{V_{max}}\right)}\right] \quad 5\text{-}2$$

As Equation 5-2 shows, Savkoor's friction law depends on pressure and velocity. However, the same equation can be implemented for different conditions. The assumption is those parameters are not constant and are functions of surface roughness, contact temperature, and speed.

For implementing the semi-empirical friction Savkoor model, the Ufric-coeff and Ufric subroutines were used for the ribbon-based and node-based approaches, respectively. These subroutines can be implemented to define the frictional behavior between two surfaces in contact and when the complex definition of shear transmission in contact is required. Also, they can use and update solution-dependent state variables. For the outputs of these subroutines, friction, and derivative of friction with respect to temperature, velocity and pressure should be defined. For defining the Savkoor friction model, slip rate and pressure variable were used.

Cpress is used to define the contact pressure, and Cslip defines the sliding velocity between two surfaces. Also, a limit for pressure and sliding velocity was added to avoid computational singularities.

5.2 Wear Model (novel semi-empirical Model)

Wear phenomenon is complicated and depends on different conditions, so the best way to predict the wear is by developing a new semi-empirical model related to the material properties and operational conditions. For example, several researchers such as Schallamach, Archard, and Lewis found that wear is a function of load and slip velocities. Others believe that wear rate depends on frictional dissipation energy. Table 5-1 shows some of the famous models that can predict wear.

Table 5-1: different semi-empirical wear model [34], [80]–[85]

Name	**Wear Model**
Cho	$\overline{W} = C\tau^{p}\dot{\gamma}^{q}$
Tamada	$\dot{W} = k\int shear\ stress\ .slip\ dt$
Bin Ma	$\dot{W} = k(w)^{n}$ $\quad$ $w = \mu.P.\Delta l$
Archard wear Model	$\dot{W} = \frac{K}{H}\ pAv$
D.Zheng	$\dot{W} = \alpha.\ \dot{E}^{\beta}$
N.Viswanath	$\Delta V = k.p^{x}.v^{y-z}.t^{y}.\gamma^{(3-y+z)}.\ E^{(y-x-3)}.\left(\frac{C_p}{k}\right)^{z}$
Goreham	$W = K.(CS).\sigma.d$
Sakai	$h = K.w.p.s.(1+3\mu^{2})$

Frictional dissipation energy is an index for defining wear and is calculated by summation of multiplication of slip ratio by shear stress in the surface's contact as shown in Equation 5-3 :

$$Frictional\ disipation\ energy = \int Shear\ stress.slip\,.dt \qquad 5\text{-}3$$

Shear stress has a relation with contact pressure and friction coefficient. The slip ratio is sliding velocity over the speed. Some researchers, such as Tamada [86], use the linear relation between the frictional dissipation energy and wear rate. However, the experimental data collected with linear friction and dynamic friction testers found that the logarithm of the frictional dissipation energy has a linear relation with the logarithmic wear rate. Based on this observation, the new semi-empirical Model for predicting the wear rate is developed.

$$Log(Wear\ Energy) = C1 * Log(\int (shear\ stress.\ Slip)\ dt) \qquad 5\text{-}4$$

Combining the Savkoor Model and Archard wear and accounting for Equation 5-4, nonlinear relations between wear and pressure, sliding velocity, and slip can be observed. Equation 5-5 shows the new semi-empirical Model developed in this research.

$$V = (K/H).(P)^{C_1}.(\dot{y})^{C2}.(s)^{C_3} \qquad 5\text{-}5$$

Where H is the material hardness, P is the contact pressure, $\dot{y}$ is the slip ratio and s is the speed. Two approaches were used to implement this semi-empirical Model in Abaqus, ribbon-based and node-based.

For the validation of the semi-empirical wear model, the experimental data from DFT and LFT were used, and as can be seen in Table 5-2 and Figure 5-1, there is good agreement between the results of the fitted model and experimental data for samples A and B.

Table 5-2: Coefficient of semi-empirical wear model for samples A and B by using LFT

	K/H	C1	C2	C3	R-Sq
Sample A	0.25196	1.10167	0	0.956387	98.9%
Sample B	0.139737	0.931405	0	0.948531	99.4%

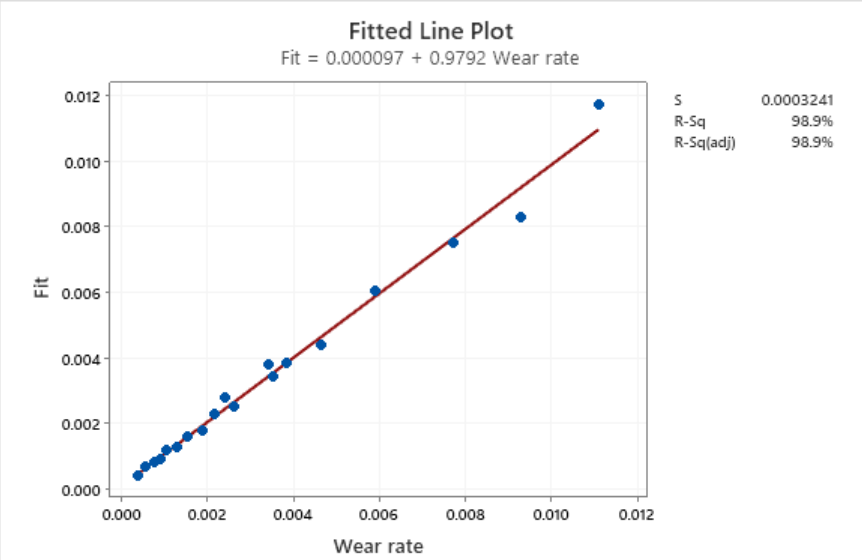

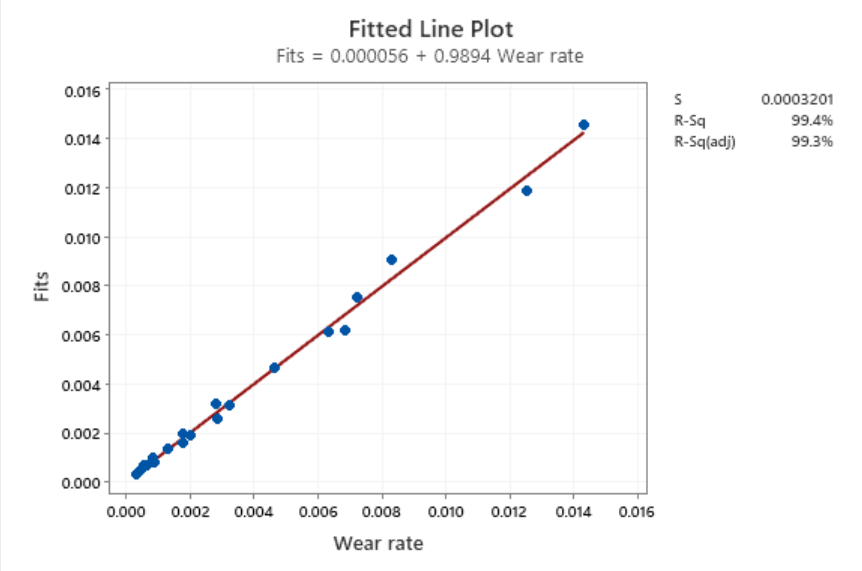

Figure 5-1: Correlation between the experimental data and data using the semi empirical model for samples A and B by using the LFT

5.3 Ribbon base

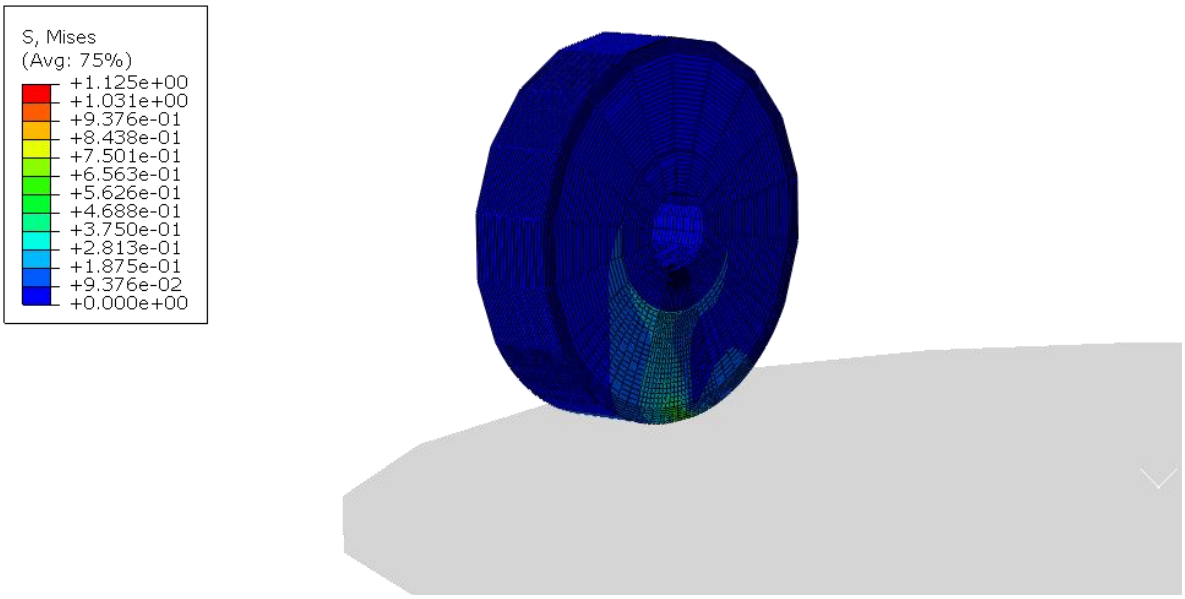

Figure 5-2 : Ribbon base

The ribbon-based (Figure 5-2)approach can model the geometry that revolves around it, so this method is defined for modeling the tire and the rubber sample. The ribbon-based method is employed relying on these two basic assumptions:

1. The wear rate in each ribbon is constant.

2. The width of each ribbon is constant during the rotation.

Slip velocity and pressure can be calculated in Abaqus. However, the steady-state transport used the Eulerian formulation, slip velocity and pressure in each streamline should be defined to model the round rubber sample's wear rate. In Equation 5-6, $\dot{q}$ is defined as the wear rate as a function of the local material depression.

$$\dot{q} = \int \dot{h}\,(s).T(s)ds \qquad 5\text{-}6$$

Node wear rate in each streamline and streamline's thickness is constant due to the assumption of ribbon-based method, so we can rewrite Equation 5-6 for discrete Model which results in Equation 5-7:

$$\dot{q} = \dot{h}.T.\sum \Delta s_i \qquad 5\text{-}7$$

The summation of the semi-empirical wear for each contact node multiplied by the contact area of each node is equal to the sample's wear rate resulting in Equation 5-8:

$$\dot{q} = \sum (K/H).(P_i)^{C_1}.(\dot{y}_i)^{C2}.(s_i)^{C_3}.\Delta A_i \qquad 5\text{-}8$$
$$= T.\sum (K/H).(P_i)^{C_1}.(\dot{y}_i)^{C2}.(s_i)^{C_3}.\Delta s_i$$

Using the assumption that the variation in stream ribbon width can be neglected, $T_i = T$, and recognizing that the nodal contact area $A_i = T\Delta s_i$ enables a more straightforward expression that does not require the use of contact area, and considering Equation 5-7 and Equation 5-8, we can obtain Equations 5-9 and 5-10:

$$\dot{h}.T.\sum \Delta s_i = T.\sum (Uref).(P_i)^{C_1}.(\dot{y}_i)^{C2}.(s_i)^{C_3}.\Delta s_i \qquad 5\text{-}9$$

Where Δs is the sliding distance, and Uref is equal to K/H.

$$\dot{h} = \frac{\sum(Uref).(P_i)^{C_1}.(\dot{y}_i)^{C2}.(s_i)^{C_3}.\Delta s_i}{\sum \Delta s_i} \qquad 5\text{-}10$$

The Δs is determined from streamline nodal coordinates, accessed from variable COORD

$$\Delta s = 0.5 * (distance\ to\ previous\ node + \ distance\ to\ next\ node) \qquad 5\text{-}11$$

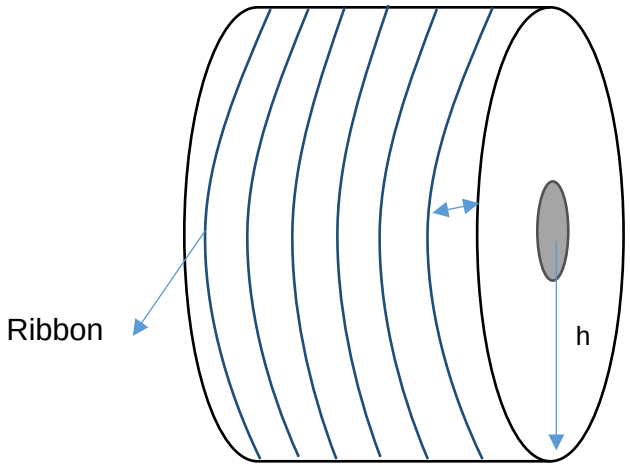

Figure 5-3: schematic of ribbon base

5.3.1 Simulation process for the ribbon-based approach

In the first step, the 2D geometry of the round rubber sample is sketched. Since Umesh-motion does not have the ability to work with hyperelastic material now, the sample is divided into two sections in terms of material properties; the section in contact with the surface is viscoelastic and other parts are hyper-viscoelastic, as can be seen in Figure 5-4.

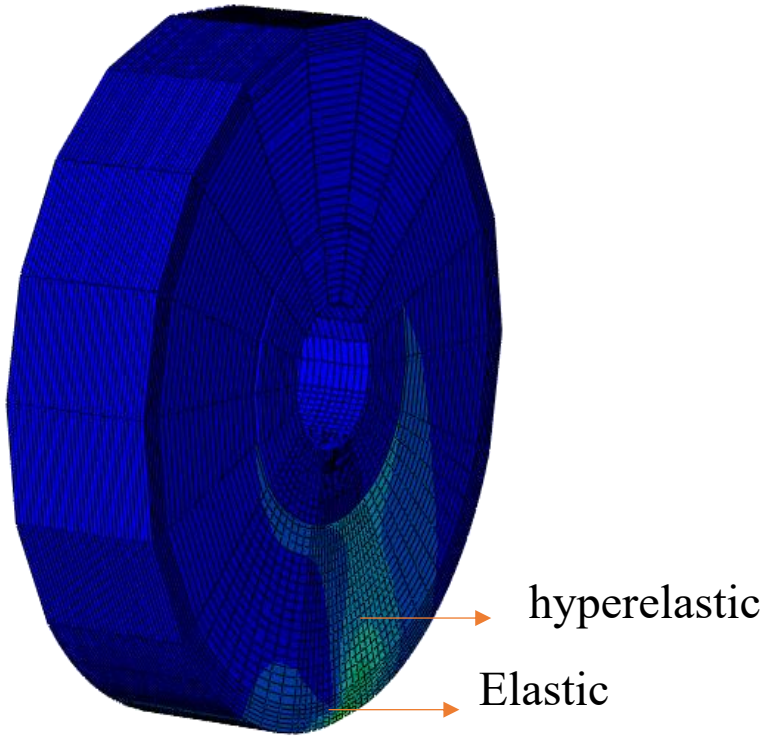

Figure 5-4: Round rubber sample with two different material sections

Neo Hooken hyperelastic properties are used in this research to be consistent with the available experimental limitations. For the viscoelastic material, the Prony series is used. Table 5-3 shows the material properties for rubber sample A.

Table 5-3: material properties for rubber sample A

Material Compound	Material Model	Coefficients
SRI Compound A	*Neo-Hookean Model*	$C10$=0.518335 MPa
	Prony series coefficients	$G0$=332 MPa $g1$=6.0891e−09; $\tau1$=1.1102e−15 $g2$=0.76986375; $\tau2$=1.7682e−07 $g3$=0.21896934; $\tau3$=1.4268e−05 $g4$=0.00693740; $\tau4$=0.02703672 $g5$=0.00203880; $\tau5$=16.6836081

After that, the 2d sample is revolved and transferred to the 3d sample. Also, the rigid analytical surface is created in this step for modeling the sandpaper. The friction coefficient between the rubber sample and the surface is defined by implementing the Savkoor Model and using the Ufric_coeff subroutine. Then after restarting the simulation pipeline, to steady-state transform, linear velocity and rotational velocity of the sample were applied. The entire simulation pipeline is shown in Figure 5-5.

Model rolling and sliding contact is computationally expensive when using a traditional Lagrangian formulation. In this method, the material attached to the reference frame and a fine mesh is required along with the cylinder's entire surface.

In this method, there is a frame of reference moving with the cylinder such that an observer on that frame would perceive the cylinder as being fixed in space, whereas in reality (seen from the perspective of a fixed frame of reference), the cylinder’s material is actually moving. This moving frame of reference is used to make the problem stationary (independent o f time),

where the point is fixed, and the material moves through it. This results in the cylinder mesh not spinning in the moving frame of reference, thereby limiting the requirement for a fine mesh to areas near the contact points.

Besides, using the ALE (Adaptive Lagrangian-Eulerian) method and using the Umesh motion, we can update the rubber sample's nodal coordinate in each streamline.

ALE is an adaptive meshing technique that allows for significant deformation or material removal without compromising the accuracy of the mesh substantially, as, in this method, the mesh is inherently decoupled from the material. However, the topology of the mesh is not modified. In other words, the connectivity of the elements is not affected during deformation, which means that extreme deformations are compromised in rendering.

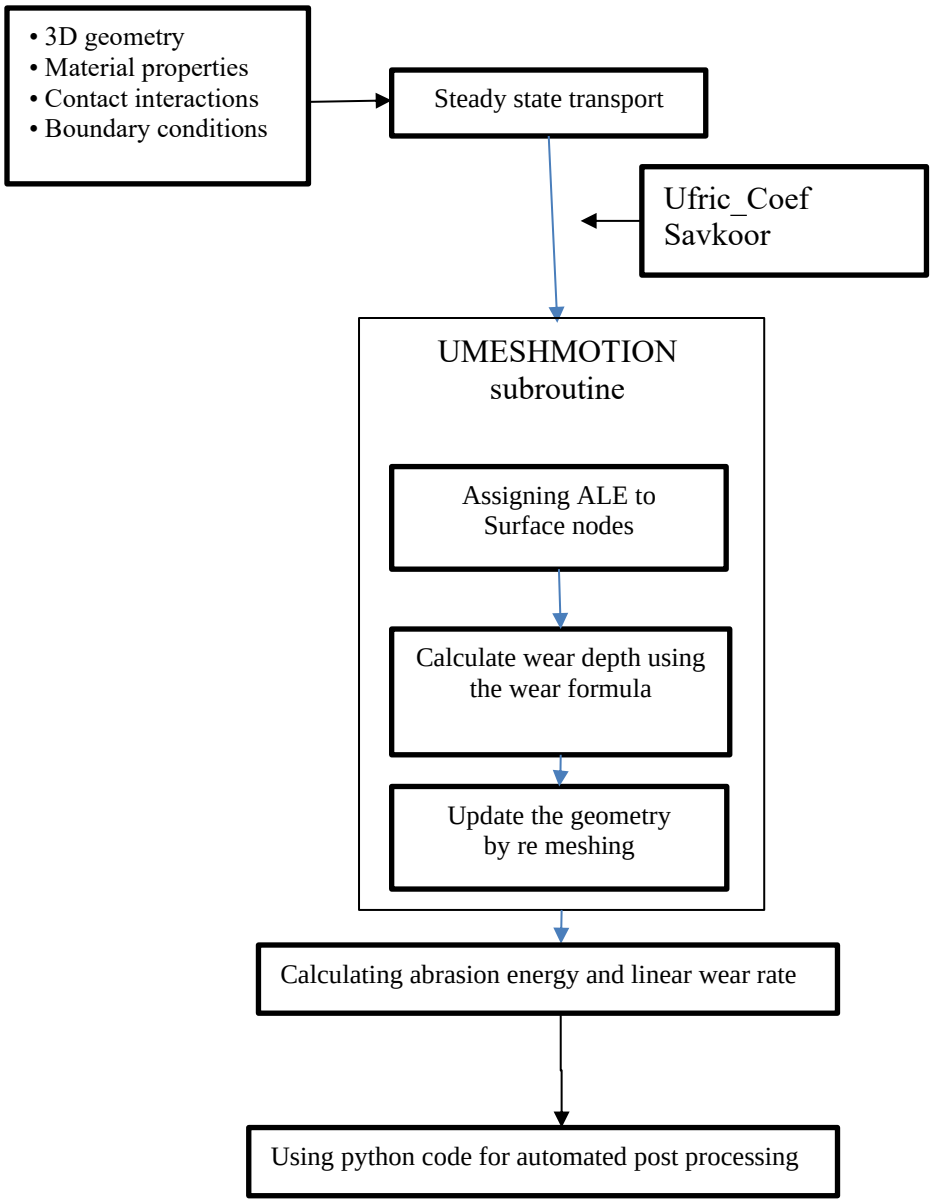

Figure 5-5: Flowchart for Ribbon base Method

5.3.2 Results of using the ribbon base method

Figure 5-6 and Figure 5-7 illustrate the gradual increase in the wear rate of the round rubber sample by increasing the sliding velocity. By increasing the normal load, the wear rate of the rubber sample increases. In this graph, blue lines show the experimental data from DFT for the rubber sample A sliding on sandpaper 120 grit for different sliding velocities and normal pressures. The red graph shows the result from the newly developed semi-empirical wear model that was implemented in Abaqus.

As illustrated in Figure 5-7, the simulation results have a good agreement with the experimental data for the round rubber sample, by which the R square of these data is 91 percent. The small error between the simulation and experimental data is due to the assumptions needed to implement the ribbon base model, uncertainties of the experimental data, and also neglecting the thermal effect in this model.

In addition, Figure 5-6 shows that the wear rate has a nonlinear relationship with the sliding velocity and pressure, which justified the assumptions for finding the semi-empirical model.

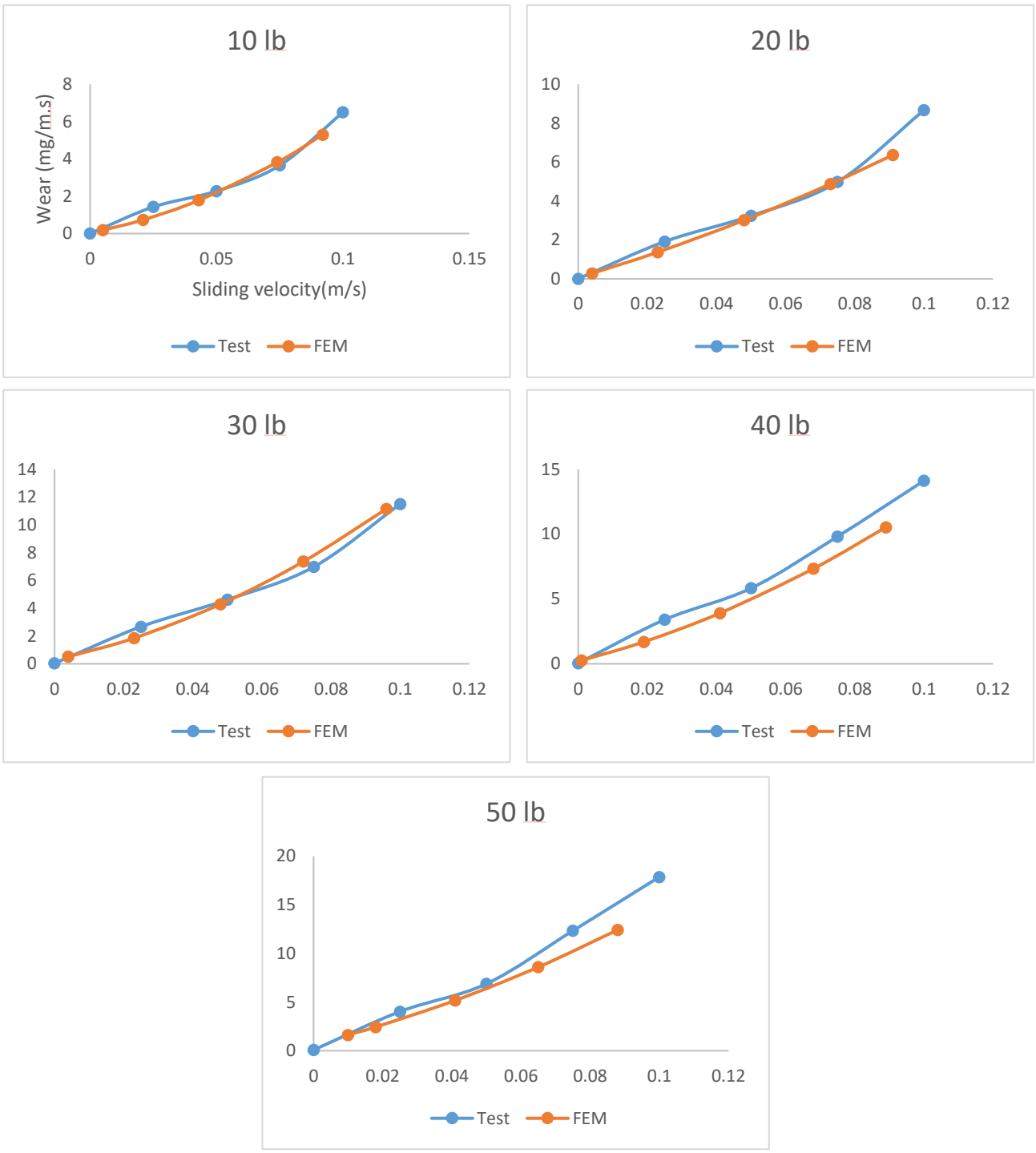

Figure 5-6: Experimental data from DFT VS. Result from simulation in different pressure and sliding velocity for sample A

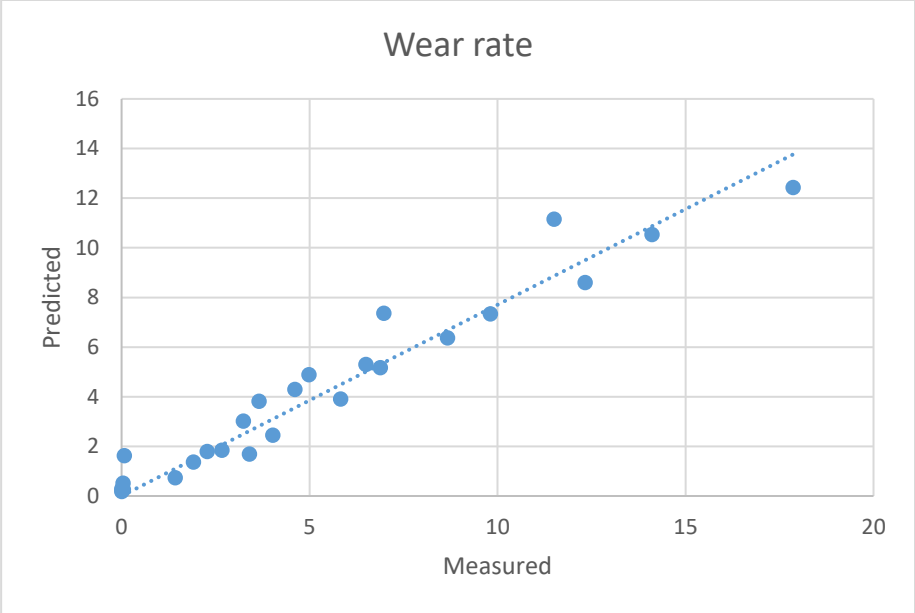

Figure 5-7: Predicted wear by simulation Vs. Measured wear from DFT

5.4 Node-Based Approach

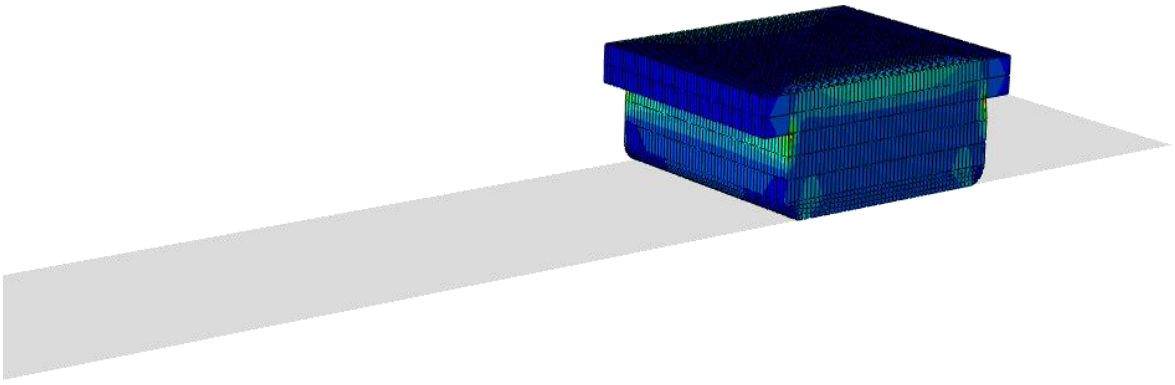

Figure 5-8: Node base

For the node-based method (Figure 5-8), the problem is solved without considering the ribbon-based method's assumptions. The node-based method can model any geometry either with or without revolving, so by implementing this method, one can measure heel and toe wear and uneven wear in tire modeling. Also, the node-based method is computationally expensive because of using a traditional Lagrangian formulation.

For the node-based method $\dot{q}$ can be expressed as a function of the local material recession rate by Equation 5-12

$$\dot{q} = \int \dot{h}\,(s).T(s)ds \qquad 5\text{-}12$$

As the node-based method eliminates the ribbon-based method's assumptions, we can rewrite Equation 5-12 as a discrete form.

$$\dot{q} = \sum \dot{h}_{\iota} \Delta A_i \qquad 5\text{-}13$$

We also can rewrite Equation 5-13 for the whole Model, as shown in Equation 5-14

$$\dot{q} = \sum (K/H).(P_i)^{C_1}.(\dot{y}_i)^{C2}.(S_i)^{C_3}.\Delta A_i \qquad 5\text{-}14$$

5.4.1 Simulation process for the node-based approach

Figure 5-9 shows the procedure of applying the wear and updating the nodal coordinate in Abaqus for the node-based method. For implementing the wear procedure in the first step, we should define the geometry of the sample and material properties. As ALE (Adaptive Lagrangian-Eulerian method) is not working with the hyperelastic material, we need to define two sections in the Model, same as the ribbon-based model. After that, the 3D sample was created by extruding the 2d sample. Also, the rigid analytical surface was created in this step for modeling the sandpaper.

To reduce the computational time, the Model runs for a particular time and finds the wear rate. Then the simulation runs in dynamic implicit mode until the specific step time and the Ufric subroutine calculates the sample's friction and wear rate. The simulation is restarted to

General Static mode and uses UMESH-MOTION subroutine to update the nodal coordinate. This process is repeated until the simulation reaches the target time. For the tire simulation, factor F is implemented to reduce the computational time by considering the assumption that wear rate has a linear relationship with time [87]. So the total wear can be calculated by using Equation 5-15. In this equation, F is the acceleration factor.

$$\dot{q}_T = \sum F.(K/H).(P_i)^{C_1}.(\dot{y}_i)^{C_2}.(s_i)^{C_3}.\Delta A_i \qquad 5\text{-}15$$

Later, using the FORTRAN user subroutine, the contact surface nodes are modified based on Equation 5-14, as shown in Figure 5-9.

At that time, subroutine UFric calculated the friction from the semi-empirical Savkoor friction model and calculated each node's wear rate from the modified semi-empirical Model. By restarting the Model to "General Static" and using the UMESH-MOTION subroutine, Abaqus updates each node's nodal coordinate given the Ufric subroutine's value calculated before. The UMESH-MOTION subroutine is available in the General Static mode. The Model, in this case, involves complications such as non-linear deformations and inertia, which require the dynamic-implicit mode. However, at the time of this writing, ALE is not available in the dynamic-implicit mode. To solve this issue, the simulation should restart the Model to the dynamic-implicit mode. However, presently, Abaqus cannot restart dynamic implicit to General Static if the Model contains the ALE method, so to overcome this problem, we first restart the Model to General Static without the ALE method and after that restart that one to dynamic implicit until the desired time.

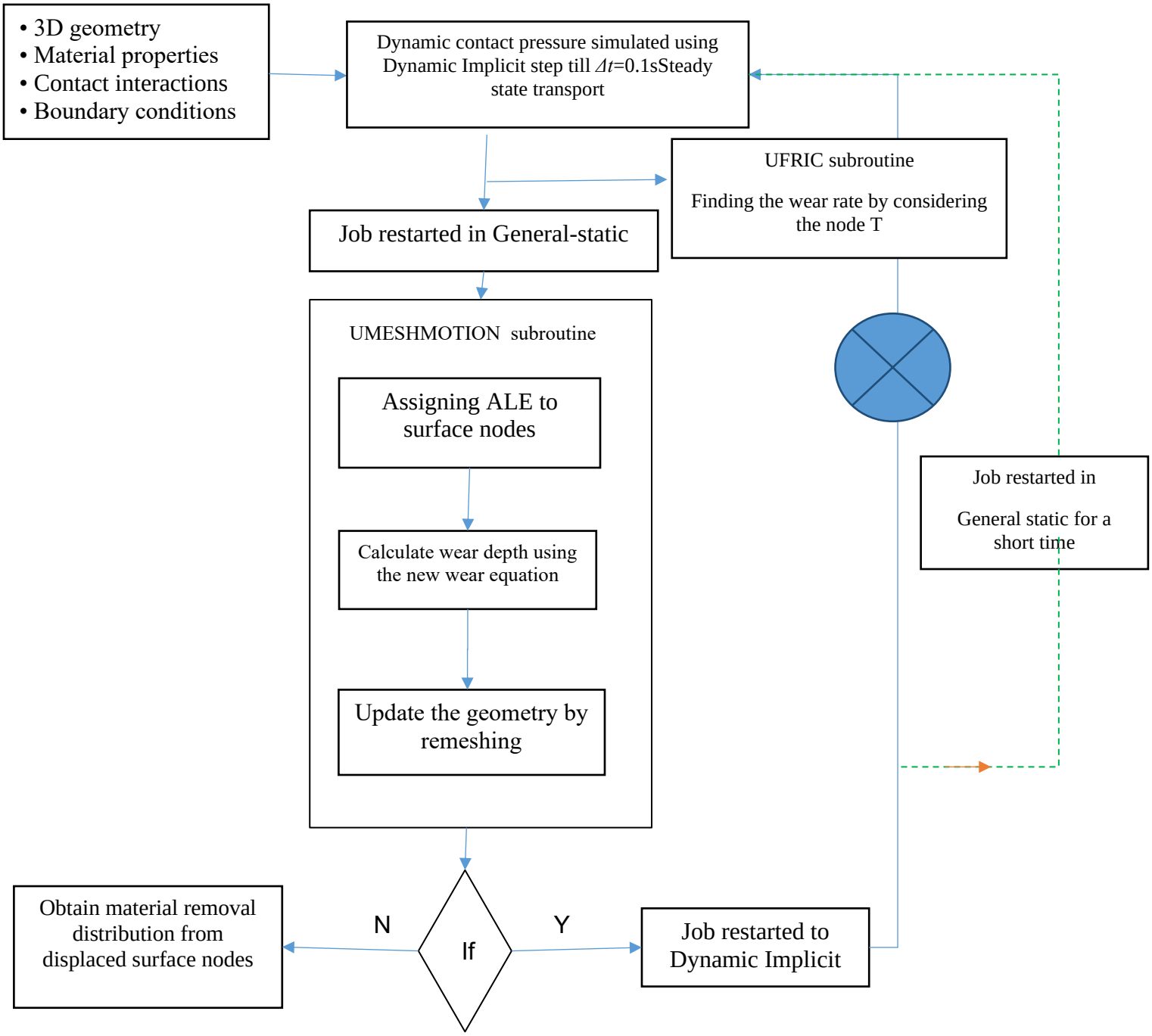

Figure 5-9: Flowchart for the Node base Method

5.4.2 Result of Node base method

Figure 5-10 and Figure 5-11 illustrate a gradual increase in the wear rate of the rectangular rubber sample by increasing the sliding velocity. By increasing the normal load, the wear rate of the rubber sample increases. This graph shows the experimental data from LFT for rubber sample A sliding on sandpaper 120 grit with different sliding velocities and normal pressures. The result from the newly developed semi-empirical wear model implemented in Abaqus is shown in Figure 5-10

As illustrated in Figure 5-11, simulation results have a good agreement with the experimental data for the rectangular rubber sample, by which the R square of these data is 97 percent. Similar to the results obtain by the ribbon-based method, there is a small error between the simulation and experimental data due to the existing uncertainties in the experimental data and neglecting the thermal and surface characteristics effects in this model.

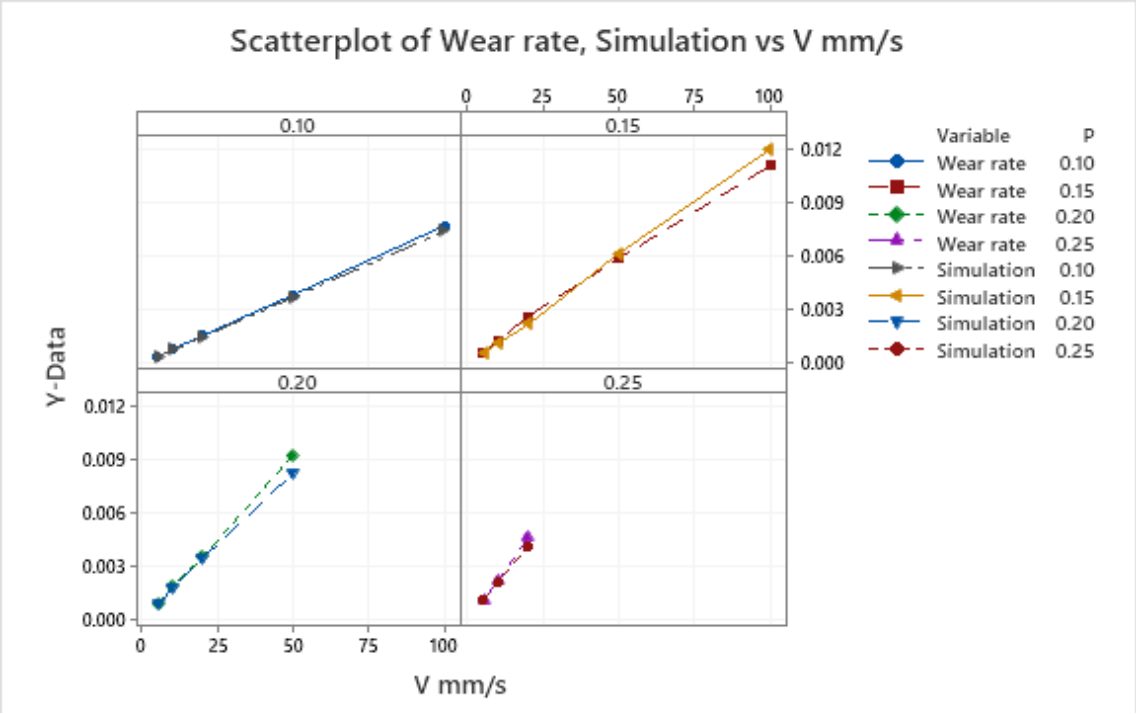

Figure 5-10: Experimental data from LFT VS. Result from simulation (Node-base) in different pressure and sliding velocity for sample A

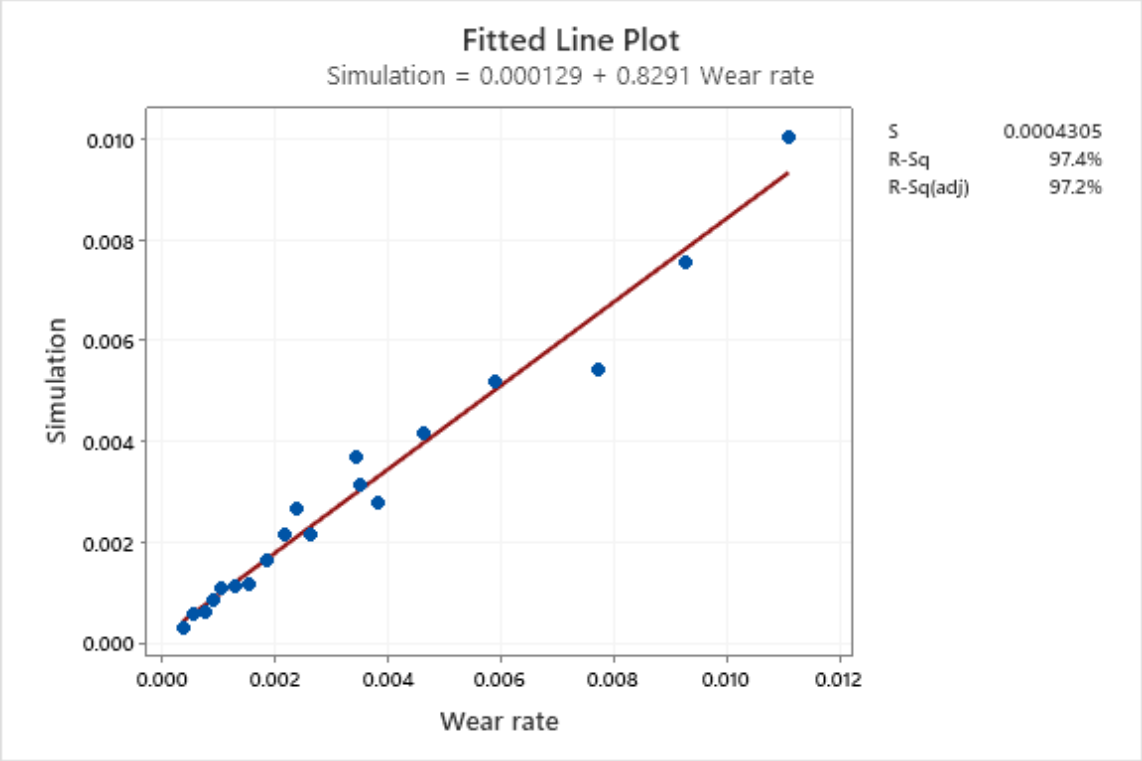

Figure 5-11: Simulation wear rate result VS. experimental data from LFT

Chapter 6

Summary of research outcome

The main objective of this study was to obtain the friction coefficient and the wear rate for different rubber blocks in contact with different surfaces via three approaches: (Experimental method, analytical method, and numerical method).

A novel linear friction tester was designed and manufactured to experimentally study the rubber blocks' wear and friction. The new test setup has several advantages over existing test setups in this field, such as covering a higher range of velocities while maintaining high precision. In addition, for this study, the existing dynamic friction tester at the CenTiRe laboratory was modified. These modifications allow the tests for different temperatures or different oxygen levels to the dynamic friction tester. These two setups were used to measure the rubber's friction and wear in contact with different surfaces for different testing conditions, such as different normal loads and different velocities.

The data collected by the experiment shows that the friction coefficient is dependent on the normal pressure, velocity, contact temperature, and ambient temperature. The data collected using the linear friction tester was validated using the dynamic friction tester's data. From the results, the friction coefficient increases by increasing the contact temperature. From the results obtained by conducting the tests using both the linear friction tester and the dynamic friction tester, the friction coefficient increases with an increase in the sliding velocity until reaching its maximum value, and then it drops. The increase in normal pressure causes a dramatic decrease in the values of the friction coefficient.

Results showed that when the ambient temperature increases, the wear rate of the rubber decreases. However, increasing the velocity causes an increase in the wear rate of the rubber.

Data collected from conducting the tests using both setups were used later to validate the developed analytical and numerical models.

To obtain the rubber wear rate using the analytical approach, the rubber's real contact area and friction were calculated using Persson's model. In order to obtain the friction coefficient and the real contact area, the surface was simulated using data collected from Profilometer via the Matlab code programmed for this study to simulate the randomly rough surfaces. After obtaining the friction coefficient and the real contact area, the rubber's wear rate was calculated using a novel approach by combining the Persson Powdery Rubber Wear model with the Crack Propagation model.

Another novelty of this study is incorporating the effect of temperature changes in wear rate. To this end, the effect of temperature changes on the friction's hysteresis and adhesive mechanism were investigated. To incorporate the temperature and change into the adhesive model, a new shift factor is designed to predict the friction coefficients' values more accurately. The effect of temperature on the crack energy dissipation was investigated by considering the changes in Young's modulus and friction coefficient caused by the change in the temperature.

The developed model was validated using the data collected by a linear friction tester. Comparing the results shows a good agreement between the data collected experimentally and the analytical approach's obtained results. The improved model results show that the real contact area of the rubber decreases by increasing the values of the RMS of the surface and decreasing the Hurst function values. In addition, an increase in the sliding velocity causes a decrease in the real contact area's values.

Using the developed analytical model, the effects of the surface characteristics on the friction coefficient were investigated. From the results, by increasing the Hurst function for the low-velocity region, the friction coefficient increase. However, for the high-velocity region, the friction coefficient decreases by increasing the Hurst function. An increase in the

RMS values causes a decrease in the friction coefficient.

From the results obtained by the analytical model for the wear rate of the rubber, by increasing the velocity, the wear rate increases.

Wear phenomena are complicated and depend on different conditions, so the best way to predict the wear is by developing a new semi-empirical model related to the material properties and operational properties

a new semi-empirical wear model to predict the wear rate is developed, which depends on the material and environmental properties, such as speed, slip ratio, pressure, and friction coefficient. Two approaches are used for implementing the wear: ribbon-based and node-based. The ribbon-based model was used for the round sample and tire with longitudinal grooves, and for the tire with complicated tread, the node-based model was used.

The ribbon-based approach can model the geometry that revolves around it, so this method is defined for modeling the tire and rubber sample. The ribbon-based method is employed relying on these two basic assumptions:

1. The wear rate in each ribbon is constant.

2. The width of each ribbon is constant during the rotation.

For the node-based method, the problem is solved without considering the ribbon-based method's assumptions. In addition, the node-based method can model any geometry either with revolving or without revolving, so by implementing this method, heel and toe wear and uneven wear can measure in tire modeling. Also, the node-based method is computationally expensive because of using a traditional Lagrangian formulation.

For implementing the semi-empirical wear model, The Umeshmotion subroutines and ALE method were used. This subroutine can update the nodal coordinate by calculating the wear rate of the sample. And also, for implementing the semi-empirical friction Savkoor model, the Ufric-coeff and Ufric subroutines were used for the ribbon-based and node-based approaches, respectively. These subroutines can be implemented to define the frictional behavior between two surfaces in contact and when the complex definition of shear

transmission in contact is required. Also, they can use and update solution-dependent state variables.

From the results obtained by the numerical model for the wear rate of the rubber, the ribbon base method and Node base method can predict the wear rate of the rubber sample with less error in comparing with the analytical model.

The main outcomes of this research are:

- Comprehensive literature review on the existing studies on the friction and wear of the viscoelastic materials
- Designed and manufactured a linear sliding friction tester
- Comparative results were presented for the data collected by the conducted tests using the linear sliding friction tester and the dynamic friction tester
- The effect of different operating conditions such as normal load, velocity, rubber compound material, surface type, surface characteristics, and temperature on wear mechanism, obtained using the Linear friction tester and the Dynamic friction tester
- Dynamic friction tester was modified by adding a chamber and systems required to control the temperature, humidity, and oxygen level during the tests.
- A comprehensive analytical wear model was developed in order to estimate the friction coefficient of the tread and tire durability.
- A new semi-empirical wear model was developed for predicting the wear rate of the rubber sample
- Semi-empirical wear model implemented to Abaqus by using different subroutines such as Umeshmotion, UFric, and UFric_coeff for different geometries.

Further work

- Extending the Wear and friction semi-empirical models by considering the surface characteristic and environmental temperature
- Extendending the computational model by adding the thermal model
- Extending the Wear and friction model for the actual tire.
- Improving the model by adding the terms for wet surface
- Improving the linear friction tester by adding the chamber on that to understanding the effect of the temperature on wear and friction of rubber sample
- Adding a mechanism to the linear friction tester for testing the round rubber sample
- Study on the effect of geometry on wear
- Improving the Savkoor friction model by adding the items for surfaces and speed and temperature
- Finding the relation between sample wear and tire wear
- Add the effect of micro crack on material properties of rubber in contact with the surface in the computational model
- Investigating the impact of aging on tire wear and friction.

Appendix A: Electrical Box

A.1 DAQ

A USB-6341 (Figure A. 1) is used for digital and analog I/O. This data acquisition system allows for many devices to be connected and monitored or controlled using NI LabVIEW.

Figure A. 1: USB-6341

A.2 Fuses

Fuses were selected for this application instead of a circuit breaker due to their quick response time to power surges. 3 fuse holders (Figure A.2) are connected between the power supply and servo drive.

Figure A. 2: Fuse holders

A.3 Solenoid valves

Two solenoid valves (Figure A. 3) are used to control airflow to the pneumatic cylinders under the table. A digital signal, controlled from LabVIEW, is provided by the DAQ to turn the valves on and off, thus raising or lowering the tracks and carriage.

Figure A. 3: Solenoid valves

A.4 Proportional valve

To accurately normal force on the sample, the pressure in the pneumatic cylinder is varied using a Proportion Air proportional valve. An analog signal to the proportional valve is controlled via a PID controller in LabView; the force on the normal load cell is input into LabVIEW, and voltage to the valve is varied to drive the force to the desired value.

Figure A. 4: Proportional valve

A.5 Servo driver

The driver for the servo motor has specifications given in the ‘Servo with Driver’ section. The servo was configured using ASDASoft software on a PC; more details on using ASDASoft are given in Appendix B.

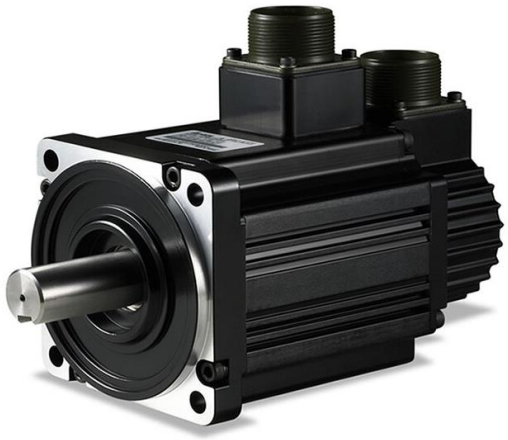

Figure A. 5: Servo motor Delta 2KW

Appendix B: Testing Operation Procedure

1. Turn on power to the electrical box by pulling down on the lever
2. Turn on fuses by pulling down on switches
3. Ensure air hose valve is open; if not, turn valve 90 degrees.
4. Check that all emergency stops are off by pulling them outward.
5. Turn servo on: turn the black switch on the control panels far clockwise as possible. The motor should start humming quietly.
6. Open the LabView file ‘Main.vi’ on the PC. When ready to start testing, click the ‘Run’ button on the toolbar details given in Appendix C.
7. Adjust speed and acceleration parameters in ASDA soft. Details on ASDA-soft for this application are given in Appendix A.
8. To start a routine, press the green button on the control panel. Use the red button to stop the routine and return the carriage to the homing origin.

Bibliography

[1] H. Hertz, “Miscellaneous Papers by Heinrich Hertz,” *MacMillan Co*, pp. 146–183, 1896.

[2] J. A. Greenwood, K. L. Johnson, and E. Matsubara, “A surface roughness parameter in Hertz contact,” *Wear*, vol. 100, no. 1–3, pp. 47–57, 1984.

[3] A. Emami and S. Khaleghian, “Investigation of tribological behavior of Styrene-Butadiene Rubber compound on asphalt-like surfaces,” *Tribol. Int.*, vol. 136, no. November 2018, pp. 487–495, 2019.

[4] R. Van Der Steen, I. Lopez, B. De Bruijn, A. J. C. Schmeitz, and H. Nijmeijer, “Tyre/road friction modeling Literature survey,” 2007.

[5] P. Wagner, P. Wriggers, C. Klapproth, C. Prange, and B. Wies, “Multiscale FEM approach for hysteresis friction of rubber on rough surfaces,” *Comput. Methods Appl. Mech. Eng.*, vol. 296, pp. 150–168, 2015.

[6] B. N. J. Persson, “Contact mechanics for randomly rough surfaces,” *Surface Science Reports*, vol. 61, no. 4. pp. 201–227, Jun-2006.

[7] B. J. Briscoe and S. K. Sinha, “Wear of polymers,” *Proc. Inst. Mech. Eng. Part J J. Eng. Tribol.*, vol. 216, no. 6, pp. 401–413, 2002.

[8] B. N. J. Persson, “Theory of rubber friction and contact mechanics,” *J. Chem. Phys.*, vol. 115, no. 8, pp. 3840–3861, 2001.

[9] A. Emami, P. D. Dissertation, and S. Case, “Investigation on physics-based multi-scale modeling of contact , friction , and wear in viscoelastic materials with application in rubber compounds.”

[10] B. N. Persson, F. Bucher, and B. Chiaia, “Elastic contact between randomly rough surfaces: Comparison of theory with numerical results,” *Phys. Rev. B - Condens. Matter Mater. Phys.*, vol. 65, no. 18, pp. 1841061–1841067, 2002.

[11] A. Schallamach, “Abrasion of rubber by a needle,” *J. Polym. Sci.*, vol. 9(5), pp. 385–404, 1952.

[12] A. Schallamach, “On the abrasion of rubber,” *Proc. Phys. Soc.*, vol. 67(12), p. 883, 1954.

[13] K. Grosch and A. Schallamach, “Relation between abrasion and strength of rubber,” *Rubber Chem. Technol.*, no. 39(2), pp. 287–305, 1966.

[14] A. Mishra, “Dry Sliding Wear Behavior of Epoxy-Rubber Dust Composites,” *Int. J. Mech. Mechatronics Eng.*, vol. 6, no. 7, pp. 1218–1223, 2012.

[15] M. A. Chowdhury, “Experimental Investigation on Friction and Wear Properties of Different Steel Materials Tribology in Industry,” *Tribol. Ind.*, vol. 35, no. 1, pp. 42–50, 2013.

[16] Sivaraos *et al.*, “Friction performance analysis of waste tire rubber powder reinforced polypropylene using pin-on-disk tribometer,” *Procedia Eng.*, vol. 68, pp. 743–749, 2013.

[17] S. Hemette, J. Cayer-Barrioz, and D. Mazuyer, “Friction setup and real-time insights of the contact under controlled cold environment: The KŌRI tribometer for rubber-ice contact application,” *Rev. Sci. Instrum.*, vol. 89, no. 12, 2018.

[18] O. Lahayne, J. Eberhardsteiner, and R. Reihsner, “Tribological investigations carried out by a linear friction tester,” *Trans. Famena*, vol. 33, no. 2, pp. 15–22, 2009.

[19] G. Carbone, B. Lorenz, B. N. J. Persson, and A. Wohlers, “Contact mechanics and rubber friction for randomly rough surfaces with anisotropic statistical properties,” *Eur. Phys. J. E*, vol. 29, no. 3, pp. 275–284, 2009.

[20] B. Lorenz, *Contact Mechanics and Friction of Elastic Solids on Hard and Rough Substrates*. 2012.

[21] J. F. Archard, “Contact and rubbing of flat surfaces,” *J. Appl. Phys.*, vol. 24, no. 8, pp. 981–988, 1953.

[22] D. Dowson, “History of tribology,” *Addison-Wesley Longman Limited.*, 1979.

[23] G. Amontons, “De la resistance caus’ ee dans les machines .,” *Mémoires l’Académie R. A*, pp. 251–282, 1699.

[24] A. Schallamach, “A theory of dynamic rubber friction,” *Wear*, vol. 6(5), pp. 375–382, 1963.

[25] A. Savkoor, “Some aspects of friction and wear of tyres arising from deformations, slip and stresses at the ground contact,” *Wear*, vol. 9(1), pp. 66–78, 1966.

[26] U. Nackenhorst, “Rollkontaktdynamik: numerische Analyse der Dynamik rollender Körper mit der Finite-Element-Methode,” *Inst. für Mech.*, 2000.

[27] L. Dorsch, V., Becker, A., and Vossen, “Enhanced rubber friction model for finite element simulations of rolling tyres, 31(10), pp. .,” *Plast. rubber Compos.*, vol. 31(10), pp. 458–464, 2002.

[28] T. Huemer, W. N. Liu, J. Eberhardsteiner, and H. A. Mang, “A 3D finite element formulation describing the frictional behavior of rubber on ice and concrete surfaces,” *Eng. Comput. (Swansea, Wales)*, vol. 18, no. 3–4, pp. 417–436, 2001.

[29] Z. Radó, “A study of road surface texture and its relationship to friction,” *1996*.

[30] A. Schallamach, “Friction and abrasion of rubber,” *Wear*, vol. 1, no. 5, pp. 384–417, 1958.

[31] A. Schallamach, “The Abrasion of Rubber,” *Rubber Chem. Technol.*, no. 28(3), pp. 906–916, 1955.

[32] K. Grosch and A. Schallamach, “The Load Dependence of Laboratory Abrasion and Tire Wear,” *Rubber Chem. Technol.*, vol. 43(4), pp. 701–713, 1970.

[33] A. Gent and C. Pulford, “Mechanisms of rubber abrasion,” *J. Appl. Polym. Sci.*, no. 28(3), pp. 943–960, 1983.

[34] J. Archard, “Elastic deformation and the laws of friction,” *Proc. R. Soc. London A Math. Phys. Eng. Sci. R. Soc.*, no. 1, pp. 190–205, 1957.

[35] R. Lewis, “Predicting the wear of sliding plastic surfaces(Wear and pressure-velocity limits in unlubricated plastic bearings, piston rings and seals),” *Mech. Eng.*, no. 86, pp. 32–35, 1964.

[36] S. Ratner, I. Farberova, O. Radyukevich, and E. Lure, “Connection between wear resistance of plastics and other mechanical properties,” *Sov. Plast.*, no. 7, pp. 37–45, 1964.

[37] J. k. Lancaster, “Relationships between the wear of polymers and their mechanical properties,” *Proc. Inst. Mech. Eng.*, pp. 98–106, 1968.

[38] B. N. J. Persson, “Rubber friction and tire dynamics,” *J. Phys. Condens. Matter*, vol. 23, no. 1, 2011.

[39] B. N. J. Persson, O. Albohr, G. Heinrich, and H. Ueba, “Crack propagation in rubber-like materials,” *J. Phys. Condens. Matter*, vol. 17, no. 44, 2005.

[40] B. N. J. Persson, “Contact mechanics for randomly rough surfaces,” *Surf. Sci. Rep.*, vol. 61, no. 4, pp. 201–227, 2006.

[41] B. N. J. Persson, “Theory of powdery rubber wear,” *J. Phys. Condens. Matter*, vol. 21, no. 48, 2009.

[42] B. N. J. Persson, “Relation between interfacial separation and load: A general theory of contact mechanics,” *Phys. Rev. Lett.*, vol. 99, no. 12, pp. 1–4, 2007.

[43] H. Davies, “The reflection of electromagnetic waves from a rough surface,” *Proc. IEE-Part IV Inst. Monogr.*, no. 101(7), pp. 209–214, 1954.

[44] D. Léger, E. Mathieu, and J. Perrin, “Optical surface roughness determination using speckle correlation technique,” *Appl. Opt.*, no. 14(4), pp. 872–877, 1975.

[45] Y. Fujii, H., Asakura, T., and Shindo, “Measurement of surface roughness properties by using image speckle contrast,” *JOSA*, no. 66(11), pp. 1217-1222., 1976.

[46] R. A. Sprague, “Surface roughness measurement using white light speckle,” *Appl. Opt.*, no. 11(12), pp. 2811–2816, 1972.

[47] C. Yang and B. N. J. Persson, “Contact mechanics: Contact area and interfacial separation from small contact to full contact,” *J. Phys. Condens. Matter*, vol. 20, no. 21, 2008.

[48] B. N. J. Persson, O. Albohr, C. Creton, and V. Peveri, “Contact area between a viscoelastic solid and a hard, randomly rough, substrate,” *J. Chem. Phys.*, vol. 120, no. 18, pp. 8779–8793, 2004.

[49] J. J. Madge, “Numerical modelling of the effect of fretting wear on fretting fatigue .,” *PhD thesis , Univ. Nottingham*, 2009.

[50] I. Rosu, H. L. Elias-Birembaux, F. Lebon, H. Lind, and M. Wangenheim, “Experimental and numerical simulation of the dynamic frictional contact between an aircraft tire rubber and a rough surface,” *Lubricants*, vol. 4, no. 3, pp. 1–14, 2016.

[51] X. Yang, “Finite element analysis and experimental investigation of tyre characteristics for developing strain-based intelligent tyre system,” no. September, p. 242, 2011.

[52] J. Wu, C. Zhang, Y. Wang, and B. Su, “Wear Predicted Model of Tread Rubber Based on Experimental and Numerical Method,” *Exp. Tech.*, vol. 42, no. 2, pp. 191–198, 2018.

[53] S. Vadakkeveetil, “MULTI – LENGTH SCALE MODELING OF RUBBER TRIBOLOGY FOR TIRE APPLICATIONS,” 2019.

[54] M. Klüppel and G. Heinrich, “Rubber Friction on Self-Affine.,” *Rubber Chem. Technol.*, vol. 73, no. 4, pp. 578–606, 2000.

[55] G. Heinrich and M. Klüppel, “Rubber friction, tread deformation and tire traction,” *Wear*, vol. 265, no. 7–8, pp. 1052–1060, 2008.

[56] B. N. J. Persson, “Rubber friction and tire dynamics,” *J. Phys. Condens. Matter*, vol. 23, no. 1, Jan. 2011.

[57] M. Mofidi, B. Prakash, B. N. J. Persson, and O. Albohr, “Rubber friction on (apparently) smooth lubricated surfaces,” *J. Phys. Condens. Matter*, vol. 20, no. 8, Feb. 2008.

[58] T. V. Tolpekina and B. N. J. Persson, “Adhesion and Friction for Three Tire Tread Compounds,” *Lubricants*, vol. 7, no. 3, p. 20, 2019.

[59] B. Lorenz, B. N. J. Persson, G. Fortunato, M. Giustiniano, and F. Baldoni, “Rubber friction for tire tread compound on road surfaces,” *J. Phys. Condens. Matter*, vol. 25, no. 9, 2013.

[60] A. P. S. Arunachalam and S. Idapalapati, “Material removal analysis for compliant polishing tool using adaptive meshing technique and Archard wear model,” *Wear*, vol. 418–419, no. August 2018, pp. 140–150, 2019.

[61] C. Aaron, “Finite element simulation methods for dry sliding wear,” *Dep. Aeronaut. Astronaut. Eng.*, vol. PhD, no. AFIT/GAE/ENY/08-M03, p. 123, 2008.

[62] H. Hooputra, H. Gese, H. Dell, and H. Werner, “A Comprehensive Failure Model for Crashworthiness Simulation of Aluminium Extrusions.,” *Int. J. Crashworthiness*, vol. 9, pp. 449–463, 2004.

[63] C. Su, “Integrated Experimental Methods and Machine Learning for Tire Wear Prediction,” 2019.

[64] S. Vadakkeveetil, “Multi – Length Scale Modeling of Rubber Tribology for Tire

Applications," 2019.

[65] "No Title." .

[66] J. C. Stover, *Optical Scattering: Measurement and Analysis.* SPIE Press, 1995.

[67] L. R. K, *Introduction to metrology for micro- and nanotechnolog.* Elsevier, 2010.

[68] A. Duparré, J. Ferre-Borrull, S. Gliech, G. Notni, J. Steinert, and J. M. Bennett, "Surface characterization techniques for determining the root-mean-square roughness and power spectral densities of optical components," *Appl. Opt.*, vol. 41, pp. 154–171, 2002.

[69] U. D. Schwarz, O. Zwörner, and R. Köster, Peter Wiesendanger, "Quantitative analysis of the frictional properties of solid materials at low loads. I. Carbon compounds," *Phys. Rev. B (Condensed Matter)*, vol. 55, no. 11, 1997.

[70] U. D. Schwarz, O. Zwörner, and R. Köster, Peter Wiesendanger, "Quantitative analysis of the frictional properties of solid materials at low loads. II. Mica and germanium sulfide," *Phys. Rev. B (Condensed Matter)*, vol. 56, no. 11, pp. 6997–7000, 1997.

[71] R. W. Carpick, N. Agraït, D. F. Ogletree, and M. Salmeron, "Variation of the Interfacial Shear Strength and Adhesion of a Nanometer-Sized Contact," *Langmuir*, vol. 12, no. 13, pp. 3334–3340, 1996.

[72] G. B and L. M. A, "Quantized thermal transport across contacts of rough surfaces.," *Nat. Mater.*, vol. 12, pp. 59–65, 2013.

[73] H. R, *Electric Contacts*. Springer-Verlag Berlin Heidelberg, 1967.

[74] B. N. J. Persson, "Theory of rubber friction and contact mechanics," *J. Chem. Phys.*, vol. 115, no. 8, pp. 3840–3861, Aug. 2001.

[75] B. N. J. Persson, "Elastoplastic contact between randomly rough surfaces," *Phys. Rev. Lett.*, vol. 87, no. 11, pp. 116101-1-116101–4, 2001.

[76] A. G. Peressadko, N. Hosoda, and B. N. J. Persson, "Influence of surface roughness on adhesion between elastic bodies," *Phys. Rev. Lett.*, vol. 95, no. 12, pp. 1–4, 2005.

[77] M. Mahboob Kanafi, A. J. Tuononen, L. Dorogin, and B. N. J. Persson, "Rubber friction on 3D-printed randomly rough surfaces at low and high sliding speeds," *Wear*, vol. 376–

377, pp. 1200–1206, 2017.

[78] B. Lorenz, Y. R. Oh, S. K. Nam, S. H. Jeon, and B. N. J. Persson, “Rubber friction on road surfaces: Experiment and theory for low sliding speeds,” *J. Chem. Phys.*, vol. 142, no. 19, 2015.

[79] G. Stachowiak and A. W. Batchelor, *Engineering tribology*. Butterworth-Heinemann, 2013.

[80] D. Zheng, “Prediction of Tire Tread Wear with FEM Steady State Rolling Contact Simulation,” *Tire Sci. Technol.*, vol. 31, no. 3, pp. 189–202, Jul. 2003.

[81] J. C. Cho and B. C. Jung, “Prediction of Tread Pattern Wear by an Explicit Finite Element Model3,” *Tire Sci. Technol.*, vol. 35, no. 4, pp. 276–299, Dec. 2007.

[82] B. Ma, H. Xu, Y. Chen, and M. Lin, “Evaluating the tire wear quantity and differences based on vehicle and road coupling method,” vol. 9, no. 5, pp. 1–13, 2017.

[83] N. Viswanath and D. G. Bellow, “of an equation,” vol. 183, pp. 42–49, 1995.

[84] K. Hanada and B. Kermanshahi, “Ive Ch Ive,” vol. 2, no. 1, pp. 3–10, 2003.

[85] H.Sakai, “Friction and Wear of Tire Tread Rubber,” *Tire Sci. Technol.*, vol. 24, no. 3, pp. 252–275, 1996.

[86] R. Tamada and M. Shiraishi, “Prediction of Uneven Tire Wear Using Wear Progress Simulation,” *Tire Sci. Technol.*, vol. 45, no. 2, pp. 87–100, Apr. 2017.

[87] F. J. Martínez, M. Canales, S. Izquierdo, M. A. Jiménez, and M. A. Martínez, “Finite element implementation and validation of wear modelling in sliding polymer–metal contacts,” *Wear*, vol. 284–285, pp. 52–64, 2012.